Studies in Electrode Kinetics

A thesis submitted for the degree of Doctor of Philosophy
in Physical and Theoretical Chemistry

Martin C. Henstridge
St John's College

September 2012

Abstract

This thesis is concerned with the study of electrode kinetics, which we shall examine via comparison between theory with experiment. As such the first two chapters outline the basic principles of electrochemical experiments and their simulation.

First, we examine the properties of voltammetry at porous electrodes by means of both simulations and experiments.

We then introduce the symmetric Marcus-Hush (SMH) model of electrode kinetics as an alternative to the empirical Butler-Volmer model. First, we examine different methods for modeling the voltammetry of kinetically inhomogeneous electroactive monolayers. Next, we perform a critical evaluation of the SMH model for solution-phase systems through extensive comparison to experiments under diffusion-only and convective mass transport conditions using both cyclic and square wave voltammetry. The model is compared with the Butler-Volmer model throughout and is ultimately found to be poorly suited to the parameterisation of electrode kinetics, despite its foundations in the microscopic Marcus theory.

We then introduce the asymmetric Marcus-Hush model, which removes the assumption that the Gibbs energy curves for reactant and product have the same curvature. This modification results in an additional parameter which quantifies the asymmetry of the system. A similar evaluation of this model is then undertaken for both surface-bound and solution phase systems and the asymmetric model is found to be a great deal more successful than its symmetric predecessor.

Finally we outline a novel technique for extracting kinetic information directly from experimental cyclic voltammetry. The method is simple to implement and is general to all electrode geometries with one-dimensional symmetry.

Acknowledgements

First, special thanks go to Prof. Richard Compton for his immeasurable assistance as both tutor and supervisor over the course of the last 7 (!) years. I am also very grateful to EPSRC for funding my studies.

I also thank Edmund Dickinson, for helping me to get started in the world of computational electrochemistry, and all of those who undertook the experiments described within.

The members, past and present, of the RGC group have played a huge role in making the past three years enormously enjoyable. Thank you all, it wouldn't have been the same without you.

Last, but certainly not least, I thank Gemma for her endless patience.

Contents

1 Fundamentals of electrochemistry 1
1.1 Electrochemical equilibrium 1
1.2 The electric double layer 2
1.3 Dynamic electrochemistry 2
1.4 Experimental techniques 5
Bibliography 7

2 Electrochemical simulation 9
2.1 The finite difference method 9
2.2 Discretisation 10
2.3 The expanding grid 11
2.4 Solving the equations 12
2.5 Dimensionless variables 12
Bibliography 13

3 Mass transport to and within porous electrodes: enhanced voltammetric selectivity 14
3.1 Introduction 14
3.2 Theoretical model 16
3.3 Theoretical results 19
3.4 Experimental 23
3.5 Results 24
3.6 Discussion 25
3.7 Conclusion 28
Bibliography 29

4 Mass transport to and within porous electrodes: the prediction of double peaks for a single electrode process 36
4.1 Introduction 36
4.2 Theory 37
4.3 Results and discussion 38
4.4 Conclusion 43
Bibliography 43

5 The symmetric Marcus-Hush model of electrode kinetics 45
5.1 Introduction 45
5.2 Reorganisation energy 47

5.3 Experimental verification 47
5.4 Heterogeneous electron transfer 48
5.5 Characteristics of the model 50
5.6 Previous work 51
5.7 Conclusions 54
Bibliography 54

6 Electron transfer to and from species bound at a non-uniform electrode surface 57
6.1 Introduction 57
6.2 Theory 59
6.3 Theoretical results 61
6.4 Experimental procedure 62
6.5 Experimental results 65
6.6 Discussion 68
6.7 Conclusion 69
Bibliography 70

7 Evaluation of the symmetric Marcus-Hush model at a mercury microhemisphere electrode 73
7.1 Introduction 73
7.2 Theory 74
7.3 Experimental Methods 75
7.4 Results 76
7.5 Discussion 82
7.6 Conclusions 84
Bibliography 85

8 Evaluation of the symmetric Marcus-Hush model at a high-speed channel microband electrode 87
8.1 Introduction 87
8.2 Theory 88
8.3 Experimental 90
8.4 Results and discussion 91
8.5 Conclusions 96
Bibliography 96

9 Redox systems obeying Marcus-Hush electrode kinetics do not obey the Randles–Ševčík equation for linear sweep voltammetry 98
9.1 Introduction 99
9.2 Theory 100
9.3 Scan rate dependence of the peak current 100
9.4 Solution-phase results 104
9.5 Surface-bound results 106
9.6 Discussion 108
9.7 Conclusion 110
Bibliography 112

10 Asymmetric Marcus theory: application to electrode kinetics 113
10.1 Introduction 113
10.2 Theory 115
10.3 Results and discussion 118
10.4 Conclusions 120
Bibliography 122

11 Evaluation of the asymmetric Marcus-Hush model at a mercury microhemisphere electrode 124
11.1 Introduction 124
11.2 Theory 125
11.3 Experimental 125
11.4 Results 127
11.5 Discussion 133
11.6 Conclusions 134
Bibliography 135

12 Asymmetric Marcus-Hush Model of Electron Transfer Kinetics: Application to the voltammetry of surface-bound redox systems 137
12.1 Introduction 137
12.2 Theory 138
12.3 Results 139
12.4 Discussion 148
12.5 Conclusions 151
Bibliography 151

13 A comparison of the Butler-Volmer and asymmetric Marcus-Hush models of electrode kinetics at the channel electrode 153

13.1 Introduction 153
13.2 Theory 154
13.3 Results 154
13.4 Discussion 159
13.5 Conclusions 160
Bibliography 160

14 Direct extraction of kinetic parameters from experimental cyclic voltammetry 162

14.1 Introduction 162
14.2 Theory 163
14.3 Results 165
14.4 Discussion 172
14.5 Conclusions 172
Bibliography 172

15 Conclusions 174

A Marcus-Hush kinetics in the limit $\lambda \to \infty$ 177

Chapter 1

Fundamentals of electrochemistry

The work presented in this thesis is concerned with the kinetics of electrochemical reactions. In this chapter we review the basic principles of electrochemistry, discussing the thermodynamic and kinetic aspects of electron transfer and introduce voltammetric experiments as a means by which we may study electrochemical systems and their kinetics.

1.1 Electrochemical equilibrium

Consider a solution containing arbitrary concentrations of two species at equilibrium, A and B, which interconvert via the transfer of a single electron:

$$\mathrm{A} + \mathrm{e} \rightleftharpoons \mathrm{B} \tag{1.1}$$

If we then immerse in this solution a metallic electrode, the system will seek to minimise its total Gibbs energy. Should the Fermi energy of the electrode be sufficiently high in energy then it will be thermodynamically favourable for electrons to pass from the electrode into the solution and drive the conversion of A to B. This will result in a build up of positive charge on the electrode and a build up of negative charge in the solution.

Equally if the Fermi energy of the electrode is sufficiently low in energy then the conversion of B to A will be thermodynamically favourable and there will be a net transfer of electrons into the electrode, resulting in a build up of negative charge on the electrode and a build up of positive charge in the solution.

Once the system reaches equilibrium there will be no further net transfer of electrons, however the charge separation will remain and a potential difference at the electrode/solution interface will result. It is not possible to measure the absolute value of this potential difference, but it may be measured *relative* to a second (reference) electrode [1].

This relationship between potential and the concentrations of A and B is (ignoring activities) quantified by the Nernst equation [1]:

$$E = E_{\mathrm{f}}^{\ominus} + \frac{RT}{F} \ln \left(\frac{c_{\mathrm{A}}}{c_{\mathrm{B}}} \right) \tag{1.2}$$

where R is the gas constant, T is the absolute temperature, F is the Faraday constant, c_{A} and c_{B} are the concentrations of the species in solution and E is the potential difference between the electrode of interest (known as the working electrode) and the reference electrode. When A and B are present at unit concentration this potential takes the value $E_{\mathrm{f}}^{\ominus}$, known as the formal electrode potential.

1.2 The electric double layer

When a potential difference is established at the electrode/solution interface an electric ‘double layer’ is formed [1]. Oppositely charged ions form a ‘compact’ layer at the electrode surface, beyond which a ‘diffuse’ layer exists which consists of species which are subject both to thermal (Brownian) motion and electrostatic forces. As a result of the double layer, the potential drop between electrode and solution extends some distance into the solution. Additionally, the charging of this double layer is analogous to capacitive charging and leads to a ‘non-Faradaic’ contribution to the current drawn at the electrode.

1.3 Dynamic electrochemistry

Rather than measuring the potential difference resulting from the solution composition, a typical electrochemical experiment involves applying a potential difference at an electrode in order to induce an electron transfer reaction. Information about the reaction may then be extracted by measuring the resulting current as a function of the applied potential.

In order to measure the current at the working electrode we require a second electrode such that we have a complete circuit. The reference electrode cannot fulfil this role since its potential and, through Equation (1.2), its composition must be held constant and so current passing through it must be minimised. We therefore require a third electrode to balance the current passed at the working electrode, known as the counter (or auxiliary) electrode [2].

With a three-electrode system, we may now measure the current at the working electrode as a function of the potential at the same electrode. For a one-electron reaction, such as that in Equation (1.1), this is given by:

$$I = FAj_0 \tag{1.3}$$

where A is the area of the electrode and j_0 is the flux at the electrode surface:

$$j_0 = -k_{\mathrm{red}} c_{\mathrm{A},0} + k_{\mathrm{ox}} c_{\mathrm{B},0} \tag{1.4}$$

where k_{red} and k_{ox} are the rate constants for reduction and oxidation respectively and $c_{\mathrm{A},0}$ and $c_{\mathrm{B},0}$ are the concentrations of species A and B at the electrode surface.

In practice the current is a function of the rate of consumption of A at the electrode (electrode kinetics) and the supply of A at the electrode. For a redox couple dissolved in solution the latter is determined by the rate at which A is replenished from bulk solution (mass transport), if the redox couple is bound to the electrode surface it is simply a function of how much unreacted A remains.

1.3.1 Electrode kinetics

The simplest and most widely used model of electrode kinetics is the Butler-Volmer model [3–5], for which the rate constants are given by:

$$k_{\mathrm{red}} = k_0 \exp\left[\frac{-\alpha F}{RT}\left(E - E_{\mathrm{f}}^{\ominus}\right)\right] \tag{1.5}$$

$$k_{\mathrm{ox}} = k_0 \exp\left[\frac{+\beta F}{RT}\left(E - E_{\mathrm{f}}^{\ominus}\right)\right] \tag{1.6}$$

where k_0 is the standard heterogeneous rate constant and α and β are known as transfer coefficients which indicate the ‘position’ of the transition state. Typically these take values around $\frac{1}{2}$ and, for a one-electron reaction, $\alpha + \beta = 1$.

The term ‘transfer coefficient’, used throughout this thesis, is general to both single-electron and multi-electron transfer reactions. The term 'symmetry factor' is also used in relation to single-electron transfer reactions. The two terms are, however, equivalent for the one-electron mechanisms with which this thesis is principally concerned.

The bulk of this thesis is concerned with the evaluation of Marcus theory as an alternate model for the parameterisation of electrode kinetics. The Butler-Volmer model is used for comparison throughout.

1.3.2 Mass transport

For a redox couple dissolved in solution, once the electrode surface is depleted of species A the current is limited by the rate of mass transport. The flux of material in solution is quantified by the Nernst-Planck equation [2]:

$$j_i = \begin{cases} -D_i \nabla c_i & \text{Diffusion} \\ +c_i \bar{v} & \text{Convection} \\ -\frac{F}{RT} z_i c_i \nabla \phi & \text{Migration} \end{cases} \tag{1.7}$$

where D_i is the diffusion coefficient, $\bar{v}$ is the velocity of the solution, z_i is the species charge and ∇ is the del operator.

Of the three modes of mass transport, diffusion is most generally of interest to electrochemists. Experiments are typically carried out in the presence of a large excess of inert (so-called 'supporting') electrolyte. This compresses the potential difference at the electrode-solution interface to within a very short distance of the electrode surface, as such the potential gradient throughout the remainder of the solution is approximately zero and hence mass transport due to migration can be considered negligible. Mass transport due to natural convection, caused by a temperature or density gradient, may also be neglected if experimental timescales are kept short.

Under so-called 'diffusion-only' conditions the rate of change of concentration in solution is given by Fick's second law:

$$\frac{\partial c_i}{\partial t} = D_i \nabla^2 c_i \tag{1.8}$$

where ∇^2 is the Laplacian operator. Some of the later chapters employ convective mass transport, a more detailed discussion of which is found in Chapter 8.

1.4 Experimental techniques

In order to study the kinetics of a redox couple, we shall use a family of techniques known collectively as voltammetry. Current is measured as a function of potential for a variety of potential profiles.

1.4.1 Cyclic voltammetry

The potential is swept linearly from a value at which no reaction occurs to one at which A undergoes rapid conversion to B ($E \gg E_{\mathrm{f}}^{\ominus}$) and then back to the starting potential again. The rate at which the potential is varied with time is known as the voltage scan rate (v) and a plot of the measured current as a function of the applied potential is known as a voltammogram [2].

For a diffusional system the current initially increases with potential as the rate of electron transfer increases. However at some point, dependent on the reversibility of the electron transfer, the rate of consumption of A becomes dominated by the rate at which it is replenished via mass transport. At this point the current then begins to drop as the potential is increased further, resulting in a peak. On the reverse sweep a similar peak is observed as B is converted back to A.

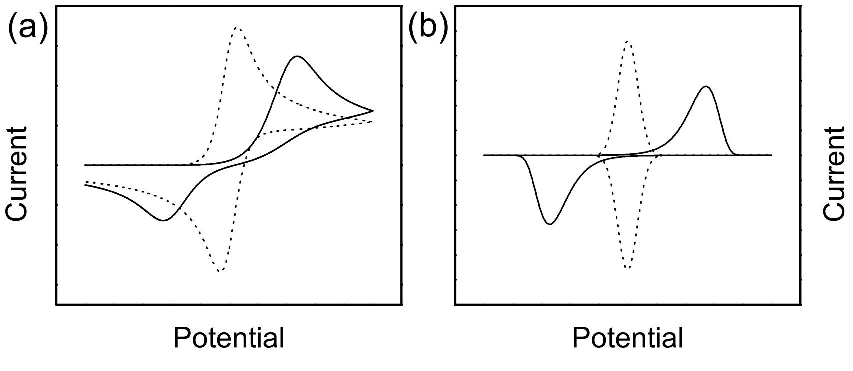

Figure 1.1: Cyclic voltammetry illustrating the different behaviour of systems with reversible (dotted line) and irreversible (solid line) kinetics for (a) diffusional system and (b) a surface-bound system.

In this thesis we also consider surface-bound redox systems for which the current also increases initially with potential. However in this case the current becomes limited by the availability of species A, which eventually becomes completely consumed and the current falls towards zero.

For both diffusional and surface-bound systems exhibiting fast (reversible) electron transfer; both forward and back peaks occur in the vicinity of the formal potential. However for slow (irreversible) electron transfer, very high overpotentials are required for electron transfer to become sufficiently fast to overtake the rate of mass transport and so there is a large separation between the forward and back peaks, as shown in Figure 1.1.

More quantitative information about a redox system may be extracted via analysis of the entire voltammetric wave, however this requires numerical simulation and will be discussed in the next chapter.

1.4.2 Pulse voltammetry

Such techniques apply a potential which consists of a series of pulses superimposed onto a potential staircase. The current signal is then given by the difference between currents recorded at the end of consecutive pulses [6]. The two components (staircase and pulses) and the overall potential profile for differential pulse voltammetry (DPV) are shown in Figures 1.2 and 1.3.

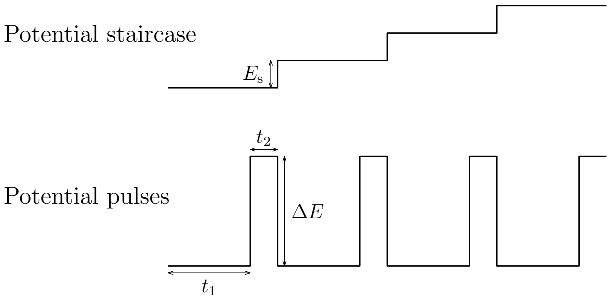

Figure 1.2: Schematic diagram of the components of the potential profile for differential pulse voltammetry.

Due to its subtractive nature, pulse voltammetry is a very sensitive technique which minimises interference from the double layer. It has been demonstrated to be even more sensitive to the subtleties of electrode kinetics than cyclic voltammetry [7, 8], however its interpretation is less straightforward.

In addition to DPV, we also employ square wave voltammetry (SWV) for some ex-

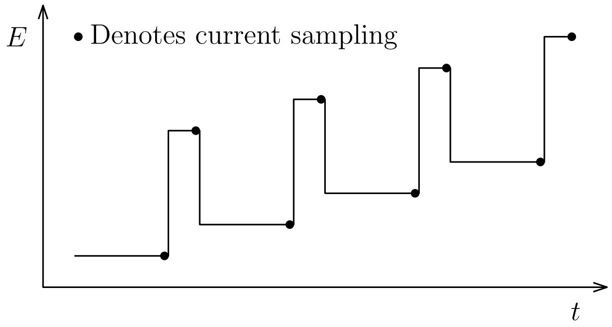

Figure 1.3: Schematic diagram of the overall potential profile for differential pulse voltammetry.

periments in this thesis. This is a special case of DPV for which $t_1 = t_2$ and the pulse amplitude (ΔE) carries the opposite sign.

1.4.3 Microelectrodes

The above discussion is based on the assumption that the electrode is large. As the electrode decreases in size, the diffusional regime changes from 'linear' at the macroscale to 'convergent' at the micrometre scale [9]. This is due to the increasing importance of diffusion to the edges of the electrode as it becomes smaller.

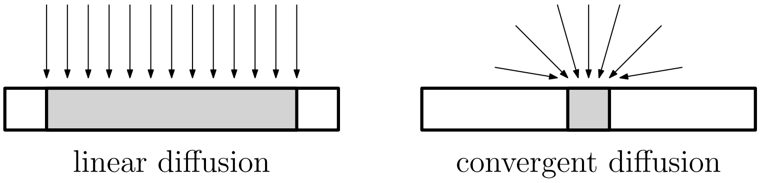

Figure 1.4: Schematic diagram of linear and convergent diffusion regimes.

This change in mass transport at so-called microelectrodes means that, at sufficiently slow scan rates, a steady-state is reached whereby the current reaches a limiting value at high overpotential, rather than going through a maximum. At higher scan rates it is also possible to obtain the peak-shaped voltammetric response characteristic of macroelectrodes and so it is possible to examine both linear and convergent diffusion regimes at a single electrode by varying the scan rate.

Bibliography

[1] A. J. Bard and L. R. Faulkner, *Electrochemical Methods: fundamentals and applications* (Wiley, 2001), 2nd edition.

[2] R. G. Compton and C. E. Banks, *Understanding voltammetry* (Imperial College Press, 2010), 2nd edition.

[3] W. J. Albery, *Electrode Kinetics* (Clarendon Press, 1975).

[4] T. Erdey-Grúz and M. Volmer, *Z. Physik Chem.* **150** (1930) 203–213.

[5] J. A. V. Butler, *Trans. Faraday Soc.* **28** (1932) 379–382.

[6] A. Molina, E. Laborda, F. Martínez-Ortiz, D. F. Bradley, D. J. Schiffrin and R. G. Compton, *J. Electroanal. Chem.* **659** (2011) 12–24.

[7] E. Laborda, M. C. Henstridge, A. Molina, F. Martínez-Ortiz and R. G. Compton, *J. Electroanal. Chem.* **660** (2011) 169–177.

[8] D. Suwatchara, N. V. Rees, M. C. Henstridge, E. Laborda and R. G. Compton, *J. Electroanal. Chem.* **665** (2012) 38–44.

[9] K. Aoki, *Electroanalysis* **5** (1993) 627–639.

Chapter 2

Electrochemical simulation

Qualitative information may easily be gained from voltammetric experiments. For example the reversibility of a system may be determined by measuring the separation between the forward and back peaks. However, in order to extract more quantitative information, for example the value of k_0, one must compare the voltammetry with a theoretical model. Some simple experimental systems, such as chronoamperometry at a planar electrode, may be solved analytically [1]. The vast majority, however, require numerical solution.

Simulating voltammetry involves solving the mass transport equation, subject to the electrochemical reaction occurring at the electrode surface. At each point in time we apply the relevant potential at the electrode and solve to find the concentration profile, from which we may calculate the flux at the electrode and therefore the current. This chapter discusses the various methods which are employed in this process.

2.1 The finite difference method

One method of solving this differential equations is to approximate derivatives as finite differences. For example we may approximate the derivative of some function $f(x)$ at some point as the gradient of a straight line between two nearby points, x_a and x_b:

$$\frac{\mathrm{d}f}{\mathrm{d}x} \approx \frac{\Delta f}{\Delta x} = \frac{f(x_a) - f(x_b)}{x_a - x_b} \tag{2.1}$$

Clearly, the nearer the points x_a and x_b are to the point of interest the better the approximation will be [2]. We may calculate the derivative across a domain by dividing it into a grid of points. The derivative at x_i may then be approximated by considering its immediate neighbours:

$$\frac{\mathrm{d}f}{\mathrm{d}x} \approx \frac{f(x_{i+1}) - f(x_i)}{x_{i+1} - x_i} \tag{2.2}$$

This is known as the *forward difference* approximation. Equally, we could calculate this derivative by considering points x_i and x_{i-1}, known as the *backward difference* approximation. Both of these methods are accurate to first order, that is to say that the error in this approximation varies with Δx.

It is better to employ a method known as the *central difference* approximation, which calculates the derivative from points x_{i-1} and x_{i+1}:

$$\frac{\mathrm{d}f}{\mathrm{d}x} \approx \frac{f(x_{i+1}) - f(x_{i-1})}{x_{i+1} - x_{i-1}} \tag{2.3}$$

This approximation is accurate to second order, *i.e.* the error varies with $(\Delta x)^2$, and is thus used in preference wherever possible.

Second derivatives are merely the derivative of the derivative. The finite difference method is thus easily extended to second derivatives and beyond by applying these formulae recursively.

2.2 Discretisation

As discussed in the previous chapter we are largely concerned with solving Fick's second law, given here for a planar electrode:

$$\frac{\partial c}{\partial t} = D\frac{\partial^2 c}{\partial x^2} \tag{2.4}$$

We must approximate the left-hand side of Equation (2.4) using the forward difference method described in the previous section since there is no time-step prior to the beginning of the experiment and so the central difference method is not practical.

We now have a choice regarding the discretisation of the right-hand side of Equation (2.4). Either we use the concentrations from the current time-step (j) or the concentrations from the next time-step $(j+1)$.

$$\text{Explicit} \qquad \frac{c_{j+1}-c_j}{t_{j+1}-t_j} = D\frac{\partial^2 c_j}{\partial x^2} \tag{2.5}$$

$$\text{Implicit} \qquad \frac{c_{j+1}-c_j}{t_{j+1}-t_j} = D\frac{\partial^2 c_{j+1}}{\partial x^2} \tag{2.6}$$

Both methods are accurate to first order, however they differ in their stability – defined as the propensity of a method to propagate errors form one time-step to the next. The implicit scheme is unconditionally stable, whereas the explicit scheme is not. Implicit discretisation is therefore used for all one-dimensional simulations in this thesis.

Particular mention must be made of the simulation of two-dimensional systems such as the array of cylindrical electrodes studied in Chapters 3 and 4. It is possible to solve such systems using an entirely implicit (or indeed explicit) discretisation, however this is a very computationally expensive method. Instead we employ a method known as the alternating direction implicit (ADI) method. This involves sub-dividing each time-step into two halves and treating each separately. In the first half of the time-step we discretise the mass transport equation implicitly in one dimension and explicitly in the other. In the second half of the time-step the discretisation schemes for the two dimensions are exchanged. This system is also unconditionally stable and is a much more efficient method than either the fully implicit or fully explicit schemes for tackling two-dimensional problems.

2.3 The expanding grid

Electrochemical reactions are confined to the electrode surface and thus the largest variation in concentration occurs in the immediate vicinity of the electrode. We require a small grid spacing in this region to retain accuracy, but the same small grid spacing far from the electrode is wasteful since there is very little variation in the concentration.

If we employ a grid for which the spacing expands with increasing distance from the electrode, we may use much a much smaller grid spacing at the electrode surface than would be practical with a non-expanding grid while having a larger separation far from the electrode where there is little change in concentration throughout the experiment.

An expanding grid with properly selected parameters can bring about increased simulation accuracy while reducing computation time because the total number of points in the grid is smaller.

In this thesis we employ a grid for which the spacing (Δx_i) is a function of two parameters: the initial spacing (h_0) and the expansion coefficient (γ) such that:

$$\Delta x_0 = h_0 \tag{2.7}$$

$$\Delta x_n = \gamma \Delta x_{n-1} \tag{2.8}$$

2.4 Solving the equations

Solution of the simultaneous equations resulting from the discretisation of the mass transport equation requires the application of suitable boundary conditions, which must also be discretised.

At the electrode surface a rate equation such as the Butler-Volmer equation is applied and bulk concentrations are assumed at a sufficiently large distance from the electrode. The specific boundary conditions for each system studied in this thesis are discussed in the relevant chapters.

By writing the set of simultaneous equations as a matrix equation, we may take advantage of the fact that the solution at a particular point is a function only of its immediate neighbours. The resulting matrix is in fact tridiagonal and may therefore be solved efficiently using the Thomas algorithm [1]. The Thomas algorithm is a simplified form of Gaussian elimination and solves a system of n simultaneous equations in $O(n)$ operations, compared with $O(n^3)$ for Gaussian elimination.

This process returns the concentration profile for the next time-step and we may now calculate the current by integrating the flux (given by Fick's first law) across the surface of the electrode.

2.5 Dimensionless variables

It is often convenient to use dimensionless variables since the number of independent variables is reduced. While most results are given in conventional units, throughout this thesis we shall refer to the following:

$$\begin{array}{ll}
\text{Distance:} & R = \dfrac{r}{r_\mathrm{e}} \\
\text{Time:} & \tau = \dfrac{D_\mathrm{A}}{r_\mathrm{e}^2}\, t \\
\text{Concentration:} & C = \dfrac{c_i}{c_\mathrm{A}^*} \\
\text{Potential:} & \theta = \dfrac{F}{RT}\left(E - E_\mathrm{f}^{\ominus}\right) \\
\text{Standard rate constant:} & K_0 = \dfrac{r_\mathrm{e}}{D_\mathrm{A}}\, k_0 \\
\text{Scan rate:} & \sigma = \dfrac{F}{RT}\dfrac{r_\mathrm{e}^2}{D_\mathrm{A}}\, v \\
\text{Current:} & J = \dfrac{I}{2\pi F D_\mathrm{A} r_\mathrm{e} c_\mathrm{A}^*}
\end{array}$$

where r_e is the electrode radius, c_A^* is the bulk concentration of species A and the other symbols have been defined previously.

Bibliography

[1] R. G. Compton and C. E. Banks, *Understanding voltammetry* (Imperial College Press, 2010), 2nd edition.

[2] D. Britz, *Digital Simulation in Electrochemistry* (Springer, 2005), 3rd edition.

Chapter 3

Mass transport to and within porous electrodes: enhanced voltammetric selectivity

We use a combination of simulation and experiment to show that the modification of an electrode surface with a conducting porous layer can be used to modify the mass transport regime from linear (planar) diffusion to one of approximately 'thin layer' character. Further, we demonstrate that this alteration can, in favourable circumstances, facilitate the amperometric discrimination between species which oxidise or reduce at similar potentials under planar diffusion conditions. The method is illustrated experimentally with respect to the detection of dopamine at naked glassy carbon electrodes and at such electrodes modified with a layer of multiwalled carbon nanotubes, and experiments are reported which are consistent with the proposed strategy.

This work has been published in *Sensors and Actuators B: Chemical* [1]. The experiments described below were performed by M. Aslanoglu and the simulations were performed using a program written by E. J. F. Dickinson.

3.1 Introduction

The use of amperometric methods in electroanalysis offers a highly sensitive approach for the detection of a diverse range of analytes, allowing low detection limits and good precision. However there is often significant interference from other redox active species present which may undergo electrolysis at a similar potential to that required to oxidise or reduce the desired target molecule.

Such an example arises in the determination of the neurotransmitter dopamine by means of its two electron oxidation using carbon based electrodes. Molecules such as uric acid, ascorbic acid and serotonin all display redox behaviour at potentials close to those required for the oxidation of dopamine, thus interfering with its accurate determination.

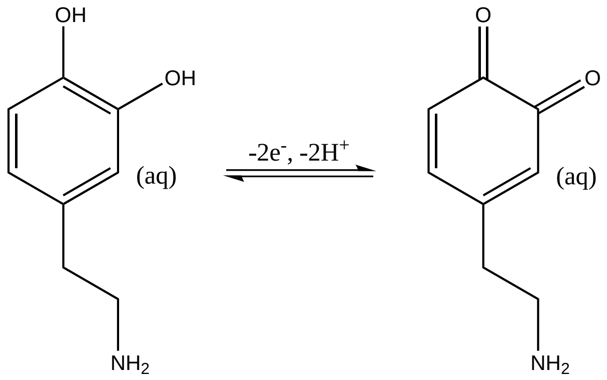

One strategy to overcome such problems is to retain the use of carbon based electrodes, which is attractive owing to their low cost and easy production, but to modify the surface of the electrode to produce a 'chemically modified electrode'. The stated aim is often to alter the electrode kinetics of the target species and/or the interfering species such that the voltammetric peak due to the target is shifted relative to those of the interferents.

The range of chemically modified electrodes is truly huge and highly diverse [2–11]. In the case of dopamine, and its selective measurement, the various electroanalytical approaches to the problem may be divided into those using electrodes chemically modified with polymer films [12–62], electrodes modified with carbon nanotubes [63–81] and other strategies including a few uses of bare, that is *un*modified, electrodes [82–135].

It is often presumed that the success of such modified electrodes arises from 'electrocatalytic' properties conferred on the electrode surface by virtue of the chemical modification. Thus, the argument runs, the rate of electron transfer to the target molecule increases and so its voltammetric peak moves to a lower overpotential. However the electrode kinetics of the interfering species are unaffected and so their voltammetric signals remain at their original potentials. Thus the voltammetric signal from the target species now occurs at a different potential to those of the interferents and so may be observed separately.

The molecular basis for such differential electrocatalysis is rarely explored or reported. In passing, it can be noted that 'negative electrocatalysis', that is to say a slowing down of the electrode kinetics of the target relative to the interferents would be similarly effective in realising the sought voltammetric discrimination and resolution but, strikingly and perhaps significantly, is rarely seen or reported highlighting the evidently highly empirical approaches to surface modification adopted in many electrode modification studies.

We emphasise that the voltammetric peak potential for a redox couple reflects *both* the electrode kinetics of the couple *and* the mass transport regime under which it is measured. Thus, for example, it is well known that electrochemically irreversible couples show voltammetric features at higher overpotentials at a microdisc than at macroelectrodes made of chemically and physically exactly the same material. This change results entirely from the changed mass transport regime – from planar to convergent diffusion – and not at all from the electrode kinetics which are unchanged.

A review of the literature for the amperometric detection of dopamine in the presence of such interferents, found in Reference [1], reveals that the apparent modus operandi for many chemically modified electrodes designed for the determination of dopamine may rely on the proposed mechanism of altered mass transport.

We report simulated cyclic voltammetry for redox systems with varying electrochemical reversibility at both a planar (unmodified) electrode and an electrode modified with a conductive porous film to demonstrate the effect of changing the mass transport regime from planar to approximately 'thin layer' in character. These simulated results are then compared with experimental cyclic voltammetry for the oxidation of dopamine at a glassy carbon (GC) electrode both in its bare, unmodified state and modified with a film of multi-walled carbon nanotubes (MWCNT).

3.2 Theoretical model

We consider the redox reaction $\mathrm{A} - \mathrm{e} \rightleftharpoons \mathrm{B}$ taking place at an electrode modified with a conducting porous film in the presence of sufficient supporting electrolyte such that migration may be neglected [136]. The porous film is modeled as a regular array of vertically aligned cylinders protruding from the electrode surface. Both the sides and the ends of the cylinders are considered to be conductive, along with the electrode base. The thickness and porosity of the 'film' are controlled via the length (Z_e) and radial separation (R_max) of the cylinders.

This cylindrical array is simulated using the diffusion domain approximation [137–

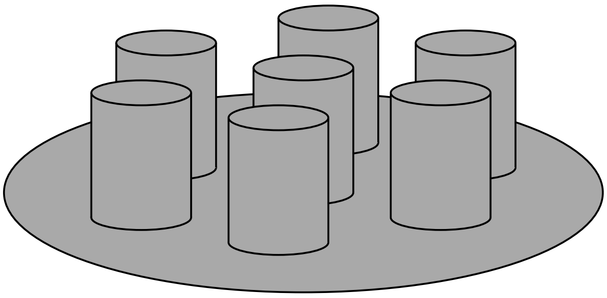

Figure 3.1: Schematic diagram of the cylinder array.

140]. The array is regular and is therefore composed of a series of repeated unit cells, each containing one cylinder. Thus the behaviour of the entire array may be characterised by the behaviour of one unit cell.

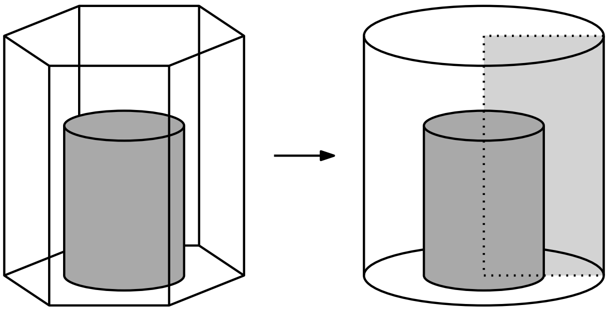

Figure 3.2: Schematic diagram of the diffusion domain approximation, the simulation space is outlined with a dotted line.

The unit cell is approximated as a cylinder which is concentric to the cylinder protruding from the surface and symmetric with neighbouring unit cells at its outer boundary (shown in Figure 3.2). Butler-Volmer kinetics operate at the surface of the cylinders (both the sides and the top) and the electrode base and at a large distance from the top of the cylinders the concentrations of A and B take their bulk values. The simulation space is symmetric through both the inner boundary (the centre of the cylinder) and through the outer boundary (the edge of the diffusion domain) and so a zero flux boundary condition is applied in both cases. Fick's second law (Equation (3.1)) is applied throughout. The simulation space is shown in Figure 3.3.

$$\frac{\partial C}{\partial \tau} = \frac{\partial^2 C}{\partial Z^2} + \frac{1}{R}\frac{\partial C}{\partial R} + \frac{\partial^2 C}{\partial R^2} \tag{3.1}$$

This two dimensional problem is solved using the alternating direction implicit (ADI) method. Equation (3.1) and the above boundary conditions are discretised over an ir-

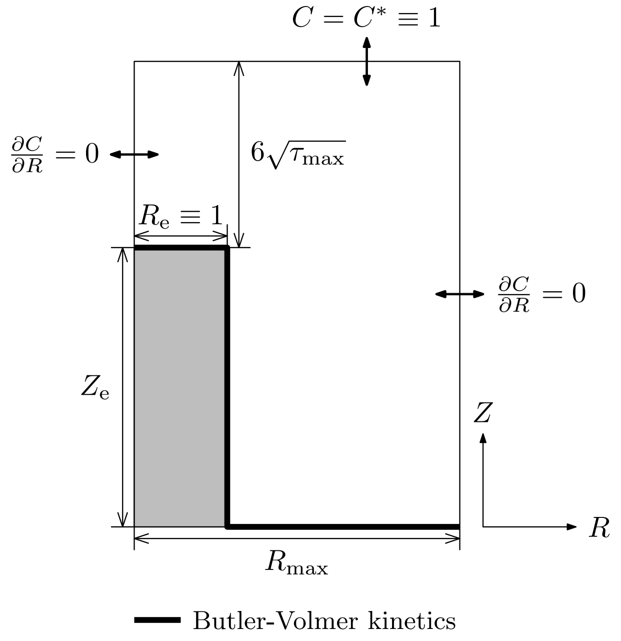
$C = C^* \equiv 1$
$\frac{\partial C}{\partial R} = 0$
$6\sqrt{\tau_{\text{max}}}$
$R_\text{e} \equiv 1$
$\frac{\partial C}{\partial R} = 0$
Z_e
Z
R
R_{max}
Butler-Volmer kinetics

Figure 3.3: Schematic diagram of the simulation space with boundary conditions shown.

regular grid of points. Each timestep is then split into two: for the first half-timestep Equation (3.1) is solved implicitly in the Z direction and explicitly in the R direction and vice versa for the second half-timestep. For each half-timestep the system of simultaneous equations is formulated as a tridiagonal matrix and solved using the Thomas algorithm.

For the Z-implicit step the current is given by $\frac{\partial C}{\partial Z}$ at the electrode base and the top of the cylinder; for the R-implicit step the current is given by $\frac{\partial C}{\partial R}$ at the side of the cylinder. The current for the complete timestep is given by the sum of the currents for each half-timestep.

This system is characterised by the interplay between the planar and 'thin layer' diffusional regimes. While the cylinder array model may only be a rudimentary approximation, it retains the physical essence of the problem; it contains a region exposed to the bulk solution in which planar diffusion operates and a region amongst the cylinders where 'thin layer' diffusion operates [141, 142].

Both the cylinders and electrode base are conductive and are assumed to obey Butler-Volmer kinetics with the same values for k_0 and α. Throughout the following simulations a typical experimental scan rate of $100\,\text{mV}\,\text{s}^{-1}$ is used, the diffusion coefficients D_A and D_B are both set to $1 \times 10^{-5}\,\text{cm}^2\,\text{s}^{-1}$ and r_e was set to $20\,\text{nm}$ (a typical value for a carbon nanotube).

3.3 Theoretical results

3.3.1 Voltammetry at an unmodified electrode

As a basis for comparison cyclic voltammetry was simulated for a flat (unmodified) electrode using the commercial software Digisim^{TM}[143].

We consider four couples with formal potentials of 0.0 V, −0.15 V, −0.30 V and −0.60 V. The couple at 0.0 V was considered to have completely reversible (Nernstian) kinetics and the k_0 values for the remaining three couples were selected such that their oxidative peak potentials coincided with the peak of the reversible couple at $100\,\mathrm{mV\,s^{-1}}$. This was achieved using the values in Table 3.1.

$E_\mathrm{f}^{\ominus}$ (V)	k_0 ($\mathrm{cm\,s^{-1}}$)
0.00	∞
−0.15	2.98×10^{-4}
−0.30	1.60×10^{-5}
−0.60	4.70×10^{-8}

Table 3.1: Parameters used for the four redox couples such that their oxidative peak potentials were identical at the flat electrode at $100\,\mathrm{mV\,s^{-1}}$.

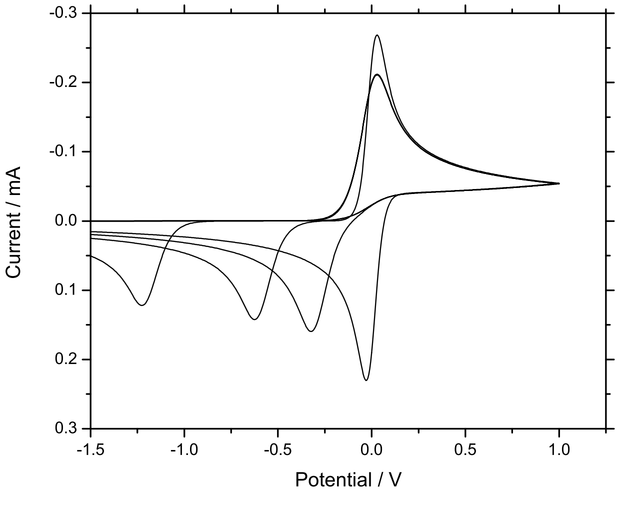

Figure 3.4: Simulated voltammetry obtained from Digisim for the four couples using the parameters in Table 3.1 at $100\,\mathrm{mV\,s^{-1}}$.

The voltammetry obtained using these parameters, shown in Figure 3.4, confirms that these four couples would be indistinguishable by means of their voltammetric oxidation at a flat electrode at 100 mV s^{-1}. Changing the scan rate to either 20 mV s^{-1} and 2 V s^{-1} enabled only the reversible couple to be differentiated from the three slower couples whose oxidative peaks remain indistinguishable from each other, as shown in Figure 3.5.

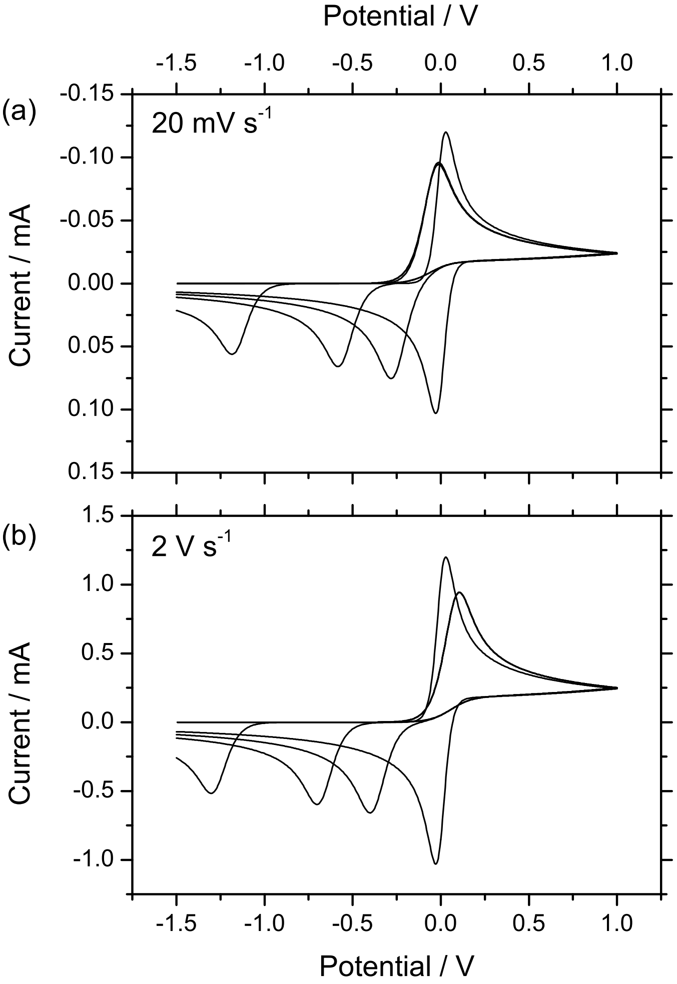

Figure 3.5: Digisim voltammetry for the four couples at (a) 20 mV s^{-1} and (b) 2 V s^{-1}.

3.3.2 Voltammetry at the modified electrode

Having characterised the four redox couples at the unmodified electrode, we may now examine the effects of modifying the electrode with a conducting porous film. First we examine the effect of varying cylinder separation (film porosity) on peak potential. Cyclic voltammetry was simulated for the four redox couples for a range of R_{max} values while Z_{e} was held constant.

The plot in Figure 3.6 shows the variation of oxidative peak potential with varying cylinder separation for the four redox couples. In the limit of very high cylinder separation there are very few cylinders on the electrode surface, hence the electrode is approximately flat and the diffusion is predominantly planar. As such the oxidative peak potentials coincide as was the case for the unmodified electrode.

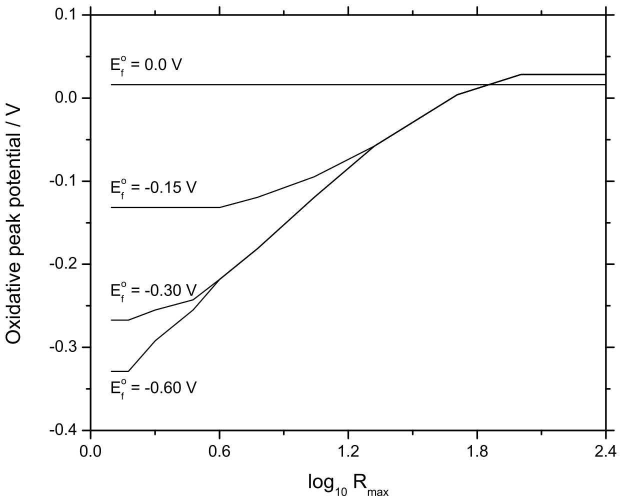

Figure 3.6: Plot of peak potential against $\log R_{\mathrm{max}}$ for the four simulated redox couples ($Z_{\mathrm{e}} = 1000$).

The reversible couple shows no change in peak potential on varying R_{max}. However as cylinder separation decreases the peaks for the less reversible couples shift to more negative potentials, even approaching their $E_{\mathrm{f}}^{\ominus}$ values at very low cylinder separation.

Figure 3.7 shows the voltammetry simulated for $R_{\mathrm{max}} = 1.25$. At this low cylinder separation the peaks for the three irreversible couples have shifted sufficiently from their values at the unmodified electrode that all four couples are observable as distinct voltammetric peaks. Since k_0 is held constant for each couple, the increase in resolution achieved at low separation must be attributed to the diffusional regime moving from approximately planar at high R_{max} to approximately 'thin layer' at low R_{max}.

Next the effect of varying film thickness on peak potential was investigated. Voltammetry was simulated for a range of Z_{e} values while R_{max} was held constant. The resulting

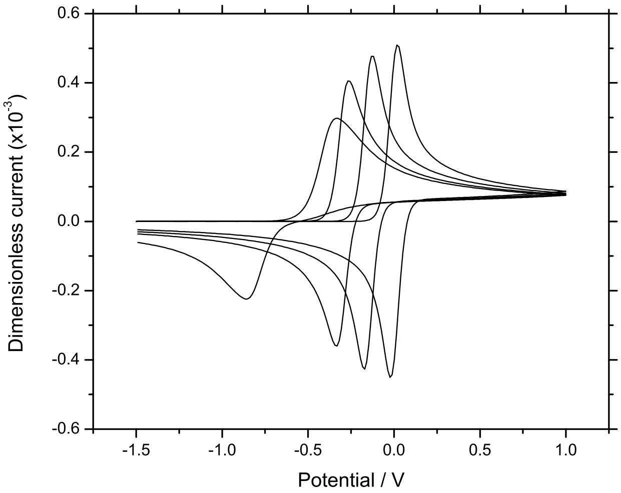

Figure 3.7: Voltammetry simulated at the modified electrode ($Z_\mathrm{e} = 1000$, $R_\mathrm{max} = 1.25$).

voltammetry for one of the couples ($E_\mathrm{f}^\ominus = -0.15\,\mathrm{V}$ and $k_0 = 2.98 \times 10^{-4}\,\mathrm{cm\,s^{-1}}$) is shown in Figure 3.8.

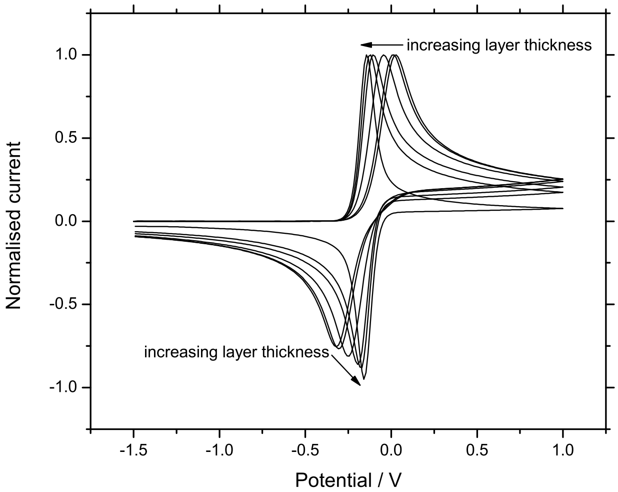

Figure 3.8: Voltammetry simulated at a cylinder array of variable thickness (current is normalised with respect to the anodic peak current in each case), $R_\mathrm{max} = 5$.

When the cylinders in the array are very short the electrode is approximately flat, thus for small Z_e the peak potential approaches the value obtained at the unmodified electrode. However as Z_e increases both the oxidative and reductive peaks move to significantly lower overpotentials compared with those observed at the unmodified electrode.

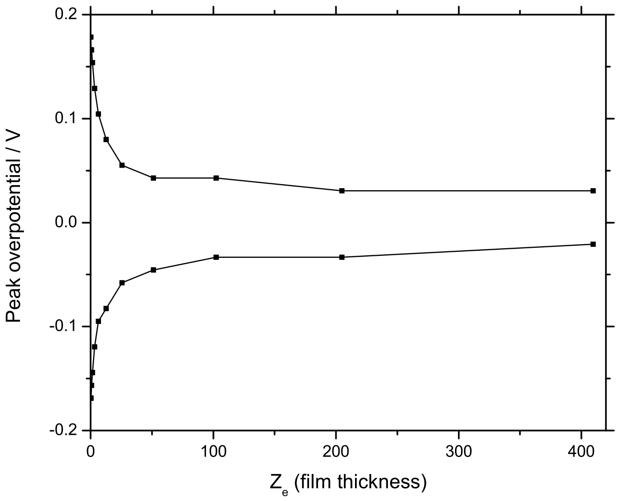

Figure 3.9: Plot of peak potential against film thickness for a one electron oxidation ($E_{\mathrm{f}}^{\ominus}$ = $-0.15\,\mathrm{V}$, $k_0 = 2.98 \times 10^{-4}\,\mathrm{cm\,s^{-1}}$). The upper line is for the oxidative peak, the lower line is for the reductive peak.

The variation of peak potential with film thickness is plotted in Figure 3.9. According to the present simulations a conductive porous film of thickness $200 \times r_{\mathrm{e}}$ (corresponding to 4.0 µm) is able to shift the oxidative peak by approximately 150 mV compared with that observed at an unmodified electrode. Since k_0 is again held constant throughout this series of simulations, the variation of peak potential is due to the changing geometry of the electrode and the resultant change in mass transport regime – from planar to more 'thin layer' diffusion.

3.4 Experimental

3.4.1 Chemical reagents

All chemicals were obtained from Aldrich with highest grade available and used without further purification. Multi-walled carbon nanotubes (MWCNTs) of > 95 % purity were obtained from NanoLab, USA. All solutions were prepared using deionised water from Vivendi UHQ grade water system with resistivity of not less than 18.2 MΩ cm at 25 °C. Dopamine stock solution was prepared with 0.1 M phosphate buffer at pH 7.0.

3.4.2 Instrumentation

Electrochemical measurements were recorded using a computer controlled µ-Autolab potentiostat with a standard three electrode configuration. A glassy carbon electrode with a geometric area of 0.07 cm^2 (BAS) was used as working electrode, a platinum wire as counter electrode and a saturated calomel reference electrode (SCE, Radiometer) completing the cell assembly. Prior to modification with MWCNTs the GCE was polished with 1 µm and 0.3 µm alumina. The electrode was then sonicated for 5 minutes in ethanol. All experiments were carried out at room temperature.

3.4.3 Preparation of MWCNT-modified electrodes

Multiwalled carbon nanotubes were first dispersed in chloroform (1 mg in 5 ml). This was placed into ultrasonic bath for 10 min, after which an aliquot of known volume was cast onto the glassy carbon electrode and the solvent allowed to evaporate.

3.4.4 Ohmic drop

Due to the very close proximity of neighbouring carbon nanotubes, it is possible that voltammetry recorded at the MWCNT-modified electrode may be affected by Ohmic drop effects. Theoretical work has shown, however, that the potential drop at the surface of charged cylinder is compressed into a smaller region than is the case for a planar electrode [144] and so the magnitude of any possible distortion due to Ohmic drop is likely to be small.

3.5 Results

Cyclic voltammetry was performed at a bare glassy carbon electrode for a 1 mM solution of dopamine in 0.1 M pH 7 phosphate buffer, the voltammetry for a range of scan rate is shown in Figure 3.10. Plotting log peak current against log scan rate yielded a slope close to 0.5, suggesting that the wave is diffusional in nature (as opposed to arising from adsorbed dopamine). A diffusion coefficient of $1.1 \times 10^{-5}\,\text{cm}^2\,\text{s}^{-1}$ was estimated from a Randles-Sevčík plot which compares well with values from the literature [145, 146] which are in the range $6.6 \times 10^{-6}\,\mathrm{cm^2\,s^{-1}}$ to $1.5 \times 10^{-5}\,\mathrm{cm^2\,s^{-1}}$.

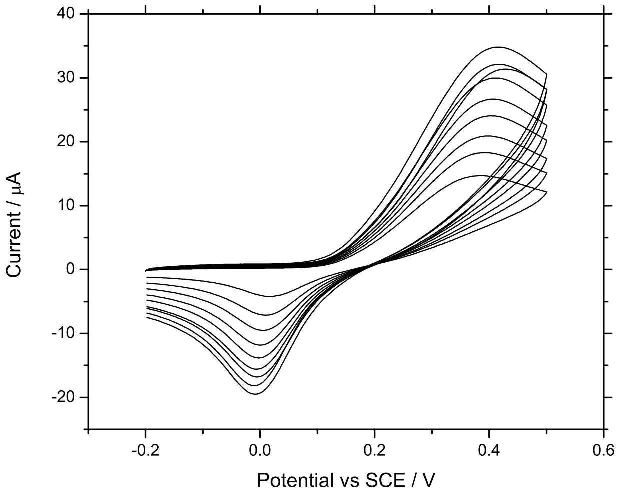

Figure 3.10: Cyclic voltammetry of a solution containing 1 mM dopamine and 0.1 M phosphate buffer (pH 7) at a bare GC electrode. Scan rates from 50 – 250 mV $\mathrm{s^{-1}}$.

Cyclic voltammograms were then recorded at the same glassy carbon electrode modified with MWCNTs, the voltammetry recorded at a range of scan rates is shown in Figure 3.11. For the MWCNT-GC electrode (modified with 8 µg MWCNTs), peak current was observed to vary linearly with scan rate as shown in Figure 3.12. Voltammetry was recorded immediately after exposure of the electrode to the solution and changed only a little over a period of *ca.* 10 min. From this it was inferred that adsorption effects, although likely present, were considerably less significant than solution-phase signals.

The effect of varying the mass of MWCNTs on the electrode surface was then examined. Cyclic voltammetry was recorded at the glassy carbon electrode modified with varying amounts of MWCNTs, the results are shown in Figure 3.13. As was the case for the simulated 'modified electrode', as the mass of MWCNTs increases (*i.e.* the film thickness increases) both oxidative and reductive peaks shift to lower overpotential. The variation of peak potential with the mass of MWCNTs is shown in Figure 3.14.

3.6 Discussion

The data reported above are consistent with a mechanistic interpretation in which the oxidation of dopamine shows a quasi-reversible response on a naked glassy carbon electrode

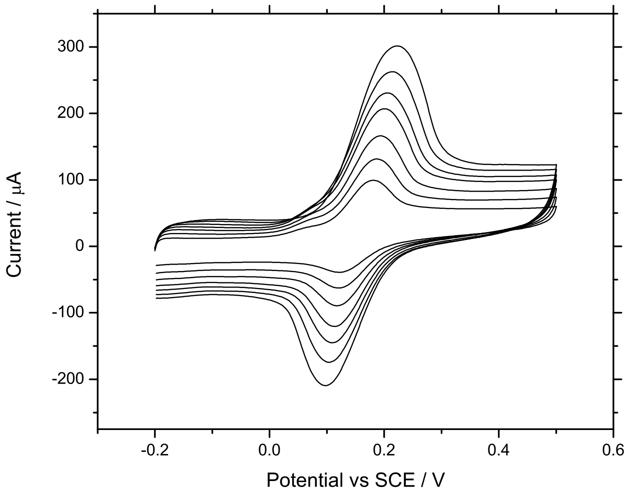

Figure 3.11: Cyclic voltammetry of a solution containing 1 mM dopamine and 0.1 M phosphate buffer (pH 7) at a GC electrode modified with 8 µg MWCNTs. Scan rates from 50 – 250 mV s^{-1}.

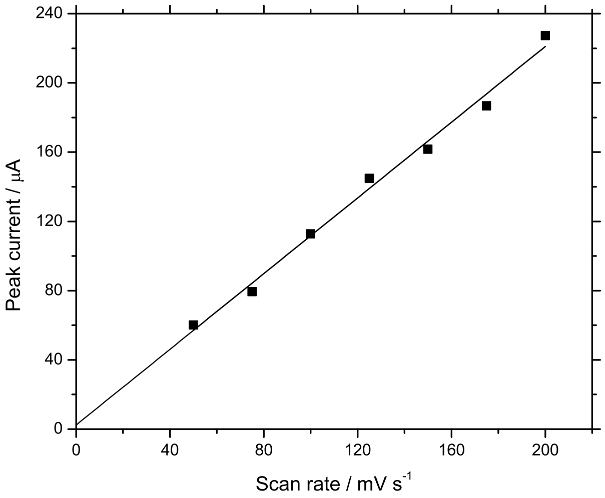

Figure 3.12: Plot of scan rate against peak current for 1 mM dopamine at a glassy carbon electrode modified with 8 µg MWCNTs.

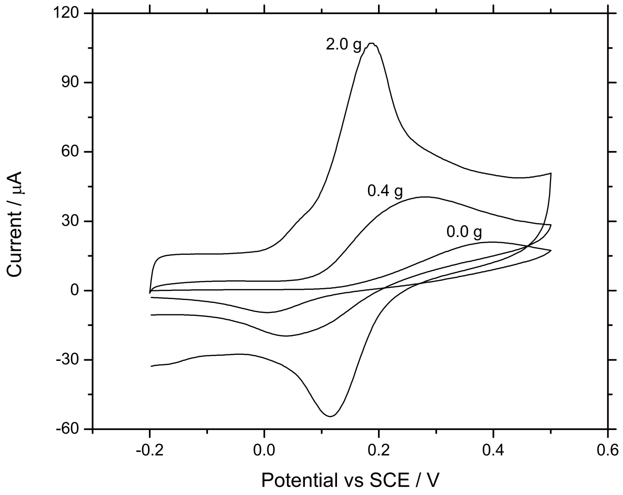

Figure 3.13: Overlaid voltammograms recorded at $100\,\mathrm{mV\,s^{-1}}$ of $1\,\mathrm{mM}$ dopamine at a GC electrode modified with differing amounts of MWCNTs.

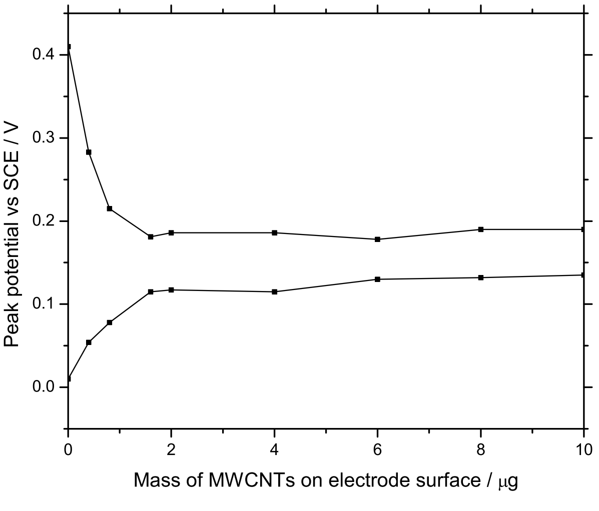

Figure 3.14: Plot of mass of MWCNTs against peak potential for a $1\,\mathrm{mM}$ dopamine solution. The upper line is for the oxidative peak, the lower line is for the reductive peak.

in which appreciable overpotential is required to drive the two electron oxidation. As the electrode is increasingly covered with a thicker film of MWCNTs the peak-to-peak separation is seen to reduce and the electrochemical signal becomes electrochemically more reversible. The potential required for the oxidation shifts to lower values and thus is consistent with a transition from planar diffusion to thin layer diffusion as simulated earlier in this chapter. This shift in potential can, at least in principle, lead to the differentiation of the signal from other analytes that might undergo oxidation at similar potentials but which show different values of the parameters $E_f^{\ominus}$, k_0 and α.

The transition to thin layer behaviour is characterised by a change in the peak current response from a square root dependence on voltage scan rate to a linear dependence. Such a behaviour would also be seen if the analyte were adsorbed, rather than diffusing in the solution phase: the case of adsorption might perhaps be regarded as the ultimate limit of thin layer diffusion. Indeed layers of MWCNTs have been proposed for adsorptive stripping voltammetry [147, 148].

The distinction between thin layer diffusion and adsorption effects is not easy to make especially where the adsorption is rapidly reversible. Where the kinetics of adsorption and desorption is slow the presence or absence of memory effects can be insightful. In particular if a voltammetric signal persists after transferring the electrode from the target solution to a fresh electrolyte solution containing no analyte then adsorption effects may be inferred. Another indication of the presence of adsorption effects is a signal steadily increasing in intensity over a period of time [147]. In the present case of dopamine oxidation; strong oxidative signals were seen immediately on exposure to the solution which changed relatively little with prolonged immersion of the electrode prior to oxidation. Thus we infer that thin layer effects possibly dominate in this case.

3.7 Conclusion

We have presented a combination of simulations and experiments to show that the modification of an electrode with porous layers of conducting material can shift voltammetric peaks in an analytically useful manner. Moreover the survey of the literature has shown a vast accumulation of data in which modified electrodes aimed at the selective detection of dopamine in the presence of other biological molecules *may* operate, at least in part, by the change of diffusional regime rather than alteration of electrode kinetics. The implications for the design, characterisation and use of chemically modified electrodes, especially deploying polymer films or layers of carbon nanotubes, is evident.

Bibliography

[1] M. C. Henstridge, E. J. F. Dickinson, M. Aslanoglu, C. Batchelor-McAuley and R. G. Compton, *Sens. Actuat. B* **145** (2010) 417–427.

[2] G. G. Wildgoose, C. E. Banks, H. C. Leventis and R. G. Compton, *Microchim. Acta* **152** (2006) 187–214.

[3] A. Walcarius, *Electroanalysis* **20** (2008) 711–738.

[4] L. G. Shaidarova and G. K. Budnikov, *J. Anal. Chem.* **63** (2008) 922–942.

[5] C. Mousty, *Appl. Clay Sci.* **27** (2004) 159–177.

[6] S. E. Ward Jones and R. G. Compton, *Curr. Anal. Chem.* **4** (2008) 177–182.

[7] S. Griese, D. K. Kampouris, R. O. Kadara and C. E. Banks, *Electroanalysis* **20** (2008) 1507–1512.

[8] J. J. Gooding, *Electroanalysis* **20** (2008) 573–582.

[9] M. J. Esplandiu, M. Pacios, E. Bellido and M. Valle, *Z. Phys. Chem.* **221** (2007) 1161–1173.

[10] E. Chow and J. J. Gooding, *Electroanalysis* **18** (2006) 1437–1448.

[11] S. V. Aurobind, K. P. Amirthalingam and H. Gomathi, *Adv. Colloid Interface Sci.* **121** (2006) 1–7.

[12] A. A. Ensafi, M. Taei and T. Khayamian, *J. Electroanal. Chem.* **633** (2009) 212–220.

[13] X. Zhu and X. Lin, *Chin. J. Chem.* **27** (2009) 1103–1109.

[14] Y. Z. Zhou, L. J. Zhang, S. L. Chen, S. Y. Dong and X. H. Zheng, *Chin. Chem. Lett.* **20** (2009) 217–220.

[15] S. Lupu, *Rev. Roum. Chim.* **50** (2005) 213–218.

[16] J. Chou, T. J. Ilgen, S. Gordon, A. D. Ranasinghe, E. W. McFarland, H. Metiu and S. K. Buratto, *J. Electroanal. Chem.* **632** (2009) 97–101.

[17] L. Zhou, F. Shang, M. Pravda, J. D. Glennon and J. H. T. Luong, *Electroanalysis* **21** (2009) 797–803.

[18] R. Zhang, G.-D. Jin, D. Chen and X.-Y. Hu, *Sens. Actuat. B* **B138** (2009) 174–181.

[19] S. Shahrokhian and H. R. Zare-Mehrjardi, *Electroanalysis* **21** (2009) 157–164.

[20] X. Huang, Y. Li, P. Wang and L. Wang, *Anal. Sci.* **24** (2008) 1563–1568.

[21] W. Hu, D. Sun and W. Ma, *Chem. Anal.* **53** (2008) 703–716.

[22] S. Harish, J. Mathiyarasu, K. L. N. Phani and V. Yegnaraman, *J. Appl. Electrochem.* **38** (2008) 1583–1588.

[23] L. Lin, J. Chen, H. Yao, Y. Chen, Y. Zheng and X. Lin, *Bioelectrochemistry* **73** (2008) 11–17.

[24] T. Luczak, *Electrochim. Acta* **53** (2008) 5725–5731.

[25] M. Aslanoglu, S. Abbasoglu, S. Karabulut and A. Kutluay, *Acta Chim. Slov.* **54** (2007) 834–839.

[26] H. Yao, Y. Sun, X. Lin, Y. Tang and L. Huang, *Electrochim. Acta* **52** (2007) 6165–6171.

[27] X. Lin, Y. Zhang, W. Chen and P. Wu, *Sens. Actuat. B* **B122** (2007) 309–314.

[28] W. Ma and D. M. Sun, *Russ. J. Electrochem.* **43** (2007) 1382–1389.

[29] Y. Zhang, S. Su, Y. Pan, L. Zhang and Y. Cai, *Ann. Chim.* **97** (2007) 665–674.

[30] N. B. Li, W. Ren and H. Q. Luo, *Electroanalysis* **19** (2007) 1496–1502.

[31] X. Lin, Q. Zhuang, J. Chen, S. Zhang and Y. Zheng, *Sens. Actuat. B* **B125** (2007) 240–245.

[32] S. R. Jeyalakshmi, S. S. Kumar, J. Mathiyarasu, K. L. N. Phani and V. Yegnaraman, *Indian J. Chem.* **46A** (2007) 957–961.

[33] B. Fang, H. Liu, G. Wang, Y. Zhou, S. Jiao and X. Gao, *J. Appl. Polym. Sci.* **104** (2007) 3864–3870.

[34] X. Jiang and X. Lin, *Anal. Chim. Acta* **537** (2005) 145–151.

[35] J. Chen, J. Zhang, X. Lin, H. Wan and S. Zhang, *Electroanalysis* **19** (2007) 612–615.

[36] A. I. Gopalan, K.-P. Lee, K. M. Manesh, P. Santhosh, J. H. Kim and J. S. Kang, *Talanta* **71** (2007) 1774–1781.

[37] G. Kang and X. Lin, *Electroanalysis* **18** (2006) 2458–2466.

[38] P. F. Huang, L. Wang, J. Y. Bai, H. J. Wang, Y. Q. Zhao and S. D. Fan, *Microchim. Acta* **157** (2007) 41–47.

[39] Q. Wan, X. Wang, X. Wang and N. Yang, *Polymer* **47** (2006) 7684–7692.

[40] Y. Li and X. Lin, *Sens. Actuat. B* **B115** (2006) 134–139.

[41] D. Bouchta, N. Izaoumen, H. Zejli, M. El Kaoutit and K. R. Temsamani, *Anal. Lett.* **38** (2005) 1019–1036.

[42] R. De Cassia Silva Luz, F. Santos Damos, A. Bof de Oliveira, J. Beck and L. T. Kubota, *Electrochim. Acta* **50** (2005) 2675–2683.

[43] Y. Zhang, G. Jin, W. Cheng and S. Li, *Front. Biosci.* **10** (2005) 23–29.

[44] R. A. D Toledo, M. C. Santos, E. T. G. Cavalheiro and L. H. Mazo, *Anal. Bioanal. Chem.* **381** (2005) 1161–1166.

[45] Y. Chen, J. Yuan, X. Wang and C. Tian, *Anal. Sci.* **20** (2004) 1725–1728.

[46] Y. Yang, C.-X. Lei, Z.-M. Liu, Y.-L. Liu, G.-L. Shen and R.-Q. Yu, *Anal. Lett.* **37** (2004) 2267–2282.

[47] T. Selvaraju and R. Ramaraj, *J. Appl. Electrochem.* **33** (2003) 759–762.

[48] P. R. Roy, T. Okajima and T. Ohsaka, *Bioelectrochemistry* **59** (2003) 11–19.

[49] H. Zhao, Y. Zhang and Z. Yuan, *Electroanalysis* **14** (2002) 1031–1034.

[50] M. M. Davila, M. P. Elizalde, J. Mattusch and R. Wennrich, *Electrochim. Acta* **46** (2001) 3189–3197.

[51] H. Zhao, Y. Zhang and Z. Yuan, *Anal. Chim. Acta* **441** (2001) 117–122.

[52] M. D. Rubianes and G. A. Rivas, *Anal. Chim. Acta* **440** (2001) 99–108.

[53] H. Zhao, Y. Zhang and Z. Yuan, *Analyst* **126** (2001) 358–360.

[54] E. Sezer, O. Yavuz and A. S. Sarac, *J. Electrochem. Soc.* **147** (2000) 3771–3774.

[55] G. Erdogdu, E. Ekinci and A. E. Karagozler, *Polym. Bull.* **44** (2000) 195–201.

[56] H. Ju, J. Ni, Y. Gong, H. Chen and D. Leech, *Anal. Lett.* **32** (1999) 2951–2964.

[57] Z. Gao and H. Huang, *Chem. Commun.* 2107–2108.

[58] Y. Sun, B. Ye, W. Zhang and X. Zhou, *Anal. Chim. Acta* **363** (1998) 75–80.

[59] H. Y. Chen, A. M. Yu and H. L. Zhang, *J. Anal. Chem.* **358** (1997) 863–864.

[60] A.-M. Yu, D.-M. Sun and H.-Y. Chen, *Anal. Lett.* **30** (1997) 1643–1652.

[61] G. Erdogdu, J. Mark, H. B. and A. E. Karagozler, *Anal. Lett.* **29** (1996) 221–231.

[62] O. Niwa, M. Morita and H. Tabei, *Electroanalysis* **6** (1994) 237–243.

[63] G. Alarcon-Angeles, B. Perez-Lopez, M. Palomar-Pardave, M. T. Ramirez-Silva and A. Alegret, S.; Merkoci, *Carbon* **46** (2008) 898–906.

[64] H. Boo, R.-A. Jeong, S. Park, K. S. Kim, K. H. An, Y. H. Lee, J. H. Han, H. C. Kim and T. D. Chung, *Anal. Chem.* **78** (2006) 617–620.

[65] L. C. Jiang and W. D. Zhang, *Electroanalysis* **21** (2009) 1811–1815.

[66] Y. Sun, J. Fei, J. Hou, Q. Zhang, Y. Liu and B. Hu, *Microchim. Acta* **165** (2009) 373–379.

[67] G. Li and J. Hao, *J. Electrochem. Soc.* **159** (2009) 134–138.

[68] M. C. Rodriguez, M. D. Rubianes and G. A. Rivas, *J. Nanosci. Nanotechnol.* **8** (2008) 6003–6009.

[69] N. Punbusayakul, L. Ci, S. Talapatra, W. Surareungchai and P. M. Ajayan, *J. Nanosci. Nanotechnol.* **8** (2008) 2085–2090.

[70] F. C. Moraes, M. F. Cabral, S. A. S. Machado and L. H. Mascaro, *Electroanalysis* **20** (2008) 851–857.

[71] U. Yogeswaran and S.-M. Chen, *Sens. Actuat. B* **B130** (2008) 739–749.

[72] S. Jo, H. Jeong, S. R. Bae and S. Jeon, *Microchem. J.* **88** (2008) 1–6.

[73] S. Jiao, M. Li, C. Wang, D. Chen and B. Fang, *Electrochim. Acta* **52** (2007) 5939–5944.

[74] N. Punbusayakul, S. Talapatra, L. Ci, W. Surareungchai and P. M. Ajayan, *Electrochem. Solid-State Lett.* **10** (2007) F13–F17.

[75] M. D. Rubianes and G. A. Rivas, *Electrochem. Commun.* **9** (2007) 480–484.

[76] Y. Zhang, Y. Pan, S. Su, L. Zhang, S. Li and M. Shao, *Electroanalysis* **19** (2007) 1695–1701.

[77] H.-S. Wang, T.-H. Li, W.-L. Jia and H.-Y. Xu, *Biosens. Bioelectron.* **22** (2006) 664–669.

[78] S. B. Hocevar, J. Wang, R. P. Deo, M. Musameh and B. Ogorevc, *Electroanalysis* **17** (2005) 417–422.

[79] K. Wu and S. Hu, *Microchim. Acta* **144** (2004) 131–137.

[80] Z. Wang, J. Liu, Q. Liang, Y. Wang and G. Luo, *Analyst* **127** (2002) 653–658.

[81] C. G. Hu, W. L. Wang, K. J. Liao and W. Zhu, *Acta Metall. Sin.* **16** (2003) 289–294.

[82] M. Bahram, K. Farhadi and F. Arjmand, *Cent. Eur. J. Chem.* **7** (2009) 524–531.

[83] S. Thiagarajan, T.-H. Tsai and S.-M. Chen, *Biosens. Bioelectron.* **24** (2009) 2712–2715.

[84] S. C. Avendano, G. A. Angeles, A. R. Hernandez, M. T. Ramirez-Silva, M. A. R. Romo, G. A. R. Pina and M. P. Pardave, *ECS Trans.* **3** (2007) 23–29.

[85] R. T. Kachoosangi and R. G. Compton, *Anal. Bioanal. Chem.* **387** (2007) 2793–2800.

[86] N. J. Ke, S.-S. Lu and S.-H. Cheng, *Electrochem. Commun.* **8** (2006) 1514–1520.

[87] L. Kaoqi and S. Hanwen, *Chemistry* **3** (2006) 11–18.

[88] A. P. dos Reis, C. R. T. Tarley, N. Maniasso and L. T. Kubota, *Talanta* **67** (2005) 829–835.

[89] X.-L. Wen, Y.-H. Jia and Z.-L. Liu, *Talanta* **50** (1999) 1027–1033.

[90] S. Hafizi, Z. L. Kruk and J. A. Stamford, *J. Electroanal. Chem.* **283** (1990) 125–33.

[91] W. Wang, Q. Wang and Z. Zhang, *J. Nanopart. Res.* **10** (2008) 255–262.

[92] P. Wang, Y. Li, X. Huang and L. Wang, *Talanta* **73** (2007) 431–437.

[93] L. Zhang and X. Jiang, *J. Electroanal. Chem.* **583** (2005) 292–299.

[94] K. Farhadi, F. Kheiri and M. M. Golzan, *J. Chin. Chem. Soc.* **55** (2008) 1034–1041.

[95] M. Zhou, J. Guo, L.-p. Guo and J. Bai, *Anal. Chem.* **80** (2008) 4642–4650.

[96] M. A. Kamyabi, Z. Asgari, H. Hosseini Monfared and A. Morsali, *J. Electroanal. Chem.* **632** (2009) 170–176.

[97] R. Hosseinzadeh, R. E. Sabzi and K. Ghasemlu, *Colloids Surf., B* **68** (2009) 213–217.

[98] K. Farhadi, F. Kheiri and M. Golzan, *J. Braz. Chem. Soc.* **19** (2008) 1405–1412.

[99] J. Huang, Y. Liu, H. Hou and T. You, *Biosens. Bioelectron.* **24** (2008) 632–637.

[100] G. Alarcon-Angeles, S. Corona-Avendano, M. Palomar-Pardave, A. Rojas-Hernandez, M. Romero-Romo and M. T. Ramirez-Silva, *Electrochim. Acta* **53** (2008) 3013–3020.

[101] W. Sun, M. Yang and K. Jiao, *Anal. Bioanal. Chem.* **389** (2007) 1283–1291.

[102] R. N. Goyal, V. K. Gupta, N. Bachheti and R. A. Sharma, *Electroanalysis* **20** (2008) 757–764.

[103] J. Zheng and X. Zhou, *Bioelectrochemistry* **70** (2007) 408–415.

[104] A. Safavi, N. Maleki, O. Moradlou and F. Tajabadi, *Anal. Biochem.* **359** (2006) 224–229.

[105] G.-J. Yang, J.-J. Xu, K. Wang and H.-Y. Chen, *Electroanalysis* **18** (2006) 282–290.

[106] J.-B. Raoof, R. Ojani and A. Kiani, *Bull. Electrochem.* **21** (2005) 223–228.

[107] J.-B. Raoof, R. Ojani and S. Rashid-Nadimi, *Electrochim. Acta* **50** (2005) 4694–4698.

[108] H. R. Zare, N. Nasirizadeh and M. Mazloum Ardakani, *J. Electroanal. Chem.* **577** (2005) 25–33.

[109] J. Oni, P. Westbroek and T. Nyokong, *Electroanalysis* **15** (2003) 847–854.

[110] P. A. Broderick, *Neurosci. Lett.* **95** (1988) 275–80.

[111] T. Kondo, Y. Niwano, A. Tamura, J. Imai, K. Honda, Y. Einaga, D. A. Tryk, A. Fujishima and T. Kawai, *Electrochim. Acta* **54** (2009) 2312–2319.

[112] M. Wei, C. Terashima, M. Lv, A. Fujishima and Z.-Z. Gu, *Chem. Commun.* 3624–3626.

[113] Y. Li, X. Huang, Y. Chen, L. Wang and X. Lin, *Microchim. Acta* **164** (2009) 107–112.

[114] Y. Wang, J. Luo, H. Chen, Q. He, N. Gan and T. Li, *Anal. Chim. Acta* **625** (2008) 180–187.

[115] L. Zhang, *Microchim. Acta* **161** (2008) 191–200.

[116] L. Zhang, R. Yuan, Y. Chai and X. Li, *Anal. Chim. Acta* **596** (2007) 99–105.

[117] C. Hsueh, R. Bravo, A. J. Jaramillo and A. Brajter-Toth, *Anal. Chim. Acta* **349** (1997) 67–76.

[118] N. Jia, Z. Wang, G. Yang, H. Shen and L. Zhu, *Electrochem. Commun.* **9** (2007) 233–238.

[119] M. Wang, X. Xu and J. Gao, *J. Appl. Electrochem.* **37** (2007) 705–710.

[120] L. Codognoto, E. Winter, J. A. R. Paschoal, H. B. Suffredini, M. F. Cabral, S. A. S. Machado and S. Rath, *Talanta* **72** (2007) 427–433.

[121] G.-S. Lai, H.-L. Zhang and C.-M. Jin, *Electroanalysis* **19** (2007) 496–501.

[122] H. Wang, L.-J. Wang, Z.-F. Shi, Y. Guo, X.-P. Cao and H.-L. Zhang, *Electrochem. Commun.* **8** (2006) 1779–1783.

[123] U. E. Majewska, K. Chmurski, K. Biesiada, A. R. Olszyna and R. Bilewicz, *Electroanalysis* **18** (2006) 1463–1470.

[124] L. M. Niu, H. Q. Luo and N. B. Li, *Arch. Pharm.* **339** (2006) 356–360.

[125] S. S. Kumar and S. S. Narayanan, *Electrochem. Commun.* **8** (2006) 815–820.

[126] H. R. Zare, N. Rajabzadeh, N. Nasirizadeh and M. Mazloum Ardakani, *J. Electroanal. Chem.* **589** (2006) 60–69.

[127] L. Zhang and X. Lin, *Anal. Bioanal. Chem.* **382** (2005) 1669–1677.

[128] C. Y. Liu, L. Z. Yang, F. Song, L. Y. Jiang and G. H. Lu, *Chin. Chem. Lett.* **16** (2005) 237–240.

[129] J. Kang, L. Zhuo, X. Lu and X. Wang, *J. Solid State Electrochem.* **9** (2005) 114–120.

[130] G.-P. Jin, X.-Q. Lin and J.-M. Gong, *J. Electroanal. Chem.* **569** (2004) 135–142.

[131] T. Liu, M. Li and Q. Li, *Talanta* **63** (2004) 1053–1059.

[132] P. Ramesh, G. S. Suresh and S. Sampath, *J. Electroanal. Chem.* **561** (2004) 173–180.

[133] C. R. Raj, K. Tokuda and T. Ohsaka, *Bioelectrochemistry* **53** (2001) 183–191.

[134] H.-M. Zhang, N.-Q. Li and Z. Zhu, *Microchem. J.* **64** (2000) 277–282.

[135] F. Malem and D. Mandler, *Anal. Chem.* **65** (1993) 37–41.

[136] E. J. F. Dickinson, J. G. Limon-Petersen, N. V. Rees and R. G. Compton, *J. Phys. Chem. C* **113** (2009) 11157–11171.

[137] H. Reller, E. Kirowa-Eisner and E. Gileadi, *J. Electroanal. Chem.* **138** (1982) 65–77.

[138] T. J. Davies, S. Ward Jones, C. E. Banks, J. del Campo, R. Mas, F. X. Muñoz and R. G. Compton, *J. Electroanal. Chem.* **585** (2005) 51–62.

[139] T. J. Davies and R. G. Compton, *J. Electroanal. Chem.* **585** (2005) 63–82.

[140] T. J. Davies, C. E. Banks and R. G. Compton, *J. Solid State Electrochem.* **9** (2005) 797–808.

[141] E. J. F. Dickinson, I. Streeter and R. G. Compton, *J. Phys. Chem. C* **112** (2008) 11637–11644.

[142] M. J. Sims, N. V. Rees, E. J. F. Dickinson and R. G. Compton, *Sens. Actuat. B* **144** (2010) 153–158.

[143] M. Rudolph, D. P. Reddy and S. W. Feldberg, *Anal. Chem.* **66** (1994) 589A–600A.

[144] M. C. Henstridge, E. J. F. Dickinson and R. G. Compton, *Chem. Phys. Lett.* **485** (2010) 167–170.

[145] G. Zou, Z. Liu and C. Wang, *Anal. Chim. Acta* **350** (1997) 359–363.

[146] X. Wang, N. Yang, Q. Wan and X. Wang, *Sens. Actuators, B* **B128** (2007) 83–90.

[147] R. T. Kachoosangi, G. G. Wildgoose and R. G. Compton, *Analyst* **133** (2008) 888–895.

[148] R. T. Kachoosangi, G. G. Wildgoose and R. G. Compton, *Anal. Chim. Acta* **618** (2008) 54–60.

Chapter 4

Mass transport to and within porous electrodes: the prediction of double peaks for a single electrode process

We simulate an electrode modified with a conducting porous film, where the electrolysis occurs both at the surface of the film and within it, in order to study the effect of pore size on the peak current in linear sweep voltammetry. For redox systems with reversible electrode kinetics we find that for both very large and very small pores the peak current is given by the Randles-Ševčík equation. For intermediate pore size, however, we observe a greatly enhanced peak current. When considering systems with irreversible electrode kinetics a very similar pattern is observed, except for the case of very small pores. In this case the peak current is actually smaller than expected from the Randles-Ševčík equation because the peak splits into two distinct peaks: one due to 'thin layer' diffusion within the film and another caused by planar diffusion from bulk solution. The experimental implications of this observation are significant given the widespread use of modified electrodes for analysis.

This work has been published in the *Russian Journal of Electrochemistry* [1]. The simulations described below were carried out using a program written by E. J. F. Dickinson.

4.1 Introduction

Electroanalysis using voltammetric methods offers a highly sensitive, precise method for the determination of a wide variety of analytes. In many cases, however, there may be other substances present in solution which may be oxidised or reduced at potentials close to the target system, thus interfering with the signal of interest. A highly successful strategy for the determination of analytes in the presence of such interferents has been the use of electrodes modified with a porous film, such as those discussed in the previous chapter.

In the previous chapter we studied the determination of dopamine employing a combination of simulation and experiment: demonstrating that the enhanced selectivity exhibited by numerous modified electrodes may be explained, at least partly, by a change in mass transport regime rather than by enhanced electrocatalytic activity [10]. Increased 'thin layer' diffusion at modified electrodes, due to increasing film thickness, causes the dopamine oxidation peak to shift to lower overpotentials relative to the unmodified electrode at which planar diffusion operates exclusively.

In this chapter we investigate how the presence of a porous film affects the voltammetric peak current. We consider both reversible and irreversible electrode kinetics and measure the peak current as a function of pore size for different values of film thickness.

4.2 Theory

The theoretical model used for the simulations described here is the same as that used in Chapter 3: the porous film is modeled as a regular array of vertically aligned cylinders protruding from a planar electrode surface. The one-electron oxidation $\mathrm{A} - \mathrm{e} \rightleftharpoons \mathrm{B}$ takes place at the surface of the cylinders as well as at the underlying electrode base. Linear sweep voltammetry is simulated using the diffusion domain approximation and the ADI finite difference method [3–5].

We consider a reversible redox couple with $K_0 = 10^4$ and an irreversible redox couple with $K_0 = 10^{-4}$, for both couples $\alpha = 0.5$. The diffusion coefficients for both A and B are set to $1 \times 10^{-5}\,\mathrm{cm}^2\,\mathrm{s}^{-1}$ and the cylinder radius is set to 20 nm, a value typical for the external radius of a multi-walled carbon nanotube. All voltammetry was simulated for a dimensionless scan rate of 10^{-2}.

Since the size of the simulation space, and hence the electroactive surface area, is dependent upon R_{max}; the current must be scaled in order to allow meaningful comparison between different array geometries. The current values reported here are therefore scaled by a factor of R_{max}^{-2}.

The theoretical peak current in the limits of both low and high cylinder separation is given by the Randles-Ševčík equation. In dimensionless units, the reversible [6, 7] and irreversible versions [8] of the Randles-Ševčík equation for a one-electron redox process are:

$$\text{Reversible electrode kinetics}: \qquad J_{\mathrm{p}} = 0.2232\sqrt{\sigma} \tag{4.1}$$

$$\text{Irreversible electrode kinetics}: \qquad J_{\mathrm{p}} = 0.2479\sqrt{\alpha\sigma} \tag{4.2}$$

This can be rationalised by considering that in the limit $R_{\mathrm{max}} \to \infty$ there are a vanishingly small number of cylinders on the electrode surface and the overall electrode geometry approximates that of a planar macroelectrode. Thus the mass transport tends towards planar diffusion and the peak current is given by the Randles-Ševčík equation. In the limit $R_{\mathrm{max}} \to 1$ there are many cylinders on the electrode surface, but the spaces between cylinders become vanishingly small and the electrode again begins to resemble a planar macroelectrode.

4.3 Results and discussion

4.3.1 Reversible kinetics

Linear sweep voltammetry was simulated for the reversible system over a wide range of cylinder separation. The variation of peak current with R_{max} is shown in Figure 4.1 for Z_{e} = 30, 100 and 300. As expected the peak current is seen to reach to the Randles-Ševčík limit (Equation (4.1)) for very high cylinder separation. As the separation decreases the total number of cylinders on the electrode surface increases and so the (scaled) peak current increases due to the increased total conductive surface area.

As separation decreases further, however, the peak current reaches a maximum and begins to decrease again. Despite the surface area increasing, the ‘diffusion fields’ of the cylinders begin to overlap and the space between the cylinders in which ‘thin layer’ diffusion operates becomes depleted of species A – leading to a decrease in peak current.

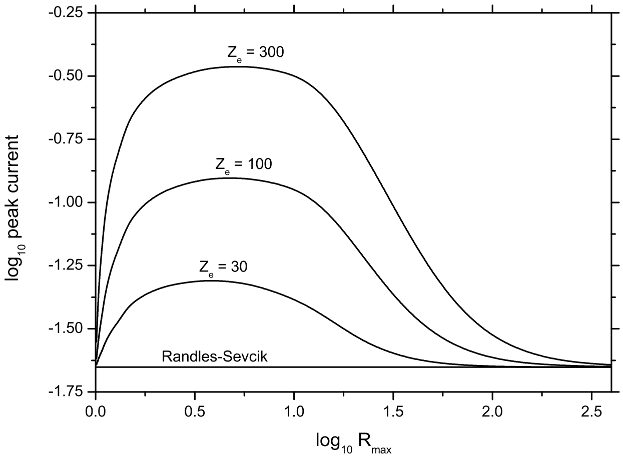

Figure 4.1: Plot of scaled peak current against $R_{\max}$ for a reversible redox couple.

For very small cylinder spacing the current contributed by diffusion to the sides of the cylinders becomes negligibly small and the peak current once more tends to the Randles-Ševčík limit as planar diffusion dominates.

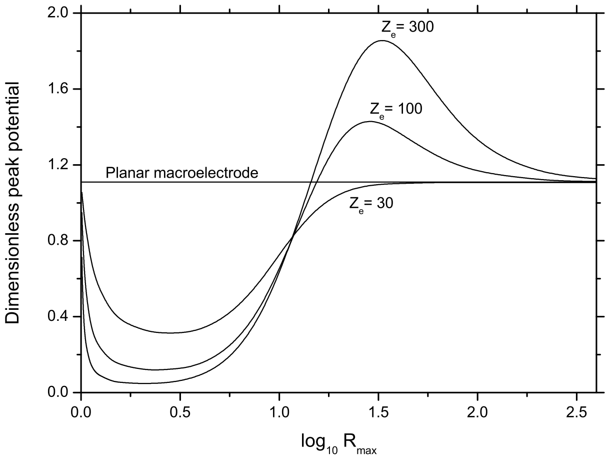

Figure 4.2: Plot of peak potential against $R_{\max}$ for a reversible system.

The variation of peak potential with $R_{\max}$ is shown in Figure 4.2. As was the case for the peak current, at both very high and very low cylinder separation (when planar diffusion dominates) the modified electrode is seen to approximate a planar macroelectrode.

At high cylinder separation the peak is at higher overpotential than for a macroelectrode due to the enhanced mass transport effected by increased 'thin layer' diffusion. Thus mass transport does not become rate limiting as quickly as is the case for a planar macroelectrode when planar diffusion operates exclusively.

As cylinder separation decreases the peak moves to lower overpotentials as 'thin layer' diffusion begins to dominate and species A is quickly consumed from the small volume of solution between the cylinders. At very small R_{max} the peak potential again tends to the planar macroelectrode limit as the distance between cylinders becomes negligibly small. A typical concentration profile for the reversible system ($Z_{\mathrm{e}} = 300$, $R_{\mathrm{max}} = 30$) is shown in Figure 4.3.

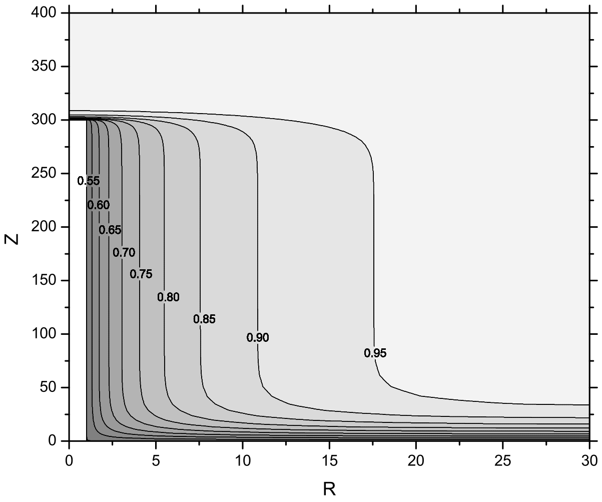

Figure 4.3: Concentration profile recorded at the peak potential of the reversible couple. $Z_{\mathrm{e}} = 300$ and $R_{\mathrm{max}} = 30$.

4.3.2 Irreversible kinetics

Simulated voltammetry for a system with irreversible electrode kinetics reveals a similar pattern, as shown in Figure 4.4. For very large R_{max} the peak current is given by Equation (4.2) and at intermediate cylinder separation there is again an enhanced peak current due to the increased surface area at which electron transfer can occur.

At very low cylinder separation, however, the peak current is actually smaller than is expected from the Randles-Ševčík equation. This is because for small R_{max} the voltammetric wave actually splits into two peaks: one at very low overpotentials due to 'thin layer' diffusion and another at much larger overpotentials due to planar diffusion from bulk solution. This phenomenon is shown in Figure 4.5.

For very small R_{max} the peak due to 'thin layer' diffusion is smaller than the peak from

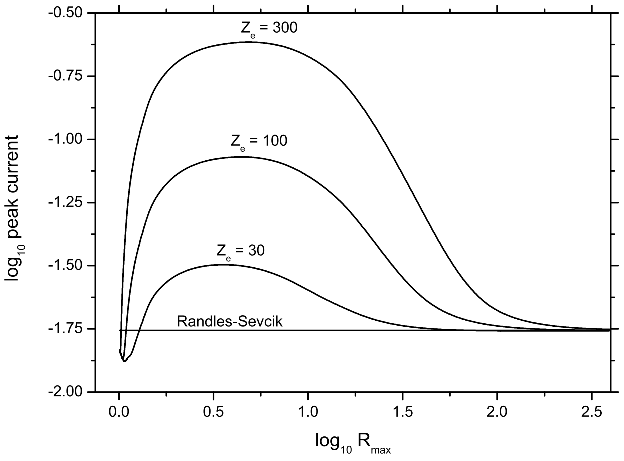

Figure 4.4: Plot of scaled peak current against $R_{\max}$ for an irreversible redox couple.

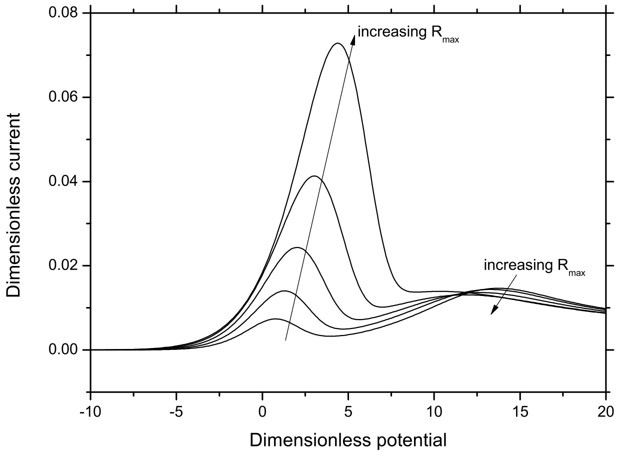

Figure 4.5: Simulated voltammetry showing splitting of the peak into separate 'thin layer' and planar diffusion peaks. $Z_e = 300$, $R_{\max} = 1.01$, 1.02, 1.04, 1.08 and 1.16.

planar diffusion, but as $R_{\max}$ increases the 'thin layer' peak grows relative to the 'planar diffusion' peak, the two peaks begin to move closer together and eventually merge.

The appearance of two peaks could potentially lead some to mistakenly conclude that there are two species present in solution, especially considering the large difference in peak potentials. We stress, however, that the two peaks are caused by different modes of mass transport alone.

This splitting of the voltammetric wave into two separate peaks is not observed for reversible kinetics. For a reversible system at a planar macroelectrode the peak separation is expected to be approximately 57 mV, and so the oxidative peak occurs at around +29 mV. This is very close to the peak potential expected from pure 'thin layer' diffusion (the limit of which is a species adsorbed at an electrode surface), which yields a forward peak at 0 mV. Thus these peaks are too close together to ever be observed as two distinct waves. This is only possible for irreversible systems because of the large difference in potentials between the 'thin layer' peak and the peak due to planar diffusion.

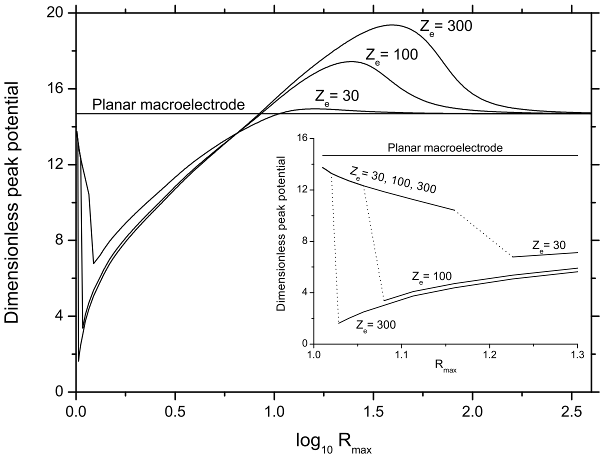

Figure 4.6: Plot of peak potential against $R_{\max}$ for a reversible system. Data is plotted for different values of film thickness with the peak potential for a planar macroelectrode plotted for comparison. Inset shows magnification of the switchover between the 'thin layer' peak being largest at higher $R_{\max}$ and the bulk planar diffusion peak being largest for small $R_{\max}$.

The variation of peak potential with $R_{\max}$ for a kinetically irreversible system is shown in Figure 4.6. It is qualitatively similar to the equivalent plot for reversible kinetics. The peak potential again tends to the planar macroelectrode limit for both high and low cylinder separation. For irreversible kinetics, however, a sharp discontinuity occurs at very low separation. This is caused by the splitting of the peak and the switch between the planar diffusion peak being the larger of the two at low R_{max} and the 'thin layer' peak becoming the larger at higher values.

Within the diffusion domain approximation the area of the cylindrical unit cell is taken to be equal to the area of the original unit cell which it approximates. Thus, in the limit of hexagonal close-packed cylinders, R_{max} takes a minimum value of 1.05. While some values of R_{max} considered here are smaller than this limit, this model is likely still applicable to real systems in which the film on the electrode consists, not of cylinders protruding from a surface, but of small pores reaching into the surface.

Experimentally, porous electrodes suffer from a decreased signal to noise ratio when compared with planar electrodes. The signal, given by the Faradaic current, varies as discussed above whereas the noise, due to capacitance, varies primarily with the electroactive surface area. A more detailed theoretical treatment of the capacitance at isolated nanomaterials [9] and isolated nanotubes [2] can be found in the literature; however the case of overlapping diffusion fields has yet to undergo such treatment and so the exact variation of the signal to noise ratio may not currently be predicted for porous electrodes.

4.4 Conclusion

We have presented simulations using a simple model to approximate an electrode modified with a porous film. For systems exhibiting reversible electrode kinetics Randles-Ševčík behaviour is observed at both very high and very low cylinder separation with a greatly enhanced peak current being seen at intermediate separation which is dependent on the film thickness. For irreversible kinetics a very similar pattern is observed, except at very small cylinder separation for which the oxidative wave is split into two distinct peaks: one due to 'thin layer' diffusion and another caused by planar diffusion from bulk solution.

Bibliography

[1] M. C. Henstridge, E. J. F. Dickinson and R. G. Compton, *Russ. J. Electrochem.* **48** (2012) 629–635.

[2] M. C. Henstridge, E. J. F. Dickinson and R. G. Compton, *Chem. Phys. Lett.* **485** (2010) 167–170.

[3] T. J. Davies, C. E. Banks and R. G. Compton, *J. Solid State Electrochem.* **9** (2005) 797–808.

[4] T. J. Davies and R. G. Compton, *J. Electroanal. Chem.* **585** (2005) 63–82.

[5] T. J. Davies, S. Ward Jones, C. E. Banks, J. del Campo, R. Mas, F. X. Muñoz and R. G. Compton, *J. Electroanal. Chem.* **585** (2005) 51–62.

[6] J. E. B. Randles, *Trans. Faraday Soc.* **44** (1948) 327–338.

[7] A. Sevcik, *Collect. Czechoslov. Chem. Commun.* **13** (1948) 349.

[8] P. Delahay, *J. Am. Chem. Soc.* **75** (1953) 1190–1196.

[9] E. J. F. Dickinson and R. G. Compton, *J. Phys. Chem. C* **113** (2009) 17585–17589.

[10] M. C. Henstridge, E. J. F. Dickinson, M. Aslanoglu, C. Batchelor-McAuley and R. G. Compton, *Sens. Actuat. B* **145** (2010) 417–427.

Chapter 5

The symmetric Marcus-Hush model of electrode kinetics

The so-called Marcus-Hush model of electron transfer is introduced as an alternative to the Butler-Volmer model and is developed into a form applicable to heterogeneous electron transfer at a metallic electrode. The basic characteristics of this model are examined and a brief review of previous work in the field is presented.

This chapter is based on a review article in press at *Electrochimica Acta* [1], co-authored with E. Laborda and N. V. Rees.

5.1 Introduction

As described in Chapter 1, the Butler-Volmer kinetic formalism is ubiquitous as a model for parameterising electrode kinetics. Since its inception in the early 20th century, this model has been employed in the analysis of countless redox systems and has proved enormously successful – largely due to the simplicity of its application and its flexibility. This model, however, remains purely empirical in nature and thus the underlying physical process may not be rationalised on the basis of the values of k_0 and α, other than a possible indication of the 'position' of the transition state.

An alternative model is that attributed to Marcus [2] which is based on a microscopic consideration of the electron transfer process. The rate of electron transfer is related to an activation energy ($\Delta G^{\ddagger}$) via an Arrhenius-type equation:

$$k = A \exp\left[\frac{-\Delta G^{\ddagger}}{RT}\right] \tag{5.1}$$

where k is a rate constant and A is a pre-exponential factor.

The Gibbs energy surfaces of both reactant and product are assumed to be parabolic and the transition state, and hence activation energy, is determined by the intersection of the two curves.

$$\Delta G^{\ddagger} = \frac{\lambda}{4}\left(1 + \frac{\Delta G^{\ominus}}{\lambda}\right)^2 \tag{5.2}$$

The activation energy is a function of the reaction Gibbs energy ($\Delta G^{\ominus}$) and a 'reorganisation energy' (λ), defined as the energy required to distort the atomic configurations of the reactant molecule and its solvation shell to those of the product in its equilibrium configuration. Electron transfer is considered to take place once reorganisation has taken place in a radiationless transition in accordance with the Franck-Condon principle [3].

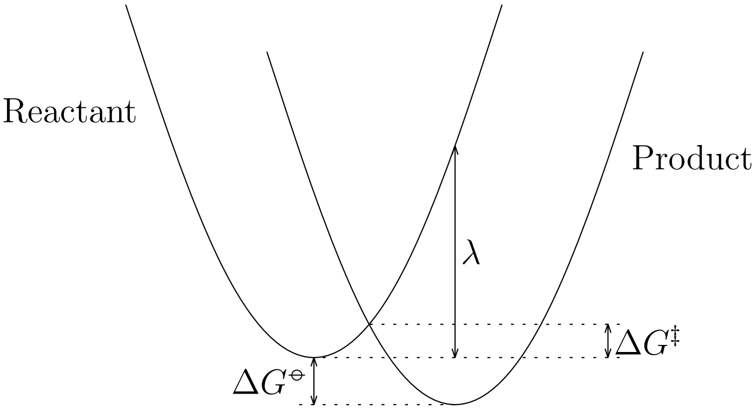

Figure 5.1: Gibbs energy curves of reactant and product molecules as given by Marcus theory for a homogeneous electron transfer.

These ideas are summarised in Figure 5.1 which shows a schematic of the parabolic Gibbs energy curves for a homogeneous electron transfer, that is electron transfer between two species in solution. If we consider heterogeneous electron transfer (*i.e.* electron transfer between a donor and acceptor which are in different phases), such as between a molecule in solution and a metallic electrode, then this diagram represents an oversimplification. Due to the band structure of the metal, each parabolic Gibbs energy curve becomes a band of parabolae such that there is a range of activation energies. This is discussed in more detail below.

Marcus' original work was concerned with outer-sphere homogeneous electron transfer [4–7], but around the same time Hush extended the model to encompass inner-sphere electron transfer [8, 9]. Fletcher has also recently highlighted [10] the importance of earlier work by Randles [11] in the development of this theory.

5.2 Reorganisation energy

The reorganisation energy can be divided into distinct inner-sphere and outer-sphere contributions. The inner-sphere reorganisation energy (λ_i) encompasses the intramolecular changes in bond lengths and angles and can be estimated by summing over the vibrational modes of the species:

$$\lambda_\mathrm{i} = \frac{1}{2}\sum_j k_j \left(q_\mathrm{B} - q_\mathrm{A}\right)^2 \tag{5.3}$$

where k_j are the force constants for each oscillator and q is displacement.

The outer-sphere reorganisation energy (λ_o) encompasses the changes in the position and orientation of nearby solvent molecules. For heterogeneous electron transfer this may be calculated using:

$$\lambda_\mathrm{o} = \frac{e^2}{8\pi\epsilon_0}\left(\frac{1}{r} - \frac{1}{2d}\right)\left(\frac{1}{\epsilon_\mathrm{op}} - \frac{1}{\epsilon_\mathrm{s}}\right) \tag{5.4}$$

along with the spherical approximation of the Stokes-Einstein equation:

$$r = \frac{k_\mathrm{B}T}{6\pi\eta D} \tag{5.5}$$

where e is the elementary charge, ϵ_0 is the permittivity of free space, d is the distance between reactant and electrode surface, ϵ_op and ϵ_s are the optical and static components of the dielectric permittivity of the solvent respectively, r is the solvodynamic radius of the molecule, η is the solvent viscosity and D is the diffusion coefficient.

5.3 Experimental verification

One of the most striking predictions of Marcus theory is that of the so-called inverted region for homogeneous electron transfer reactions. Examination of Equation (5.2) reveals that there is zero activation energy when $\Delta G^\ominus = -\lambda$. Further increasing the thermodynamic driving force results in an increase in the activation energy and thus a reduced rate of electron transfer. This result seems counter-intuitive, yet it has been observed experimentally [12].

Work by Savéant and Tessier [13–15] on the reduction of various nitro-compounds used convolution potential sweep voltammetry to determine the variation of the heterogeneous electron transfer rate constant with potential. This gave the first experimental evidence of a potential-dependent transfer coefficient as predicted by Marcus theory, with the magnitude of the variation also seen to be consistent with the Marcusian model. Subsequent work by Corrigan and Evans [16] successfully used a variable transfer coefficient (quantified by a $\frac{\mathrm{d}\alpha}{\mathrm{d}E}$ value) in the fitting cyclic voltammetry for the reduction of tert-nitrobutane.

Later refinements to the theory on the basis of the 'encounter pre-equilibrium' suggested that in the limit of weak overlap and assuming $\lambda_\mathrm{o} \gg \lambda_\mathrm{i}$, the standard rate constant is inversely proportional to the longitudinal dielectric relaxation time. This relationship has been observed for several outer-sphere heterogeneous electron transfers [17–22] in a wide range of solvents and solvent mixtures. Further, since dielectric relaxation time is directly proportional to solvent viscosity, k_0 has also been seen to vary inversely with solvent viscosity [23, 24].

The standard rate constant is also a function of molecular size, through its influence on the outer-sphere reorganisation energy (Equation (5.4)). Experiments employing a channel microband electrode operating under high mass transport conditions have confirmed the theoretical relationship between k_0 and the solvodynamic radius, a_s [21, 22, 25, 26].

5.4 Heterogeneous electron transfer

We consider a one-electron reduction occurring at the surface of a metallic electrode. Due to the band structure of the metal, electron transfer occurs between the molecules in solution and a whole continuum of electrode energy levels and so the reaction Gibbs energy becomes a function of the energy of the particular metallic state participating in electron transfer. Consequently (see Equation (5.2)) the activation energy for a given metallic state, i, is now given by:

$$\Delta G^{\ddagger}_{\mathrm{red/ox}}(\epsilon_i) = \frac{\lambda}{4}\left[1 \pm \frac{F(\epsilon_i - E^{\ominus}_\mathrm{f})}{\lambda}\right] \tag{5.6}$$

where $F\epsilon_i$ is the energy of state i. Where two signs appear, the upper sign refers to reduction and the lower sign refers to oxidation.

The overall rate of electron transfer is then a sum of the rates of electron transfer for each electronic state of the electrode, weighted by the probability of occupancy (f_+) or vacancy (f_-) of that state [27]:

$$k_{\text{red/ox}} = \sum_i f_\pm(\epsilon_i)\ A(\epsilon_i)\ \exp\left[\frac{-\Delta G^\ddagger_{\text{red/ox}}(\epsilon_i)}{RT}\right] \tag{5.7}$$

where $f_\pm(\epsilon_i)$ is given by the Fermi-Dirac distribution:

$$f_\pm(\epsilon_i) = \frac{1}{1 + \exp\left[\pm\frac{F}{RT}(\epsilon_i - E)\right]} \tag{5.8}$$

If we assume that $A(\epsilon_i)$ is independent of energy we may re-write Equation (5.7) as an integral:

$$k_{\text{red/ox}} = A\int_{-\infty}^{\infty} f_\pm(\epsilon)\ \exp\left[\frac{-\Delta G^\ddagger_{\text{red/ox}}(\epsilon)}{RT}\right] d\epsilon \tag{5.9}$$

As discussed in [27], in making this approximation we assume that both the density of metallic states (ρ) and coupling between the reactant molecule and the electrode ($\bar{H}^2_{\text{DA}}$) are independent of energy. These assumptions are nevertheless validated by comparison to experiment.

We then define k_0 as the rate constant at the formal potential and obtain the following general expressions for the electron transfer rate constants:

$$k_{\text{red}} = k_0\,\frac{S_{\text{red}}(\theta,\Lambda)}{S_{\text{red}}(0,\Lambda)} \tag{5.10}$$

$$k_{\text{ox}} = k_0\,\frac{S_{\text{ox}}(\theta,\Lambda)}{S_{\text{ox}}(0,\Lambda)} \tag{5.11}$$

where θ is dimensionless potential, Λ is the dimensionless reorganisation energy, given by:

$$\Lambda = \frac{F}{RT}\lambda \tag{5.12}$$

and $S_{\text{red/ox}}(\theta, \Lambda)$ is an integral of the form:

$$S_{\text{red/ox}}(\theta, \Lambda) = \int_{-\infty}^{\infty} \frac{\exp\left[-\frac{\Lambda}{4}\left(1 \pm \frac{\theta+x}{\Lambda}\right)^2\right]}{1 + \exp\left[\mp x\right]}\, dx \tag{5.13}$$

where x is a dimensionless integration variable:

$$x = \frac{F}{RT}(\epsilon - E) \tag{5.14}$$

The rate constants given in Equations (5.10) and (5.11) take a convenient form whereby the rate of electron transfer at a given potential can be expressed in terms of three independent variables: $\{E_{\text{f}}^{\ominus}, k_0, \lambda\}$. In reality k_0 is a function several variables, including λ, ρ and $\bar{H}_{\text{DA}}^2$ [28, 29]. However, in the following chapters we seek to evaluate the Marcus-Hush model of electrode kinetics as an alternative to the Butler-Volmer model and as such it is convenient to define k_0 in a manner consistent with the latter in order to retain a three-parameter model. As such we make no a priori assumptions regarding the value of k_0.

5.5 Characteristics of the model

With these expressions for the rate constants we can begin to analyse the behaviour of what we shall refer to as the symmetric Marcus-Hush (SMH) model of electrode kinetics. Figure 5.2 shows the variation of k_{red} and k_{ox} as a function of potential for a range of reorganisation energies (plotted as $\ln k$ against overpotential). The most striking feature of this model is that the rate constants reach a limiting value at large overpotentials. This is in stark contrast to the Butler-Volmer model for which the rate constants continue to increase exponentially *ad infinitum.*

The potential at which the rate constants begin to level off decreases as the reorganisation energy decreases. More quantitatively, Oldham has shown that the rate constant reaches half of its limiting value when $\theta = \Lambda$ [30]. Thus when the reorganisation energy is large, the rate constants continue to increase even for large overpotentials. Feldberg [31] has shown that in the limit $\Lambda \to \infty$ the rate constants given by the symmetric Marcus-Hush model become exactly equivalent to those given by the Butler-Volmer model for

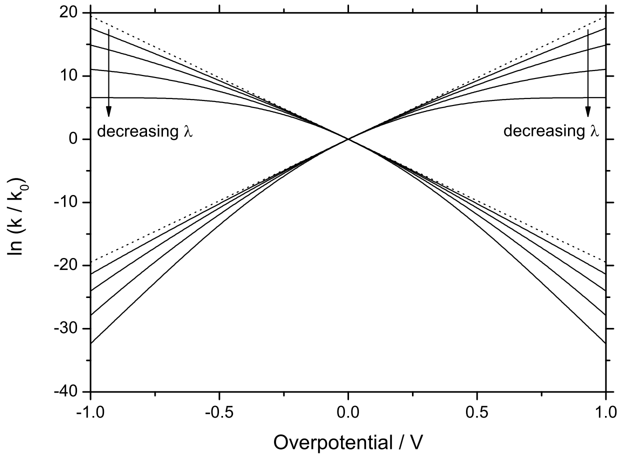

Figure 5.2: Plot of $\ln(k/k_0)$ against overpotential for the symmetric Marcus-Hush model for a range of reorganisation energies ($\lambda = 5$, 2, 1 and 0.5 eV). The dotted line shows the Butler-Volmer model for $\alpha = 0.5$ for comparison.

$\alpha = \frac{1}{2}$. This relationship can clearly be seen in Figure 5.2.

Clearly the value of the reorganisation energy affects the rate constants of the SMH model in a different manner to the value of the transfer coefficient within the BV model. This is highlighted in Figure 5.3 which shows simulated cyclic voltammetry for a diffusional system for varying values of α and λ in the two models.

Within the BV model varying α from $\frac{1}{2}$ results in one peak becoming taller and sharper, while the other peak becomes broader and shorter. From looking at Figure 5.3 we see that as λ decreases both peaks become shorter and broader. The implications of this difference in behaviour between the BV and SMH models will be examined in the following chapters where we shall compare both models with experimental voltammetry.

5.6 Previous work

In his seminal work, Chidsey [27] used potential step chronoamperometry to study the oxidation of ferrocene groups tethered to a gold electrode via a long alkylthiol chain. The experimental dependence of the rate constant showed marked deviation from the Butler-Volmer theory, reaching a plateau rather than continuing to increase exponentially (such as shown in Figure 5.2). The SMH model, which had been developed earlier in the same work, however, was able to reproduce this leveling off of the apparent rate constant with

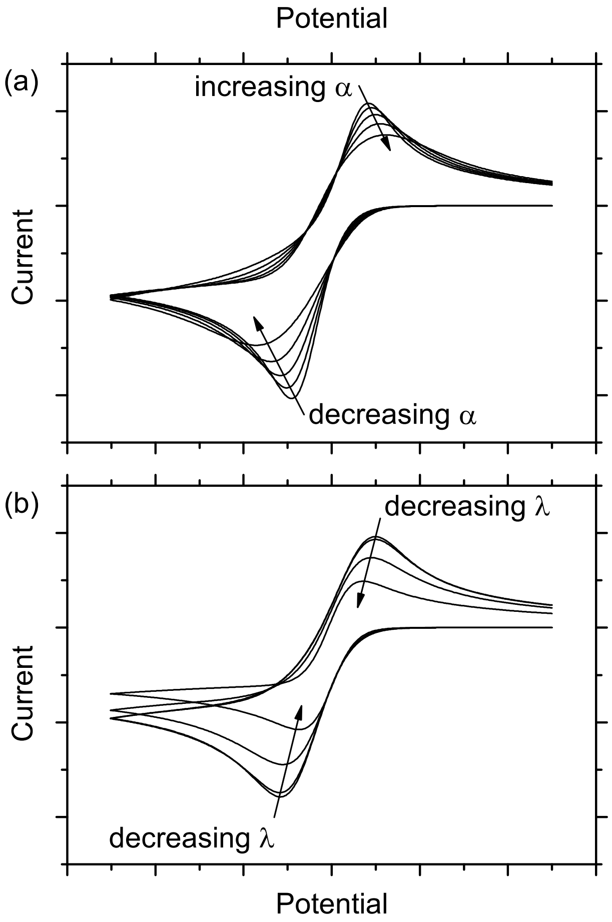

Figure 5.3: Cyclic voltammetry for a diffusional system comparing the effects of (a) α within the BV model (α = 0.3, 0.4, 0.5, 0.6 and 0.7) and (b) λ within the SMH model (λ = 10, 1, 0.1 and 0.01 eV).

striking accuracy. Accurate fitting of the experimental data was possible across a wide range of temperatures for a reorganisation energy of 0.85 eV (close to the theoretically estimated solvent reorganisation of 0.94 eV).

The excellent agreement between theory and experiment for this system justified the approximations used in the derivation above. The symmetry of the data indicated that the forward and back reactions had equal (or at least very similar) reorganisation energies and the density of states in the electrode is approximately independent of potential or the limiting rate constants at high positive and negative overpotentials would differ.

Finklea and Hanshew [32] undertook similar experiments using a ruthenium redox centre tethered to a gold electrode. The Butler-Volmer model was again found to overestimate the rate constants at large overpotential, with the experimental values tending towards a limiting value, while the SMH model fitted closely across the whole potential range with $\lambda = 0.6\,\mathrm{eV}$. Furthermore, through varying the length of the thiol chains they were able to measure the dependence of k_0 on distance from the electrode. The data was found to obey an exponential dependence on distance with the rate constant decaying by a factor of 1.06 ± 0.04 per CH_2 group which is consistent with a through-bond, rather than a through-space, tunneling mechanism.

Despite several groups reporting experimental verification of the SMH model for surface-bound redox couples [27, 32–38], there is very little literature regarding the theory as it pertains to solution-phase redox systems [39]. Researchers have preferred to continue using the BV kinetic model due to the vast body of literature which report values for k_0 and α, not least due to the relative simplicity of the theory and its implementation into computer based modeling.

Feldberg [31] has undertaken a theoretical examination of the expected differences between the BV and SMH kinetic formalisms for diffusional steady-state voltammetry at a microdisc electrode. He simulated voltammetry using the SMH model which he then proceeded to fit using the BV model in order to highlight the dangers of using an inappropriate kinetic model in the analysis of experimental data. As an illustrative example; using a moderate value of reorganisation energy (approximately 1 eV) he found that in order to obtain an equivalent voltammogram using the BV model the values of k_0 for the two formalisms could differ by a factor of 2 for a quasi-reversible system, or by as much as a factor of 200 for an extremely irreversible system. A possible weakness of his work is its assumption that the symmetric Marcus-Hush model is inherently 'correct' – a critical evaluation of this model is undertaken in the following chapters.

5.7 Conclusions

We have introduced Marcus theory as an alternative to the Butler-Volmer model for the parameterisation of electrode kinetics which may allow greater physical insight. We have then developed the so-called symmetric Marcus-Hush model for application to heterogeneous electron transfer at metallic electrodes.

Some of the experimental justifications of Marcus theory have been presented, as well as a brief overview of some of the previous work which has been undertaken in the field, the vast majority of which pertains to the analysis of surface-bound redox couples.

In the following chapters we undertake a critical examination of the theory outlined here by comparison of simulation with experimental voltammetry for several different redox systems under varied experimental conditions.

Bibliography

[1] M. C. Henstridge, E. Laborda, N. V. Rees and R. G. Compton, *Electrochim. Acta* (In press).

[2] R. A. Marcus and N. Sutin, *Biochim. Biophys. Acta* **811** (1985) 265–322.

[3] A. J. Bard and L. R. Faulkner, *Electrochemical Methods: fundamentals and applications* (Wiley, 2001), 2nd edition.

[4] R. A. Marcus, *J. Chem. Phys.* **24** (1956) 979–989.

[5] R. A. Marcus, *J. Chem. Phys.* **24** (1956) 966–978.

[6] R. A. Marcus, *J. Chem. Phys.* **26** (1957) 867–871.

[7] R. A. Marcus, *J. Chem. Phys.* **26** (1957) 872–877.

[8] N. S. Hush, *J. Chem. Phys.* **28** (1958) 962–972.

[9] N. S. Hush, *J. Electroanal. Chem.* **470** (1999) 170–195.

[10] S. Fletcher, *J. Solid State Electrochem.* **14** (2010) 705–739.

[11] J. E. B. Randles, *Trans. Faraday Soc.* **48** (1952) 828–832.

[12] J. R. Miller, L. T. Calcaterra and G. L. Closs, *J. Am. Chem. Soc.* **106** (1984) 3047–3049.

[13] J. M. Savéant and D. Tessier, *J. Electroanal. Chem.* **65** (1975) 57–66.

[14] J. M. Savéant and D. Tessier, *J. Phys. Chem.* **81** (1977) 2192–2197.

[15] J. M. Savéant and D. Tessier, *Faraday Discuss. Chem. Soc.* **74** (1982) 57–72.

[16] D. A. Corrigan and D. H. Evans, *J. Electroanal. Chem.* **106** (1980) 287–304.

[17] H. Fernández and M. A. Zón, *J. Electroanal. Chem.* **283** (1990) 251–270.

[18] A. S. Baranski, K. Winkler and W. R. Fawcett, *J. Electroanal. Chem.* **313** (1991) 367–375.

[19] H. Fernández and M. A. Zón, *J. Electroanal. Chem.* **332** (1992) 237–255.

[20] M. B. Moressi, M. A. Zón and H. Fernández, *Electrochim. Acta* **45** (2000) 1669–1682.

[21] A. D. Clegg, N. V. Rees, O. V. Klymenko, B. A. Coles and R. G. Compton, *J. Am. Chem. Soc.* **126** (2004) 6185–6192.

[22] A. D. Clegg, N. V. Rees, O. V. Klymenko, B. A. Coles and R. G. Compton, *J. Electroanal. Chem.* **580** (2005) 78–86.

[23] X. Zhang, J. Leddy and A. J. Bard, *J. Am. Chem. Soc.* **107** (1985) 3719–3721.

[24] X. Zhang, H. Yang and A. J. Bard, *J. Am. Chem. Soc.* **109** (1987) 1916–1920.

[25] A. D. Clegg, N. V. Rees, O. V. Klymenko, B. A. Coles and R. G. Compton, *ChemPhysChem* **5** (2004) 1234–1240.

[26] N. V. Rees, A. D. Clegg, O. V. Klymenko, B. A. Coles and R. G. Compton, *J. Phys. Chem. B* **108** (2004) 13047–13051.

[27] C. E. D. Chidsey, *Science* **251** (1991) 919–922.

[28] W. J. Royea, A. M. Fajardo and N. S. Lewis, *J. Phys. Chem. B* **101** (1997) 11152–11159.

[29] W. J. Royea, T. W. Hamann, B. S. Brunschwig and N. S. Lewis, *J. Phys. Chem. B* **110** (2006) 19433–19442.

[30] K. B. Oldham and J. C. Myland, *J. Electroanal. Chem.* **655** (2011) 65–72.

[31] S. W. Feldberg, *Anal. Chem.* **82** (2010) 5176–5183.

[32] H. O. Finklea and D. D. Hanshew, *J. Am. Chem. Soc.* **114** (1992) 3173–3181.

[33] R. J. Forster and L. R. Faulkner, *J. Am. Chem. Soc.* **116** (1994) 5444–5452.

[34] J. N. Richardson, G. K. Rowe, M. T. Carter, L. M. Tender, L. S. Curtin, S. R. Peck and R. W. Murray, *Electrochim. Acta* **40** (1995) 1331–1338.

[35] J. N. Richardson, S. R. Peck, L. S. Curtin, L. M. Tender, R. H. Terrill, M. T. Carter, R. W. Murray, G. K. Rowe and S. E. Creager, *J. Phys. Chem.* **99** (1995) 766–772.

[36] J. Hirst and F. A. Armstrong, *Anal. Chem.* **70** (1998) 5062–5071.

[37] H. O. Finklea, K. Yoon, E. Chamberlain, J. Allen and R. Haddox, *J. Phys. Chem. B* **105** (2001) 3088–3092.

[38] R. M. Haddox and H. O. Finklea, *J. Phys. Chem. B* **108** (2004) 1694–1700.

[39] J. N. Richardson, J. Harvey and R. W. Murray, *J. Phys. Chem.* **98** (1994) 13396–13402.

Chapter 6

Electron transfer to and from species bound at a non-uniform electrode surface

Two simple models of electrode surface inhomogeneity based on symmetric Marcus-Hush theory are considered in this chapter; a distribution in formal potentials and a distribution in electron tunneling distances. Cyclic voltammetry simulated using these two models of inhomogeneity is compared with that simulated for a flat, uniform and homogeneous electrode surface. Both models of surface inhomogeneity yield broadened peaks with decreased peak-currents relative to the homogeneous surface.

An edge-plane pyrolytic graphite electrode is then covalently modified with ferrocene via 'click' chemistry and the resulting voltammetry compared with each of the three previously considered models. The distribution of formal potentials is seen to fit the experimental data most closely.

This work has been published in *Chemical Physics Letters* [1]. The experiments were performed by R. Gusmão.

6.1 Introduction

Carbon based electrodes find regular use in electrochemical experiments, in part due to their relative ease of modification and low associated costs. Application of such electrode materials range from point-of-use electroanalysis through to industrial scale synthesis [2]. Carbon is available in a variety of forms, of these graphite is of great significance not least for its use as an enzymic support [3] but also due to the fact that the electrochemical response of carbon nanotubes are often viewed as being analogous [4]. The graphitic surface is heterogeneous in nature exhibiting both edge and basal plane sites, where it is generally viewed that the rate of electron transfer is substantially lower at the basal plane sites [5]. Consequently, knowledge of how the surface structure influences the observed voltammetric response is imperative for the development of more sophisticated graphite based electrochemical systems.

Following the seminal work of Chidsey [6], symmetric Marcus-Hush theory has been widely applied in describing the redox activity of species adsorbed on an electrode surface [7–14]. While this theory has been very successful in modeling many systems, mainly on Au electrodes, it fails to adequately describe a number of systems which exhibit non-ideal broadening of voltammetric peaks [15–20], caused by a distribution of rates at which the adsorbate is oxidised or reduced. Through assessment of how the voltammetric response for the surface bound voltammetric wave deviates from 'ideality' we are able to gain greater insight into the interfacial chemistry occurring at the electrode/solution interface.

For redox species attached to graphite electrodes, kinetic inhomogeneity may be attributed to a number of causes; roughness of the electrode surface or disorder within the adsorbate monolayer could yield a distribution of distances over which electron tunneling occurs; equally, covalent attachment of the adsorbed species at different crystal planes or to different functional groups on the electrode surface could alter the thermodynamic properties of the redox system and yield a distribution of formal potentials as studied by Albery *et al.* [21].

Rowe *et al.* [19] have studied these models of surface inhomogeneity within the context of potential step chronoamperometry and suggested that conventional analysis of such non-ideal systems could lead to erroneous determination of kinetic parameters. In the absence of a parameter controlling the extent of inhomogeneity the only variables able to affect the shape of the voltammetric wave are the rate constant and reorganisation energy. The broadened waves which are characteristic of inhomogeneous electrode surfaces are best approximated, in this situation, by a small value of reorganisation energy.

Honeychurch *et al.* have looked at other sources of voltammetric non-ideality for both reversible [22] and irreversible systems [23], including broadening caused by lateral interactions between adsorbate molecules as considered by Laviron [24]. However, in experimental work on a ferrocene-modified edge-plane pyrolytic graphite electrode we find that voltammetric broadening is unaffected by surface coverage and so varying adsorbate-adsorbate interactions cannot be the cause of any observed non-ideality. Smith and White have also considered the effects of monolayer thickness and dielectric on voltammetry [25].

Inhomogeneous, or rough, electrodes are ubiquitous in experimental electrochemistry and have been observed to show different behaviour to flat electrodes for diffusional systems. For example, rough electrodes have been shown to yield a ten-fold increase in the stripping peak intensity for some systems [26]. Rough electrodes have been modeled for diffusional systems by Menshykau *et al.* [27, 28] using the diffusion domain approximation. Work by Kant and co-workers treated the rough electrode surface as fractal [29, 30], however real electrodes are likely only approximately fractal. Another approach has been to use exact mathematical functions [31, 32], however the solutions obtained using this method are only asymptotic and do not lend themselves to experimental applications. Gaussian distributions have been used to parameterise various other models of electrode inhomogeneity, notably by Albery [21] and Murray [19] for formal potentials and tunneling distances respectively, and it is these models which we shall consider in this work.

In this chapter we describe the modeling of cyclic voltammetry for a surface-bound redox system using the 'classical' symmetric Marcus-Hush theory (as used by Chidsey) as well as considering two simple models for the kinetic inhomogeneity: a Gaussian distribution of formal potentials and a Gaussian distribution of electron tunneling distances. These theoretical results are then used to consider experimental voltammetry for a ferrocene-modified edge-plane pyrolytic graphite (Fc-EPPG) electrode, whereby we are able to demonstrate that the source of non-ideality is likely related to the presence of a distribution of formal potentials arising from the differing environments present upon the electrode.

6.2 Theory

We consider the redox reaction $\mathrm{A} + \mathrm{e} \rightleftharpoons \mathrm{B}$, in which A and B are both confined on the surface of an electrode. The current for this reaction is given by:

$$I = FA\left[-k_{\mathrm{red}}\Gamma_{\mathrm{A}} + k_{\mathrm{ox}}\Gamma_{\mathrm{B}}\right] \tag{6.1}$$

where F is the Faraday constant, A is the electrode area, Γ_i is the surface coverage of species i and k_{ox} and k_{red} are the rate constants for oxidation and reduction respectively. For this system, symmetric Marcus-Hush kinetics are assumed throughout.

The inhomogeneity of the electrode surface was modeled as a Gaussian distribution of parameter χ (either formal potential or tunneling distance) with mean μ and standard deviation σ. A total of 300 cyclic voltammograms were simulated, spread evenly across the range $\chi = \mu \pm 3\sigma$. A weighted sum was then calculated to give the total current:

$$I_{\text{total}} = \frac{\sum\limits_j w_j \, I_j}{\sum\limits_j w_j} \tag{6.2}$$

where I_j is the current of the jth simulation, given by Equation (6.1), and w_j is the weighting of the jth simulation which is given by the Gaussian function:

$$w_j = \exp\left[\frac{-(\chi_j - \mu)^2}{2\sigma^2}\right] \tag{6.3}$$

The distribution of formal potentials is thus directly implemented, however varying the tunneling distance manifests as a change in k_0 since [33, 34]:

$$k_0 \propto \exp(-\beta r_0) \tag{6.4}$$

where r_0 is the distance separating the redox centre from the electrode surface and β is the electronic coupling attenuation coefficient which takes a value of $1.59\,\text{Å}^{-1}$ water [35].

It should be noted that values of k_0 quoted in this chapter are defined at the electrode surface and are subject to Equation (6.4), thus a value of $10^6\,\text{s}^{-1}$ at the electrode surface is equal to $0.113\,\text{s}^{-1}$ at a distance of $10\,\text{Å}$ from the electrode, assuming β takes the value $1.6\,\text{Å}^{-1}$.

When simulating the homogeneous electrode, for which no distribution of parameters was considered, σ was set equal to zero. In all cases Equation (6.1) was solved numerically using the backwards implicit finite difference method.

6.3 Theoretical results

Numerical simulations were performed using the two models of inhomogeneity (Gaussian distributions of formal potentials and tunneling distances) and the voltammetry compared with that simulated for a uniform homogeneous electrode surface. As $\sigma(\chi)$ was increased from 0, both inhomogeneous models yielded voltammetric waves which are noticeably broadened with correspondingly decreased peak currents.

The shape of the broadened voltammetric wave, however, differs between the two models. Figure 6.1 shows a series of voltammograms simulated using a distribution of formal potentials with $\sigma(E^{\ominus})$ increasing from 0 mV (equivalent to the homogeneous model) to 100 mV. The broadening is seen to occur symmetrically about the peak potential, consistent with the symmetrical nature of the Gaussian distribution of formal potentials, such that the peak potential remains the same for all values of $\sigma(E^{\ominus})$.

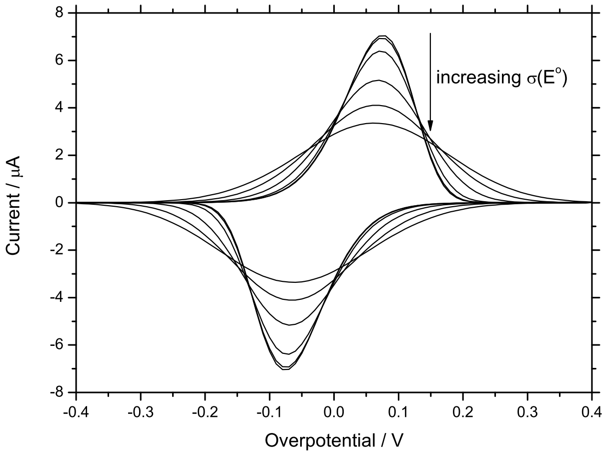

Figure 6.1: Typical voltammetry simulated using a Gaussian distribution of formal potentials, $\sigma(E^{\ominus}) = 0, 10, 25, 50, 75, 100\,\mathrm{mV}$. The voltammetry is simulated a scan rate of $100\,\mathrm{mV\,s^{-1}}$ for a redox couple with $k_0 = 4.4 \times 10^6\,\mathrm{s^{-1}}$, $\lambda = 1.0\,\mathrm{eV}$, $r_0 = 10\,\text{Å}$, and $\beta = 1.5\,\text{Å}^{-1}$.

This is in contrast to voltammetry simulated using the distribution of tunneling distances. Figure 6.2 shows simulations for a range of values of $\sigma(r_0)$ from 0 Å (equivalent to the homogeneous model) up to 3 Å. As with the distribution of formal potentials the peak current is seen to decrease with increasing $\sigma(r_0)$, however in this case the peak itself remains relatively sharp for all values of $\sigma(r_0)$. Due to the exponential dependence of rate constant on tunneling distance (Equation (6.4)), the distribution of k_0 values is weighted towards very slow kinetics. Thus increasing $\sigma(r_0)$ results an increasingly extended 'tail' at high overpotential, with appreciable Faradaic current continuing some tens or even hundreds of millivolts beyond the peak potential. A further consequence of this asymmetric distribution of rate constants is that the peak potential shifts to lower overpotential with increasing $\sigma(r_0)$, resulting in voltammetry which appears more reversible.

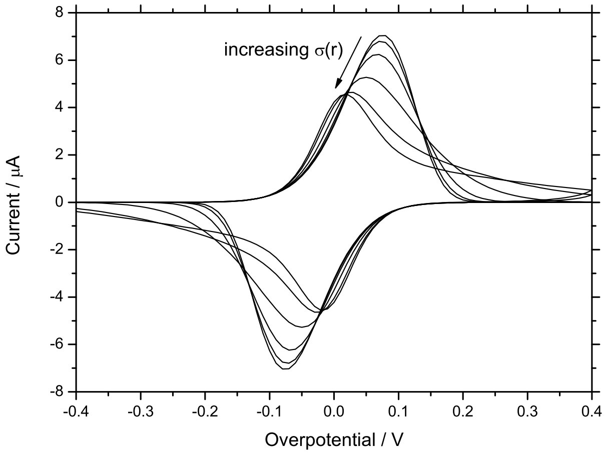

Figure 6.2: Typical voltammetry simulated using a Gaussian distribution of tunneling distances, $\sigma(r_0) = 0, 0.25, 0.5, 1, 2, 3\,\text{Å}$. The voltammetry was simulated a scan rate of $100\,\text{mV}\,\text{s}^{-1}$ for a redox couple with $k_0 = 4.4 \times 10^6\,\text{s}^{-1}$, $\lambda = 1.0\,\text{eV}$, $r_0 = 10\,\text{Å}$, and $\beta = 1.5\,\text{Å}^{-1}$.

These qualitative differences in wave broadening resulting from the two different models may therefore be used as a diagnostic when deciding which model is most appropriate for simulating a particular experimental system.

6.4 Experimental procedure

6.4.1 Reagents and Equipment

All chemicals were purchased from Sigma-Aldrich (St. Louis, MO) at the highest grade available and used directly without any further purification. All solutions were prepared with deionized water of resistivity not less than $18.2\,\text{M}\Omega\,\text{cm}$ at $298\,\text{K}$ (Millipore, Billerica, MA). All voltammetric measurements were recorded using a μ-Autolab type III computer controlled potentiostat (EcoChemie, Utrecht, Netherlands). A standard three electrode configuration was used throughout, consisting of an edge-plane pyrolytic graphite (EPPG, area 0.196 cm^2) working electrode, a platinum wire and a Ag/AgCl/Sat. KCl electrode acting as the counter and the reference electrodes, respectively. EPPG electrodes were polished successively by 1 and 0.3 µm alumina slurry on a cloth polishing pad and then washed in water under sonication.

6.4.2 Electrode modification

The synthesis of 4-azidobenzene diazonium tetrafluoroborate was carried out according to a literature procedure [36]. A cold solution of $NaNO_2$ (45 mg, 0.65 mmol) in Milli-Q water (0.25 ml) was added slowly to a cold solution (over an ice bath) of 4-azidoaniline hydrochloride (100 mg, 0.59 mmol) in 1 M HCl (1 ml). The mixture was left to react at 4 °C for 1 h, and then 0.6 ml of a saturated aqueous solution of $NaBF_4$ was added. The precipitated brown diazonium tetrafluoroborate was filtered and washed with cold ether, then dried in a desiccator and stored in the freezer.

Surface derivatisation of the EPPG electrode was carried out at 4 °C in a deaerated solution of 0.1 M HCl (10 ml) containing 1 mM 4-azidobenzene diazonium tetrafluoroborate. The reductive electrodeposition of the aryl diazonium salt was achieved amperometrically by stepping the potential at a sufficiently cathodic value (working electrode potential was set for 1 min at -0.80 V). After functionalisation, the electrode was thoroughly rinsed with cold water.

The ferrocene probes were then coupled to the surface diazonium groups by copper (I)-catalyzed azide-alkyne cycloaddition according to a literature procedure [36]. Arylazide modified electrodes were immersed in a 5 ml Milli-Q water solution containing $CuSO_4$ (10 mM), L-ascorbic acid (10 mM) and ethynylferrocene (100 µM) over an ice bath. The click reaction was complete after 60 min. The Fc-EPPG electrode was then rinsed with cold Milli-Q water and ethanol to ensure removal of any physisorbed species.

6.4.3 Electrode characterisation

Cyclic voltammetry of the Fc-EPPG electrode was systematically recorded in 0.1 M KPF_6 at 20 °C over a wide range of scan rates (10 – 800 mV s^{-1}), as shown in Figure 6.3. A plot of peak current against scan rate was found to be linear (Figure 6.4), indicating that the redox active species was, in fact, adsorbed on the electrode surface with the surface coverage calculated to be $1.0 \times 10^{-9}\,\mathrm{mol\,cm^{-2}}$, equivalent to $16.6\,\mathring{A}^2$ per molecule.

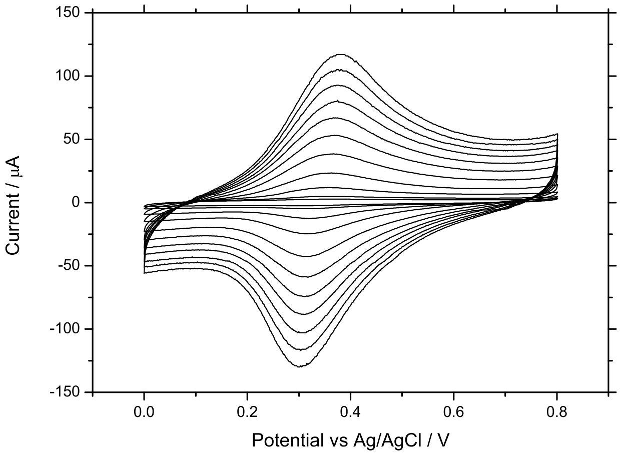

Figure 6.3: Experimental voltammetry of the ferrocene-modified electrode recorded at scan rates between $10\,\mathrm{mV\,s^{-1}}$ and $800\,\mathrm{mV\,s^{-1}}$.

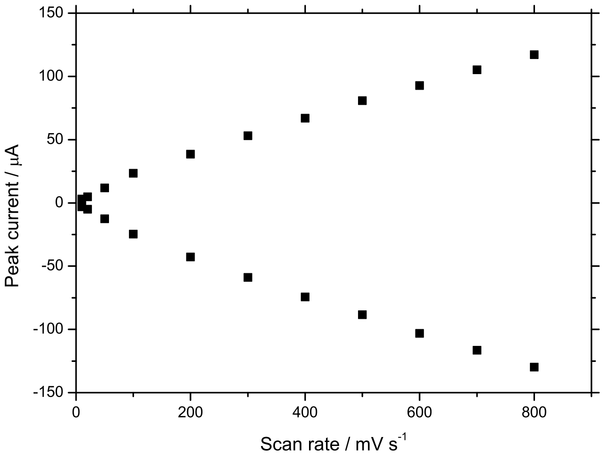

Figure 6.4: Scan rate dependence of the peak current for the ferrocene-modified electrode.

Due to the inherent roughness of the EPPG surface, the actual surface area of the electrode will be larger than the geometric surface area used to calculate surface coverage [37]. This value of surface coverage therefore corresponds to sub-monolayer coverage for a molecule the size of ferrocene.

With a high surface coverage the possibility of inter-adsorbate interaction needs to be considered. Laviron considered the voltammetry of adsorbed species within the framework of the Frumkin isotherm [24] and found that adsorbate-adsorbate interaction can cause changes in peak width. However, comparison of voltammetry recorded at this high coverage with voltammetry obtained using a lower coverage ($6.0 \times 10^{-10}\,\mathrm{mol\,cm^{-2}}$) shows that the full width half maximum (FWHM) is found to be almost the same for both coverages across the whole range of scan rates. Since an increase in surface coverage should lead to increased adsorbate-adsorbate interaction and therefore a change in FWHM, we shall assume that inter-adsorbate interactions are weak in this case and that experimental voltammetric broadening can likely be attributed to surface inhomogeneity alone.

6.4.4 Potential staircase effects

Cyclic voltammetry was performed using a potential staircase, while simulations were carried out assuming an analog potential ramp. The accuracy of this approximation was checked via comparison with a program simulating a series of potential steps, with each step being described by the analytical solution for a surface-bound chronoamperogram. The error was found to be less than 5 % over the whole range of scan rates used.

6.5 Experimental results

These experimental results were, after baseline subtraction, fitted using each of the two inhomogeneous models, as well as the homogeneous model. The best-fit parameters are given in Table 6.1.

The experimental voltammetry is observed to be highly broadened when compared with simulations of homogeneous Marcus-Hush theory shown in Figure 6.5, even when using an extremely small reorganisation energy of 10^{-4} eV as has been previously reported for an inhomogeneous electrode surface [15–20], with the simulated peak current being much too large.

When compared with the simulations incorporating surface inhomogeneity, however, a much closer fit is achieved. The distribution of tunneling distances achieves fairly good agreement with the experimental peak current and potential (Figure 6.6(b)), however the overall waveshape is qualitatively different; with the current initially rising too sharply, then decaying too slowly. In contrast the distribution of formal potentials has enabled excellent agreement between theory and experiment (Figure 6.6(a)), matching peak cur-

	Homogeneous	$E^{\ominus}$ distribution	r_0 distribution
$E^{\ominus}$ / V	0.33	0.34	0.34
k_0 / s^{-1}	5.3×10^6	7.1×10^6	4.0×10^6
λ / eV	10^{-4}	0.85	0.85
$\sigma(E^{\ominus})$ / mV	–	60	–
$\sigma(r_0)$ / Å	–	–	3

Table 6.1: Best-fit parameters for each model. Note that these values of k_0 are defined at the electrode surface and are subject to Equation (6.4), in all cases $r_0 = 10\,\text{Å}$ and $\beta = 1.6\,\text{Å}^{-1}$.

rent, peak potential and achieving a very close fit for the overall shape of the voltammetric wave. The qualitative differences in fit between the two models strongly suggest that a distribution of formal potentials is the most likely contributing factor to the observed inhomogeneity in this system.

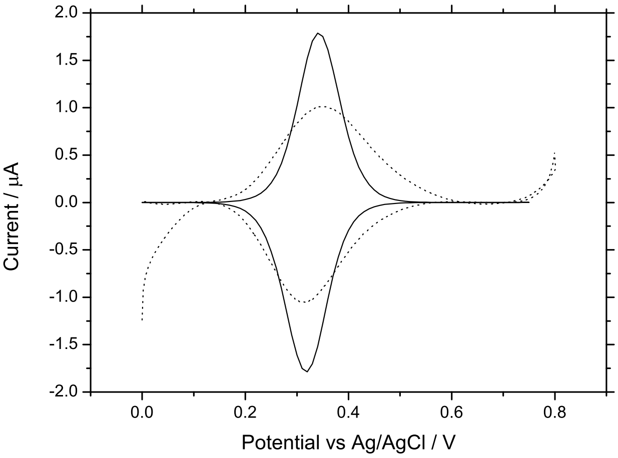

Figure 6.5: Comparison of baseline-subtracted experimental voltammetry (dotted line) with the homogeneous model (solid line), scan rate is $10\,\mathrm{mV\,s^{-1}}$. Parameters are as given in Table 6.1.

The Gaussian distribution of formal potentials also provides a better fit of peak potentials across the whole range of scan rates used. As can be seen in Figure 6.7, despite fitting very well at low scan rate, the distribution of tunneling distances generally predicts a larger peak-peak separation than is observed experimentally, whereas the distribution of formal potentials fits fairly well across the whole range. Figure 6.7 demonstrates that

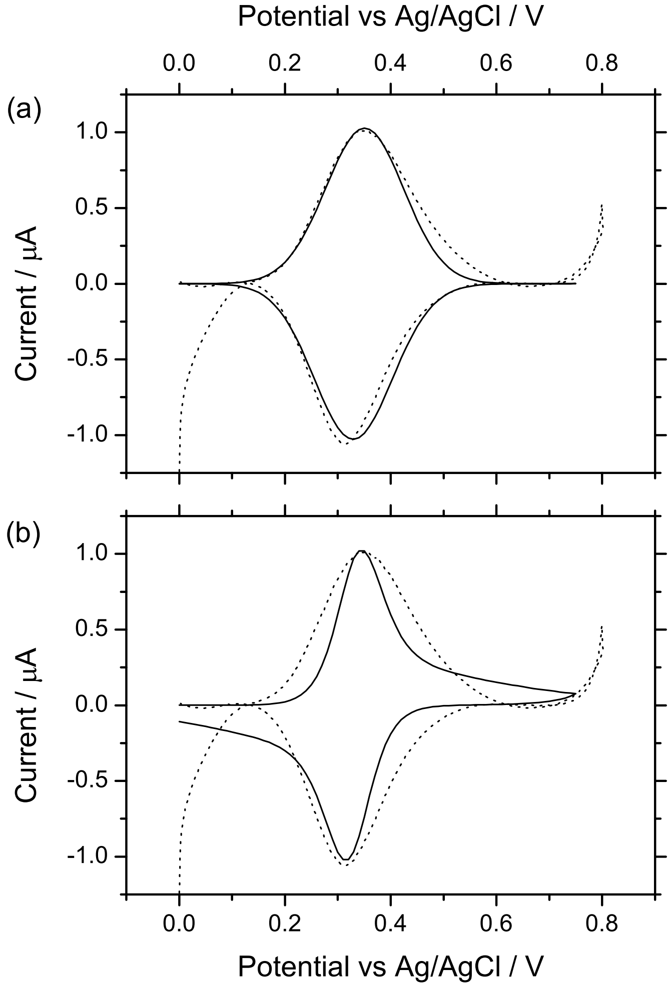

Figure 6.6: Comparison of baseline-subtracted experimental voltammetry (dotted line) with a heterogeneous model (solid line), scan rate is $10\,\mathrm{mV\,s^{-1}}$. Simulations were performed using (a) a distribution of formal potentials and (b) a distribution of tunneling distances. Parameters are as given in Table 6.1.

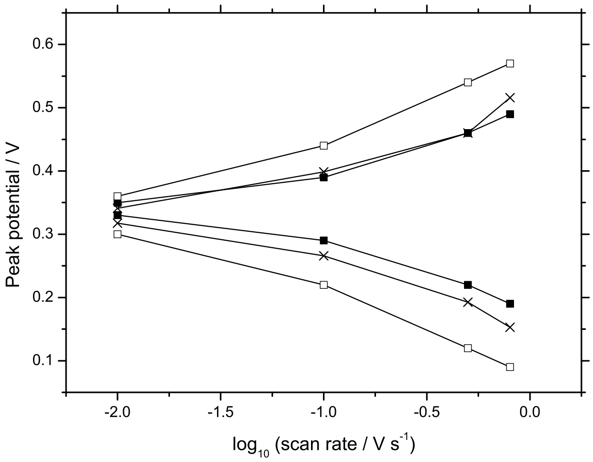

Figure 6.7: Plot of peak potential against log scan rate for both oxidative and reductive peaks. Experiment (crosses), distribution of formal potentials (black squares), distribution of tunneling distances (white squares).

even at low scan rates there is a non-zero peak separation. While this may be caused by the presence of non-uniform multilayers [25], hysteresis has also been explained in terms of a square scheme in which different paths for oxidation and reduction exist [38] as well as an 'N-shaped' free energy curve [39].

6.6 Discussion

While the use of the symmetric Marcus-Hush model theory assumes a perfectly metallic electrode [34] we tentatively assume that it might be applied to EPPG due to its high density of states [40–43]. This assumption has been corroborated by recent work by Nissim *et al.* who measured the heterogeneous rate constants for the oxidation of a series of quinone species at both a gold electrode and a graphite electrode, treating both as metals, and finding the ratio of rate constants at the two electrodes is proportional to the difference in the density of states in the two materials [44].

Additionally, the density of states in the electrode is assumed to be approximately constant across the range of potentials used, as is the electronic coupling matrix (see Chapter 5). Thus, for a given redox couple at a given distance from the electrode surface, k_0 is assumed constant. While these assumptions make the application of Marcus theory to reactions at electrodes a more tractable problem, it should be noted that the model remains an approximation.

The value of λ used here in the simulations of both models of inhomogeneity is in excellent agreement with that reported by Chidsey for thiol-tethered ferrocene on a gold electrode [6], whereas the best fit achieved with the homogeneous model used a value which is several orders of magnitude smaller. This is in alignment with the conclusion of Rowe *et al.* that ignoring the effects of surface inhomogeneity leads to the extraction of erroneous values of kinetic parameters [19].

The successful fit of the voltammetric data via the use of a distribution of formal potentials gives possible insight into the cause of the non-ideality. In light of the surface structure of the graphite material it may be concluded that the varying solvation and local ionic atmosphere may be contributing to the observed variation in formal potentials. Further the bonding of the ferrocene group to different sites or crystal planes on the electrode surface may also lead to such thermodynamic shifts.

It should be noted, that despite the superior fit achieved by the inhomogeneous models, in order to achieve voltammetric broadening to such an extent it was necessary to use a relatively large value of σ. In particular for the distribution of formal potentials, the best fit was achieved using a value of $\sigma(E^{\ominus})$ equal to 60 mV, meaning that over the whole distribution $(\mu \pm 3\sigma)$ $\Delta G^{\ominus}$ would vary by $35\,\mathrm{kJ\,mol^{-1}}$.

However, the use of a Gaussian distribution to approximate surface inhomogeneity is only a rudimentary model. It is also possible that more than one parameter could show small variations simultaneously, rather than only one varying in isolation. It is possible that a more sophisticated model for surface inhomogeneity could yield similar voltammetric broadening with smaller variations in parameter values, but considering the simplicity of the model used the observed agreement with experiment is excellent.

6.7 Conclusion

Simulations using two different models for electrode surface inhomogeneity have been compared with both simulations for a homogeneous surface and with experimental results. The voltammetric broadening reported in the literature is reproduced qualitatively by both a Gaussian distribution of formal potentials and a Gaussian distribution of electron tunneling distances, but not by the homogeneous model. Comparison with experimental voltammetry obtained from a Fc-EPPG electrode revealed that a distribution in formal potentials is found to achieve by far the best fit.

Bibliography

[1] M. C. Henstridge, C. Batchelor-McAuley, R. Gusmao and R. G. Compton, *Chem. Phys. Lett.* **517** (2011) 108–112.

[2] R. L. McCreery, *Chem. Rev.* **108** (2008) 2646–2687.

[3] C. F. Blanford and F. A. Armstrong, *J. Solid State Electrochem.* **10** (2006) 826–832.

[4] I. Dumitrescu, P. R. Unwin, N. R. Wilson and J. V. Macpherson, *Anal. Chem.* **80** (2008) 3598–3605.

[5] C. Neumann, C. Batchelor-Mcauley, C. Downing and R. Compton, *Chem. Eur. J.* **17** (2011) 7320–7326.

[6] C. E. D. Chidsey, *Science* **251** (1991) 919–922.

[7] J. F. Smalley, M. D. Newton and S. W. Feldberg, *J. Electroanal. Chem.* **589** (2006) 1–6.

[8] H. O. Finklea, L. Liu, M. S. Ravenscroft and S. Punturi, *J. Phys. Chem.* **100** (1996) 18852–18858.

[9] Q. Chi, J. Zhang, J. E. T. Andersen and J. Ulstrup, *J. Phys. Chem. B* **105** (2001) 4669–4679.

[10] J. Yan, S. Dong, J. Li and W. Chen, *J. Electrochem. Soc.* **144** (1997) 3858–3865.

[11] J. Hirst and F. A. Armstrong, *Anal. Chem.* **70** (1998) 5062–5071.

[12] H. O. Finklea and D. D. Hanshew, *J. Am. Chem. Soc.* **114** (1992) 3173–3181.

[13] M. S. Ravenscroft and H. O. Finklea, *J. Phys. Chem.* **98** (1994) 3843–3850.

[14] P. Fristrup, M. Grubb, J. Zhang, H. E. M. Christensen, A. M. Hansen and J. Ulstrup, *J. Electroanal. Chem.* **511** (2001) 128–133.

[15] J. N. Richardson, G. K. Rowe, M. T. Carter, L. M. Tender, L. S. Curtin, S. R. Peck and R. W. Murray, *Electrochim. Acta* **40** (1995) 1331–1338.

[16] J. N. Richardson, S. R. Peck, L. S. Curtin, L. M. Tender, R. H. Terrill, M. T. Carter, R. W. Murray, G. K. Rowe and S. E. Creager, *J. Phys. Chem.* **99** (1995) 766–772.

[17] R. S. Ingram and R. W. Murray, *J. Chem. Soc. Faraday Trans.* **92** (1996) 3941–3946.

[18] L. Tender, M. T. Carter and R. W. Murray, *Anal. Chem.* **66** (1994) 3173–3181.

[19] G. K. Rowe, M. T. Carter, J. N. Richardson and R. W. Murray, *Langmuir* **11** (1995) 1797–1806.

[20] A. L. Eckermann, J. A. Shaw and T. J. Meade, *Langmuir* **26** (2010) 2904–2913.

[21] W. J. Albery, M. G. Boutelle, P. J. Colby and A. R. Hillman, *J. Electroanal. Chem.* **133** (1982) 135–145.

[22] M. J. Honeychurch and G. A. Rechnitz, *Electroanalysis* **10** (1998) 285–293.

[23] M. J. Honeychurch and G. A. Rechnitz, *Electroanalysis* **10** (1998) 453–457.

[24] E. Laviron, *J.Electroanal. Chem.* **105** (1979) 25–34.

[25] C. P. Smith and H. S. White, *Anal. Chem.* **64** (1992) 2398–2405.

[26] L. Fojt and S. Hasoň, *J. Electroanal. Chem.* **586** (2006) 136–143.

[27] D. Menshykau, I. Streeter and R. G. Compton, *J. Phys. Chem. C* **112** (2008) 14428–14438.

[28] D. Menshykau and R. G. Compton, *J. Phys. Chem. C* **113** (2009) 15602–15620.

[29] R. Kant and S. Rangarajan, *J. Electroanal. Chem.* **368** (1994) 1–21.

[30] S. K. Jha, A. Sangal and R. Kant, *J. Electroanal. Chem.* **615** (2008) 180–190.

[31] T. R. Nolen and P. S. Fedkiw, *J. Electroanal. Chem.* **258** (1989) 265–280.

[32] D. S. Louch and M. D. Pritzker, *J. Electroanal. Chem.* **319** (1991) 33–53.

[33] W. J. Royea, A. M. Fajardo and N. S. Lewis, *J. Phys. Chem. B* **101** (1997) 11152–11159.

[34] W. J. Royea, T. W. Hamann, B. S. Brunschwig and N. S. Lewis, *J. Phys. Chem. B* **110** (2006) 19433–19442.

[35] P. P. Edwards, H. B. Gray, M. T. J. Lodge and R. J. P. Williams, *Angew. Chem. Int. Ed.* **47** (2008) 6758–6765.

[36] D. Evrard, F. Lambert, C. Policar, V. Balland and B. Limoges, *Chem. Eur. J.* **14** (2008) 9286–9291.

[37] J. P. Randin and E. Yeager, *J. Electroanal. Chem.* **58** (1975) 313–322.

[38] C. Amatore, E. Maisonhaute, B. Schöllhorn and J. Wadhawan, *ChemPhysChem* **8** (2007) 1321–1329.

[39] S. W. Feldberg and I. Rubinstein, *J. Electroanal. Chem.* **240** (1988) 1–15.

[40] C. A. Coulson and R. Taylor, *Proc. Phys. Soc.* **65A** (1952) 815–825.

[41] A. R. Ubbelohde, *Proc. R. Soc. Lond. A* **327** (1972) 289–303.

[42] L. Edman, B. Sundqvist, E. McRae and E. Litvin-Staszewska, *Phys. Rev. B* **57** (1998) 6227–6230.

[43] D. A. Fischer, R. M. Wentzcovitch, R. G. Carr, A. Continenza and A. J. Freeman, *Phys. Rev. B* **44** (1991) 1427–1429.

[44] R. Nissim, C. Batchelor-McAuley, M. C. Henstridge and R. G. Compton, *Chem. Commun.* **48** (2012) 3294–3296.

Chapter 7

Evaluation of the symmetric Marcus-Hush model at a mercury microhemisphere electrode

This chapter presents a comparative experimental evaluation of the Butler-Volmer and symmetric Marcus-Hush models using cyclic voltammetry at a microelectrode. Numerical simulations are used to fit experimental voltammetry for the one electron reductions of europium (III) and 2-methyl-2-nitropropane at a mercury microhemisphere electrode over a wide range of voltage scan rates. For both systems the symmetric Marcus-Hush model proves less able to accurately fit the experimental voltammetry than the Butler-Volmer model.

This work has been published in the *Chemical Physics Letters* [1]. The experiments were performed by Y. Wang and J. G. Limon-Petersen.

7.1 Introduction

This chapter reports an experimental comparison of the symmetric Marcus-Hush and Butler-Volmer kinetic formalisms using cyclic voltammetry, which is by far the most popular voltammetric method employed by both electrochemists and non-specialists. We study the one electron reduction of 2-methyl-2-nitropropane (MeNP) in acetonitrile, as well as the one electron reduction of europium (III) chloride in aqueous solution, both at a mercury microhemisphere electrode. These systems were chosen due to their irreversible kinetics and literature α values which deviate from $\frac{1}{2}$ [2, 3], such systems are predicted to produce the most marked differences in the two kinetic models [4]. Experimental voltammetry was fitted using numerical simulations for both the BV and SMH models. In particular we focus on fitting the cyclic voltammetric waveshape in its entirety to identify any differences between the two kinetic models. We do not necessarily seek curved Tafel plots [5] and no a priori assumptions are made, in contrast with earlier work [6] which extracts effective rate constants as a function of potential which are not inconsistent with Marcus theory.

The enhanced mass transport properties of microelectrodes (as opposed to macroelectrodes) make them ideal for use in kinetic investigations such as this [7]. Specifically, the use of a mercury microhemisphere electrode made it possible to verify, via simulation using programs developed previously [8], that all experimental solutions contained sufficient supporting electrolyte to be considered diffusion-only systems. Owing to its one-dimensional symmetry, cyclic voltammetry at a hemispherical electrode is also much faster, more accurate and more straightforward to simulate than voltammetry at the more conventional microdisc, allowing fitting of the entire voltammetric wave. This geometry also permits our study to encompass both the linear and convergent diffusion regimes.

7.2 Theory

We consider the one-electron reduction $\mathrm{A} + \mathrm{e} \rightleftharpoons \mathrm{B}$ taking place at the surface of a hemispherical electrode. We further consider the solution to contain sufficient supporting electrolyte for migration to be neglected [8], thus only diffusional mass transport need be considered. Diffusion is described by Fick's second law which, in hemispherical geometry, takes the form:

$$\frac{\partial c_i}{\partial t} = D_i \left[\frac{2}{r} \frac{\partial c_i}{\partial r} + \frac{\partial^2 c_i}{\partial r^2} \right] \tag{7.1}$$

where c_i and D_i are respectively the concentration and diffusion coefficient of species i, r is distance and t is time. In order to solve Equation (7.1) we require boundary conditions. At $t = 0$ we assume that, throughout the simulation space, species A takes its bulk value (c^*_{A}) uniformly and that species B is absent. The outer boundary of the simulation space is set to be sufficiently far from the electrode surface such that the concentrations of A and B remain at these initial values. The outer boundary is located at

$$r_{\mathrm{max}} = r_{\mathrm{e}} + 6\sqrt{D_{\mathrm{max}}\, t_{\mathrm{max}}} \tag{7.2}$$

where r_{e} is the r-coordinate of the electrode surface, D_{max} is the larger of D_{A} and D_{B} and t_{max} is the duration of the experiment.

At the surface of the electrode, we employ the a first order rate equation as the boundary condition:

$$j_{\mathrm{A},0} = -k_{\mathrm{A}} c_{\mathrm{A},0} + k_{\mathrm{B}} c_{\mathrm{B},0} \tag{7.3}$$

where $j_{\mathrm{A},0}$ is the flux of A at the electrode surface, $c_{\mathrm{A},0}$ and $c_{\mathrm{B},0}$ are the concentrations of A and B at the electrode surface and k_{A} and k_{B} are the rate constants for the consumption of A and B respectively, given by Equations (5.10) and (5.11) in Chapter 5.

Equation (7.1) is solved using the backwards implicit finite difference method on a grid of points which expands outwards from the electrode. The discretised mass transport equation (for both species A and B), along with the appropriately discretised boundary conditions, forms a pentadiagonal matrix equation which is solved using the Thomas algorithm. This process is performed programmatically on a desktop computer with simulation times of a few seconds.

7.3 Experimental Methods

A three electrode cell was used. Hemispherical mercury ultramicroelectodes were used (radius 50 µm for Eu(III) and radius 25 µm for MeNP) as the working electrode and was prepared according the procedure of Bard *et al.* [9, 10]. A platinum wire was used as a counter electrode and a silver wire was used as the pseudo-reference electrode in non-aqueous solutions, a saturated calomel electrode electrode (SCE, Radiometer, Copenhagen) was used instead in aqueous solutions. All electrochemical experiments were carried out using a PGSTAT 12 potentiostat (Autolab, Netherlands) and thermostatted via immersion in a water bath at 298 K.

Europium (III) chloride (Aldrich, 99.99 %), 2-methyl-2-nitropropane (Aldrich, 99 %), potassium chloride (Aldrich, >99 %), tetra-n-butylammonium perchlorate (TBAP, Aldrich,

>99 %) and acetonitrile (Fischer Scientific, HPLC grade) were all used as received with no further purification. Aqueous solutions were made up using water of resistivity not less than 18.2 MΩ cm at 298 K (Millipore, UK).

All solutions were thoroughly deoxygenated, for at least 30 min, with nitrogen pre-saturated with the corresponding solvent.

7.4 Results

7.4.1 Quantifying quality of fit

In order to quantify agreement between simulation and experiment, a mean scaled absolute deviation (MSAD) was calculated for each voltammogram [11], which is defined by:

$$\%\ \mathrm{MSAD} = \frac{1}{N} \sum_{N} \left| \frac{I_{\mathrm{exp}} - I_{\mathrm{sim}}}{I_{\mathrm{exp}}} \right| \times 100 \tag{7.4}$$

where I_{exp} and I_{sim} are experimental and simulated current respectively and N is the number of data points. Since the points of the simulated voltammetry are not necessarily aligned at the same potential values as those of the experimental voltammetry, spline interpolation was used to calculate I_{sim} at the potentials of the experimental points. Additionally a narrow strip of the experimental voltammetry near $I = 0$ was omitted from the MSAD calculations because dividing by a very small value of I_{exp} yields a very large value of MSAD even if $I_{\mathrm{exp}} - I_{\mathrm{sim}}$ is small.

As an illustrative example of which regions give rise to significant error, Figure 7.1 shows the percentage scaled absolute deviation (SAD) for each point of the simulated fitting of the forward sweep of the reduction of Eu^{3+} (*vide infra*).

7.4.2 The one electron reduction of Eu(III)

In order to study the system $\mathrm{Eu}^{3+} + \mathrm{e} \rightleftharpoons \mathrm{Eu}^{2+}$, cyclic voltammetry was carried out over a wide range of voltage scan rates ($10\,\mathrm{mV\,s^{-1}}$ – $1\,\mathrm{V\,s^{-1}}$) on a 1 mM aqueous solution of europium (III) chloride containing 0.4 M potassium chloride as supporting electrolyte. Prior to attempting theoretical fitting of the experimental data the diffusion coefficients of Eu^{3+} and Eu^{2+} were determined via double potential step chronoamperometry at the

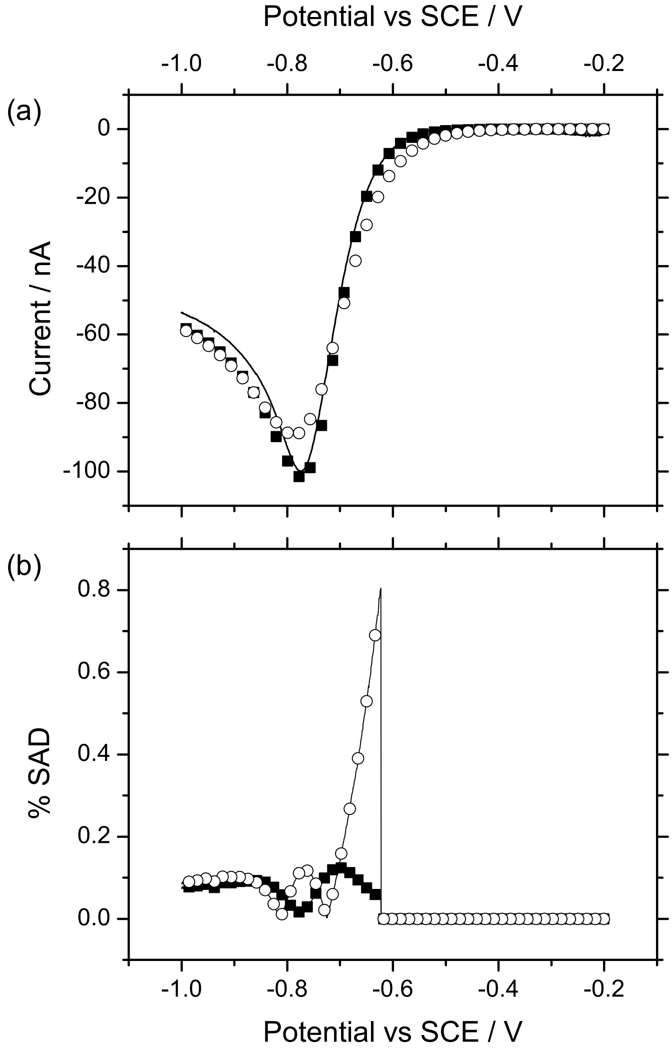

Figure 7.1: An illustrative example of the MSAD analysis showing the regions which give rise to the error. (a) The forward scan of the experimental voltammetry shown in Figure 7.2(b). (b) MSAD as a function of potential for the same voltammetry. The solid line shows the experimental data, the best-fits using the BV and SMH models are shown by black squares and white circles respectively.

Hg microhemisphere. The resulting transient was fitted for both diffusion coefficients and the concentration using a previously reported program [12] based on the Shoup & Szabo expression [7]. The diffusion coefficients for Eu^{3+} and Eu^{2+} were found to be $6.4 \times 10^{-6}\,\mathrm{cm^2\,s^{-1}}$ and $9.0 \times 10^{-6}\,\mathrm{cm^2\,s^{-1}}$ respectively at 298 K, in excellent agreement with literature values [13–15].

Although the Shoup & Szabo expression assumes infinite electrode kinetics at high overpotentials, its use was justified as follows: the Shoup & Szabo value for the diffusion coefficient was used in fitting the experimental voltammetry. Once fitting was completed the best fit values for k_0 were substituted into a second potential step program, based upon finite electrode kinetics [16], to fit the same chronoamperometric transient fitted previously. For both BV and SMH cases the diffusion coefficients were found to be effectively equal to those originally obtained from Shoup & Szabo.

Supplementary simulations were carried out to check the validity of simulating the system as "diffusion-only". These simulations used a previously reported program which solves the Nernst-Planck-Poisson system of equations and thus does not neglect migration. There was no observable difference between the diffusion-only simulations and the diffusion-migration simulations for the support ratios used in the present experiments, thus we consider the system fully supported and the diffusion-only approximation assumed valid [17].

Additional experiments were also carried out to discount possible double layer effects, so-called "Frumkin effects" [18], which could potentially have minor distorting effects on the voltammetry. Cyclic voltammetry was carried out for both 1 mM and 2 mM analyte in a range of supporting electrolyte concentrations (0.1 M – 1.0 M). When this voltammetry was fitted (using Butler-Volmer kinetics) negligible and non-systematic variation was seen for both k_0 and α. Further, within each set of experiments the formal potential was seen to be independent of scan rate and we therefore exclude possible Frumkin effects. This experimental justification is also supported by recent theoretical work [19] which considers electron transfer occurring at a range of distances from the electrode (rather than at a single distance as in Frumkin's original work [18]). This work indicates that the inclusion of this range of tunneling distances acts so as to substantially mitigate the predicted effects. Thus the experimental voltammetry was further analysed without consideration of Frumkin effects.

Experimental voltammetry for the reduction of Eu(III) is shown for two different scan rates in Figure 7.2, along with best fit simulations using both BV and SMH kinetics.

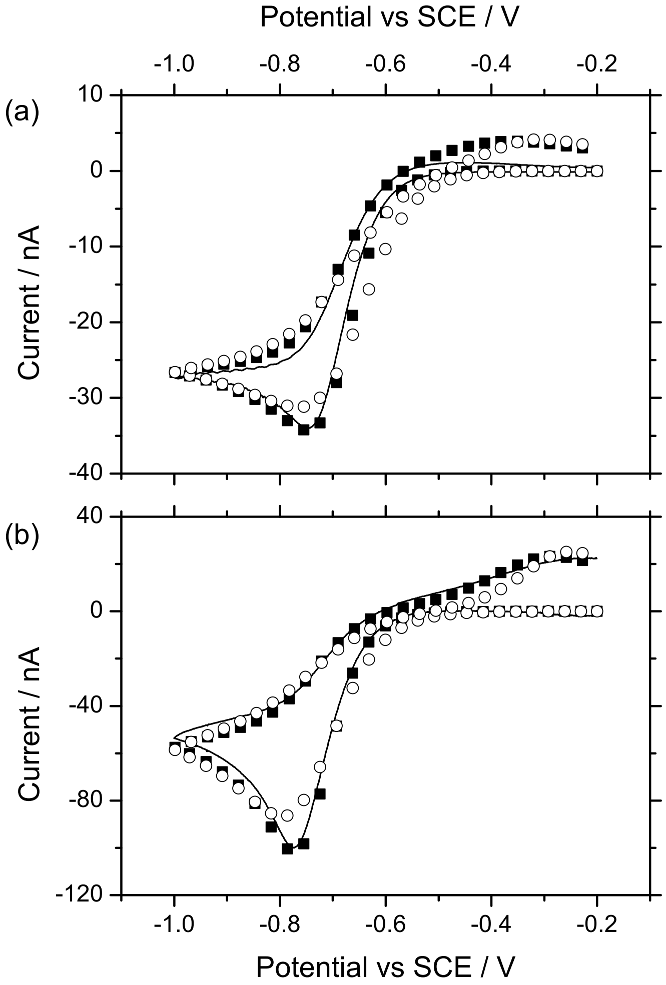

Figure 7.2: Comparison of experimental Eu(III) voltammetry (solid line) with best fit simulations using BV (black squares) and SMH (white circles) kinetics. Parameters are given in Table 7.1. (a) $50\,\mathrm{mV\,s^{-1}}$ (b) $1\,\mathrm{V\,s^{-1}}$.

For the BV model, the best fit kinetic parameters were $k_0 = 3.5 \times 10^{-4}\,\mathrm{cm\,s^{-1}}$ and $\alpha = 0.65$, which are in good agreement with values found in the literature [14]. Figure 7.2 clearly shows good agreement between simulation and experiment across a wide range of scan rates. At high scan rates a very close fit is achieved throughout the entirety of the voltammetric transient, with both the peak potential and peak current being accurately reproduced by simulations on the forward sweep, although at low scan rates the reverse peak current is overestimated by the simulations. Quantitative analysis of the fits yielded a relatively small MSAD value of 9.4 %.

The best fit achieved using SMH kinetics used $k_0 = 2.0 \times 10^{-4}\,\mathrm{cm\,s^{-1}}$ and $\lambda = 2.0\,\mathrm{eV}$. This value of λ is equal to a value calculated using the Arrhenius and Marcus relations from k_0 by Elzanowska *et al.* [2]. Similar values for reorganisation energy, between 1.0 eV and 3.0 eV, have also been reported for numerous other metals [20].

Figure 7.2 shows that for both high and low scan rates the experimental data is not fitted as accurately as was the case for BV kinetics. The forward peak current is too low and the peak too broad across the whole scan rate range. The simulated voltammetry fits the back peaks more closely than the forward, but the oxidative peak current is overestimated at all scan rates. Despite the large discrepancy between simulation and experiment, it was not possible to obtain a better fit. With both reactant and product diffusion coefficients fixed via double potential step experiments and k_0 fixed to a large degree by the peak separation, λ is the only remaining parameter able to effect a change in the voltammetric waveshape. The MSAD value calculated for the SMH model was 20.3 %, more than double the value obtained for the BV simulations.

	BV	SMH
k_0 / $\mathrm{cm\,s^{-1}}$	3.5×10^{-4}	2.0×10^{-4}
α	0.65	–
λ / eV	–	2.0
$E_\mathrm{f}^{\ominus}$ / V	-0.59	-0.52
% MSAD	9.4 ± 2.3	20.3 ± 2.8

Table 7.1: Simulation parameters for the reduction of Eu(III).

7.4.3 The one electron reduction of 2-methyl-2-nitropropane

Next, we consider the system $\mathrm{MeNP} + \mathrm{e} \rightleftharpoons \mathrm{MeNP}^{\bullet-}$. Cyclic voltammetry was carried out on a 2 mM solution of 2-methyl-2-nitropropane in acetonitrile containing 0.1 M TBAP as supporting electrolyte. Again a wide range of scan rates was studied, from $10\,\mathrm{mV\,s^{-1}}$ – $10\,\mathrm{V\,s^{-1}}$, which encompassed steady-state to fully transient voltammetric responses. The diffusion coefficients of MeNP and $\mathrm{MeNP}^{\bullet-}$ were determined via fitting of double potential step chronoamperometric transients using the same procedure described above for Eu(III). The values for MeNP and $\mathrm{MeNP}^{\bullet-}$ were both found to be $2.7 \times 10^{-5}\,\mathrm{cm^2\,s^{-1}}$, in excellent agreement with literature values [21]. There was no observed systematic shift in either $E_\mathrm{f}^\ominus$ or k_0 with scan rate; thus ohmic drop was assumed to be negligible. Again, diffusion-migration simulations proved indistinguishable from diffusion-only simulations for the support ratio used in these experiments, as expected given that MeNP is uncharged.

The experimental voltammetry is shown for two different scan rates in Figure 7.3, along with best fit simulations for both BV and SMH kinetics.

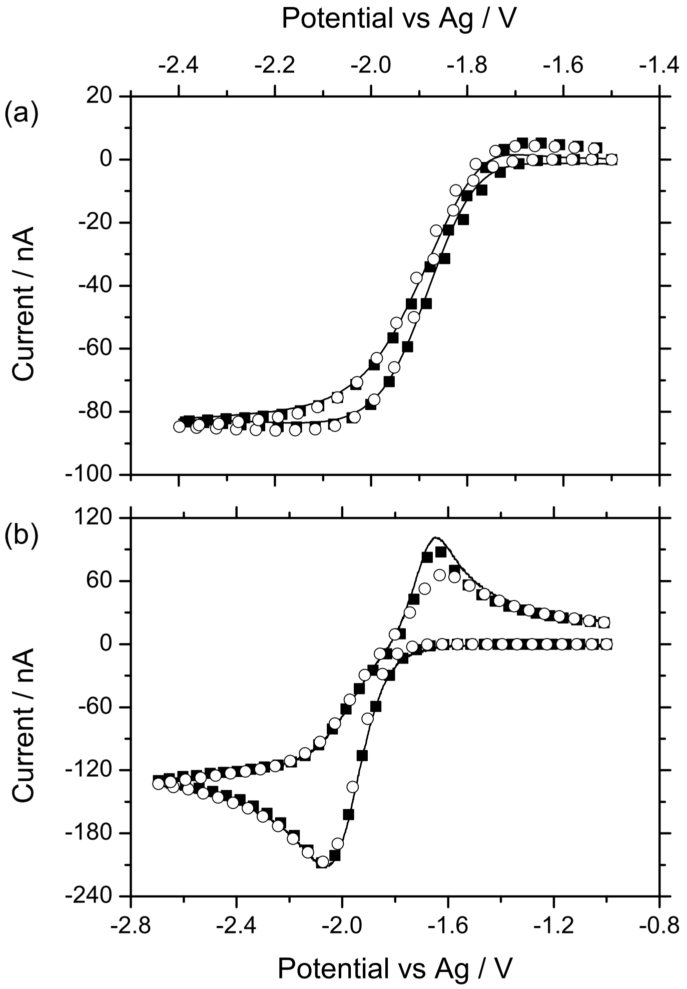

Figure 7.3: Comparison of experimental MeNP voltammetry (solid line) with best fit simulations using BV (black squares) and SMH (white circles) kinetics. Parameters are given in Table 7.2. (a) $50\,\mathrm{mV\,s^{-1}}$ (b) $5\,\mathrm{V\,s^{-1}}$.

Figure 7.3 shows that, as was the case for Eu(III), the voltammetry of MeNP was fitted very well using BV kinetics. The best fit values of k_0 and α were $3.2 \times 10^{-3}\,\mathrm{cm\,s^{-1}}$ and 0.38 respectively, both in close agreement with literature values [3, 22–24]. It can be seen that these simulations fit the experimental peak potentials and peak currents at high scan rates very closely and accurate reproduction of the steady-state current is also observed at low scan rate. This impressive agreement between simulation and experiment is reflected by the small MSAD value of 4.3 %.

The best fit achieved using the SMH model used $\lambda = 0.5\,\mathrm{eV}$ and $k_0 = 3.2 \times 10^{-3}\,\mathrm{cm\,s^{-1}}$. The simulations using these parameters yielded an MSAD value of 6.7 % which is larger than was achieved by the BV fit. Almost perfect agreement is observed between simulation and experiment at high scan rate for the forward scan, but the simulated back peak is much smaller than experiment. At lower scan rates the SMH fits are comparable to those produced by the BV model, but with a steady state current which is slightly larger than is observed experimentally.

Despite producing reasonable fitting of the experimental voltammetry, this value of λ is smaller even than the theoretical outer-sphere reorganisation energy alone, calculated to be 1.6 eV using the Equation (5.4) from Chapter 5. Furthermore, calculations using density functional theory [23] have shown that the inner-sphere reorganisation for the reduction of MeNP has a value of approximately 0.9 eV – far from negligible. Simulated voltammetry using a 'literature' value of $\lambda = 2.5\,\mathrm{eV}$, considering both inner-sphere and outer-sphere reorganisation, is shown in Figure 7.4. The increased reorganisation energy results in an overestimation of the reductive peak current whilst maintaining the underestimated oxidative peak current, leading to an increased overall MSAD value of 7.2 %. This demonstrates that simulations using SMH kinetics with physically meaningful values of reorganisation energy may, in some cases, less accurately model the real physical process!

7.5 Discussion

These two systems have also been studied using square wave voltammetry [24, 25] where a greater discrepancy in fitting was apparent between the BV and SMH models. The BV model again demonstrated excellent fitting, while the SMH model was not able to yield

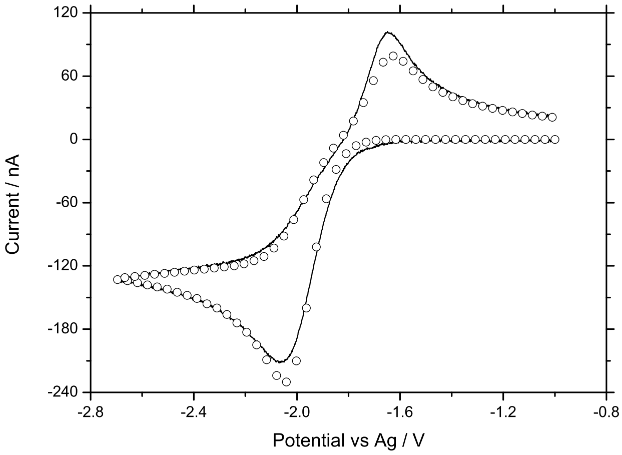

Figure 7.4: Comparison of experimental MeNP voltammetry (solid line) with simulations using SMH kinetics (white circles) using a 'literature' reorganisation energy of 2.5 eV. The scan rate is $5\,\mathrm{V\,s^{-1}}$ and all other parameters are given in Table 7.2.

	BV	SMH	
		$\lambda_{\text{best fit}}$	$\lambda_{\text{literature}}$
k_0 / $\mathrm{cm\,s^{-1}}$	3.2×10^{-3}	3.2×10^{-3}	3.2×10^{-3}
α	0.38	–	–
λ / eV	–	0.5	2.5
$E_f^\ominus$ / V	-1.825	-1.83	-1.83
% MSAD	4.3 ± 2.3	6.7 ± 3.4	7.2 ± 3.6

Table 7.2: Simulation parameters for the reduction of 2-methyl-2-nitropropane.

accurate fitting even when the reorganisation energy was used purely as a fitting parameter. Further, the reduction of cyclooctatetraene (COT) has also been studied using both cyclic and square wave voltammetry [26]. For CV the two models preform comparably, but again SWV reveals the BV model to be better suited to the parameterisation of electrode kinetics, with the SMH model not able to accurately reproduce the experimental data.

Each of the three redox couples discussed here (MeNP, Eu(III) and COT) have been accurately fitted using the Butler-Volmer model with a transfer coefficient which deviates from $\frac{1}{2}$ and, as has been previously shown [4], in the limit $\lambda \to \infty$ the SMH model become identical to the BV model for $\alpha = \frac{1}{2}$. In order to better fit experimental data, it is likely that the SMH model will require modification so as to enable some asymmetry between the oxidative and reductive processes.

A possible route to improving the ability of the Marcus-Hush model to parameterise experimental voltammetry would be to remove Chidsey's assumption [27] that the forward and back reactions have the same reorganisation energy. Through the use of non-symmetrised Marcus theory [28], and the introduction of a second reorganisation energy (one for the forward reaction and another for the back reaction), it may be possible for this model to better parameterise electrochemical reactions while still giving physical insight into the underlying processes. It is also possible, however, that an additional parameter would only make fitting more difficult and raise possible questions of the uniqueness of sets of parameters which fit experimental data.

7.6 Conclusions

We have undertaken a comparison of the Butler-Volmer and symmetric Marcus-Hush kinetic formalisms using cyclic voltammetry at a microelectrode. We have shown that for each of the experimental systems studied, despite its simplicity, the use of Butler-Volmer kinetics using literature values of k_0 and α afforded accurate fitting of the experimental data. Reasonable fitting was also possible for the reduction of MeNP using SMH kinetics, however in order to achieve this it was necessary to discard both literature and calculated values of reorganisation energy in favour of using λ purely as a further fitting parameter, yielding a physically unrealistic value. Thus, we conclude that the symmetric Marcus-Hush model is less well suited for the *parameterisation* of solution-phase voltammetry than the Butler-Volmer model. That said, the Marcusian approach arguably remains more physically insightful, as will be demonstrated in the later chapters of this thesis.

Bibliography

[1] M. C. Henstridge, Y. Wang, J. G. Limon-Petersen, E. Laborda and R. G. Compton, *Chem. Phys. Lett.* **517** (2011) 29–35.

[2] H. Elzanowska, Z. Galus and Z. Borkowska, *J. Electroanal. Chem.* **157** (1983) 251–268.

[3] D. A. Corrigan and D. H. Evans, *J. Electroanal. Chem.* **106** (1980) 287–304.

[4] S. W. Feldberg, *Anal. Chem.* **82** (2010) 5176–5183.

[5] S. Fletcher and T. S. Varley, *Phys. Chem. Chem. Phys.* **13** (2011) 5359–5364.

[6] J. M. Savéant and D. Tessier, *Faraday Discuss. Chem. Soc.* **74** (1982) 57–72.

[7] R. G. Compton and C. E. Banks, *Understanding voltammetry* (Imperial College Press, London, 2010), 2nd edition.

[8] E. J. F. Dickinson, J. G. Limon-Petersen, N. V. Rees and R. G. Compton, *J. Phys. Chem. C* **113** (2009) 11157–11171.

[9] J. Mauzeroll, E. A. Hueske and A. J. Bard, *Anal. Chem.* **75** (2003) 3880–3889.

[10] J. G. Limon-Petersen, I. Streeter, N. V. Rees and R. G. Compton, *J. Phys. Chem. C* **112** (2008) 17175–17182.

[11] N. V. Rees, O. V. Klymenko, B. A. Coles and R. G. Compton, *J. Electroanal. Chem.* **534** (2002) 151–161.

[12] O. V. Klymenko, R. G. Evans, C. Hardacre, I. B. Svir and R. G. Compton, *J. Electroanal. Chem.* **571** (2004) 211–221.

[13] B. Timmer, M. Sluyters-Rehbach and J. Sluyters, *J. Electroanal. Chem.* **14** (1967) 181–191.

[14] W. F. Kinard and R. H. Philp, *J. Electroanal. Chem.* **25** (1970) 373–379.

[15] T. Rabockai, *Electrochim. Acta* **22** (1977) 489 – 490.

[16] S. R. Belding, E. I. Rogers and R. G. Compton, *J. Phys. Chem. C* **113** (2009) 4202–4207.

[17] S. R. Belding, J. G. Limon-Petersen, E. J. F. Dickinson and R. G. Compton, *Angew. Chem. Int. Ed.* **49** (2010) 9242–9245.

[18] A. N. Frumkin, *Electrochim. Acta* **9** (1964) 465 – 476.

[19] E. J. F. Dickinson and R. G. Compton, *J. Electroanal. Chem.* **661** (2011) 198–212.

[20] J. O. Bockris, S. U. M. Khan and D. B. Matthews, *J. Res. Inst. Catalysis. Hokkaido Univ.* **22** (1974) 1–21.

[21] J. M. Savéant and D. Tessier, *J. Electroanal. Chem.* **65** (1975) 57–66.

[22] D. H. Evans and A. G. Gilicinski, *J. Phys. Chem.* **96** (1992) 2528–2533.

[23] C. Kraiya, P. Singh and D. H. Evans, *J. Electroanal. Chem.* **563** (2004) 203–212.

[24] E. Laborda, Y. Wang, M. C. Henstridge, F. Martínez-Ortiz, A. Molina and R. G. Compton, *Chem. Phys. Lett.* **512** (2011) 133–137.

[25] Y. Wang, E. Laborda, M. C. Henstridge, F. Martinez-Ortiz, A. Molina and R. G. Compton, *J. Electroanal. Chem.* **668** (2012) 7–12.

[26] D. Suwatchara, N. V. Rees, M. C. Henstridge, E. Laborda and R. G. Compton, *J. Electroanal. Chem.* **665** (2012) 38–44.

[27] C. E. D. Chidsey, *Science* **251** (1991) 919–922.

[28] R. A. Marcus, *J. Chem. Phys.* **43** (1965) 679–701.

Chapter 8

Evaluation of the symmetric Marcus-Hush model at a high-speed channel microband electrode

This chapter presents a comparative evaluation of the symmetric Marcus-Hush and Butler-Volmer models of electrode kinetics under high mass transport conditions. Numerical simulation is employed in fitting voltammetry of the one-electron oxidation of 9,10-diphenylanthracene and the one-electron reduction of 2-nitropropane at a high-speed channel microband electrode using both kinetic formalisms.

In the case of diphenylanthracene, a nearly reversible system, the two models proved equally able to accurately fit the experimental data. However in the case of 2-nitropropane, a highly irreversible system, neither model was able to provide a satisfactory fit. It was possible to improve the fitting of the Butler-Volmer model by relaxing the usual requirement that $\alpha + \beta = 1$, justified by the very large difference in potential between the reductive and oxidative peaks.

This work has been published in the *Journal of Physical Chemistry C* [1]. The experiments described below were carried out by D. Suwatchara.

8.1 Introduction

We consider the symmetric Marcus-Hush and Butler-Volmer formalisms under hydrodynamic conditions, using a high-speed channel electrode system (HSChE). The HSChE has been described previously [2], and consists of a pressurised chamber containing the solution of interest and electrode assembly. The solution flows through a flow-cell containing the working electrode, and out through one of three capillaries to the exit at atmospheric pressure. The flow-cell is designed to smoothly accelerate the solution flow as it enters the channel, achieving volume flow rates of $4\,\mathrm{cm^3\,s^{-1}}$ and linear solution velocities of $20\,\mathrm{m\,s^{-1}}$ through the centre of the channel. This arrangement enables Reynolds' numbers approaching 10^4 to be reached whilst maintaining a well-defined laminar flow profile. It has been found that the measured $E_\mathrm{f}^\ominus$ is independent of scan rate at a given volume flow rate of solution, and the channel electrode is designed such that no distortions due to Ohmic losses are observed for fully supported systems [3].

The HSChE was chosen over other hydrodynamic microelectrode arrangements due to its reliable and extensive use in accurately measuring a wide range of electron transfer kinetics [4]. Previous studies using the HSChE have widely utilised the Butler-Volmer formalism for interpretation of experimental data, but it has also been used with particular success to verify results of semi-classical Marcus theory [5–8].

As test systems for use in the HSChE we have selected the one-electron reduction of 2-nitropropane (2NP) and the one-electron oxidation of 9,10-diphenylanthracene (DPA). 2NP has been reported as having a potential-dependent transfer coefficient: a feature suggestive of Marcusian kinetics [9]. Additionally, substituted anthracenes such as DPA have been shown to obey the Marcusian relationship between heterogeneous rate constant and reorganisation energy [7]. Both DPA and 2NP have the additional benefit of being neutral molecules, thus minimising any possible double layer effects – although such effects are also explicitly considered and found to be negligible.

8.2 Theory

We consider the one-electron reaction $\mathrm{A} + \mathrm{e} \rightleftharpoons \mathrm{B}$. Both species A and B are dissolved in a solution which is flowing through a channel, with the reaction occurring at the surface of a microband electrode which is embedded in the bottom of the channel. A schematic diagram of the system is shown in Figure 8.1.

We assume that the solution contains an excess of supporting electrolyte such that migration may be neglected [10]. The width (w_e) of the electrode is much larger than its length (x_e) in the direction of flow, thus the problem may be reduced to two spatial

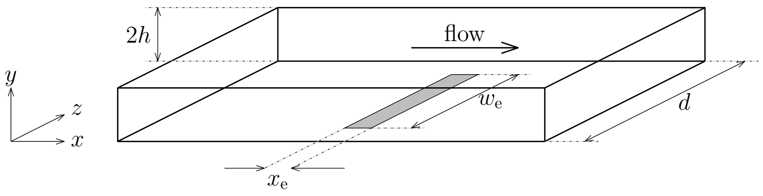

Figure 8.1: Schematic diagram of the high speed channel electrode.

dimensions. In addition we assume the flow to be laminar and the flow velocity to be sufficiently high to neglect axial diffusion [11].

The mass transport in this system may therefore described by:

$$\frac{\partial c_i}{\partial t} = D_i \frac{\partial^2 c_i}{\partial y^2} - v_x \frac{\partial c_i}{\partial x} \tag{8.1}$$

where c_i and D_i are the concentration and diffusion coefficient of species i respectively, t is time, x and y are distance parallel and perpendicular to the direction of flow respectively and v_x is the flow velocity, given by:

$$v_x = v_0 \left[1 - \left(\frac{h - y}{h} \right)^2 \right] \tag{8.2}$$

where v_0 is the flow velocity in the centre of the channel and h is the half-height of the channel. For convenience, the flow rate is generally quoted as a volume flow rate:

$$V_\mathrm{f} = \frac{4}{3} h d v_0 \tag{8.3}$$

where V_f is the volume flow rate and d is the width of the channel.

At time $t = 0$ species A is uniformly present at concentration c^*_A and species B is absent. The top wall of the channel is considered as a zero-flux boundary and the flux at the electrode ($j_{\mathrm{A},0}$) is given by:

$$j_{\mathrm{A},0} = -k_\mathrm{red}\, c_{\mathrm{A},0} + k_\mathrm{ox}\, c_{\mathrm{B},0} \tag{8.4}$$

where k_ox and k_red are the rate constants for oxidation and reduction respectively and $c_{i,0}$ is the concentration of species i at the electrode surface.

Since axial diffusion is neglected, the simulation space is limited to the region directly above the electrode. Upstream of this region the concentrations of species A and B are assumed to remain at their initial concentrations. The region downstream of the electrode is not considered.

Equation (8.1) is discretised along with these boundary conditions using the space-marching backwards implicit method [12], over a regular grid along the x-axis and an expanding grid along the y-axis. This system of equations, when expressed in matrix form, is pentadiagonal and hence may be solved using the Thomas algorithm.

8.3 Experimental

Tetra-n-butylammonium perchlorate (TBAP, Fluka puriss grade), 9,10-diphenylanthracene (DPA, 98 % Aldrich), 2-nitropropane (2NP, 99 % Aldrich), and acetonitrile (HPLC grade, Fisher Scientific) were all used as received without further purification. Microband working electrodes of lengths (x_e) 12.5 and 40.5 µm and widths (w_e) 0.87 and 0.96 mm respectively, were fabricated in-house by sealing Pt foil (Goodfellow Cambridge Ltd, UK) into soda glass according to a published method [2]. The 12.5 and 40.5 µm electrodes were used for the DPA and 2NP investigations respectively. A silver quasi-reference and large surface area platinum coil counter electrode completed the three electrode arrangement.

The high-speed channel apparatus has been described previously, and the solution flow within it fully characterised and shown to be laminar under the conditions used within this study [2, 5–8, 11–14]. The fast-scan potentiostat, capable of ohmic drop compensation by means of an internal positive feedback circuit, was constructed in-house according to a design from Amatore *et al.* [15], and was operated in conjunction with the flow apparatus as described elsewhere [14].

For both redox couples there was no observed systematic variation of either $E_\mathrm{f}^\ominus$ or k_0 (as deduced from simulation) with varying flow rate or varying scan rate; thus the ohmic drop compensation is assumed to be working correctly and the resulting voltammetry is free from distortion.

8.4 Results and discussion

8.4.1 Determination of diffusion coefficients

In order to allow a rigorous comparison of the two models with experiment, we independently measured the diffusion coefficients of both reactant and product via double potential step chronoamperometry at a platinum microdisc (radius 10 µm). The direct use of a simulation model using finite electrode kinetics was not practical, since both k_0 and D are unknown, and so the following procedure was adopted.

First, the double potential step transients were simultaneously fitted for both diffusion coefficients and concentration using a previously reported program [16], based on the Shoup & Szabo expression (and therefore assuming *infinite* electrode kinetics [17]). In order to verify that the assumption of infinite electrode kinetics was accurate these diffusion coefficients were then used to model cyclic voltammetry, fixing both the formal potential and standard heterogeneous electron transfer rate constant.

These values were then used in a second simulation of the double potential step chronoamperograms using a program based on *finite* electrode kinetics [18]. For both systems excellent agreement was observed between the values extracted assuming infinite electrode kinetics and the literature.

8.4.2 Oxidation of 9,10-diphenylanthracene

For this system the diffusion coefficients of both neutral and radical cation species were found to be equal taking the value of $1.4 \times 10^{-5}\,\mathrm{cm^2\,s^{-1}}$. Linear sweep and cyclic voltammetry was then recorded at a 12.5 µm platinum microband electode for a solution containing 0.67 mM DPA and 0.1 M TBAP in acetonitrile. The solution was flowed at a rate of $0.14\,\mathrm{cm^3\,s^{-1}}$ and voltammetry was recorded for scan rates in the range $200\,\mathrm{mV\,s^{-1}}$ to $2\,\mathrm{kV\,s^{-1}}$, encompassing both steady-state and transient voltammetry.

The voltammetry was then fitted using both kinetic models across the entire range of scan rates. The best-fit parameters, *i.e.* those which produced voltammetry yielding the lowest MSAD value, are shown in Table 8.1. Typical transients showing excellent fitting for both models is shown in Figure 8.2.

For the BV model the best-fit parameters were found to be $k_0 = 0.83\,\mathrm{cm\,s^{-1}}$ and α

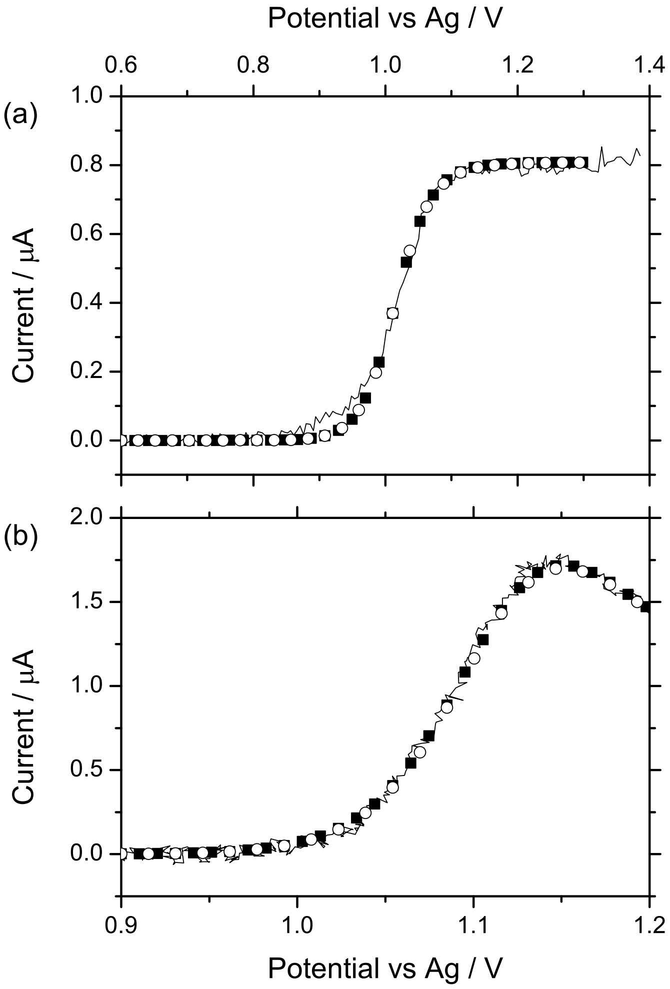

Figure 8.2: Experimental linear sweep voltammetry of DPA oxidation (solid line) compared to Butler-Volmer (black squares) and Marcus-Hush (white circles) theoretical results for a volume flow rate of $0.14\,\mathrm{cm^3\,s^{-1}}$ and voltage scan rates of (a) $1\,\mathrm{V\,s^{-1}}$ and (b) $1\,\mathrm{kV\,s^{-1}}$. Simulation parameters are as given in Figure 8.1.

	BV	SMH
k_0 / $\mathrm{cm\,s^{-1}}$	0.83 ± 0.15	0.85 ± 0.17
α	0.49 ± 0.02	–
λ / eV	–	0.58 ± 0.08
$E_{\mathrm{f}}^{\ominus}$ / V	1.18 ± 0.3	1.18 ± 0.3
% MSAD	3.1 ± 0.8	3.0 ± 0.7

Table 8.1: Best-fit parameters for the oxidation of DPA.

= 0.49, which are consistent with literature values of k_0 = 0.94 cm s^{-1} and α = 0.53 [7]. The best-fit parameters for the SMH model were k_0 = 0.85 cm s^{-1} and λ = 0.58 eV. This value of the reorganisation energy agrees well with the outer-sphere reorganisation energy of 0.50 eV calculated using Equation (5.4) given in Chapter 5.

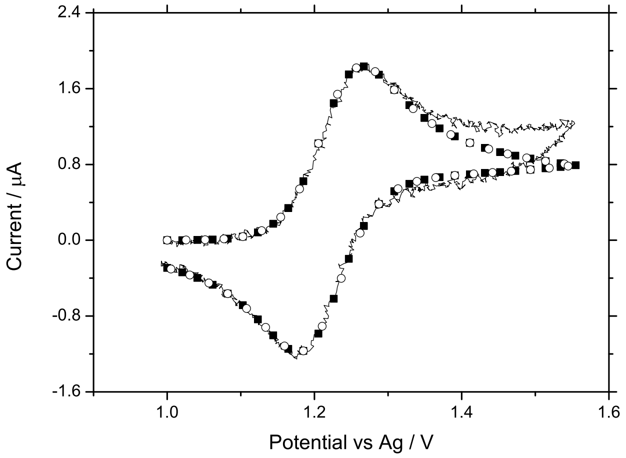

Figure 8.3: Experimental cyclic voltammetry of DPA oxidation (background subtracted) measured at a volume flow rate of 0.14 cm^3 s^{-1} and voltage scan rate of 1 kV s^{-1} (solid line), along with simulations using BV (black squares) and SMH (white circles). Simulation parameters are as given in Figure 8.1. The high currents at $E > 1.4$ V are due to the influence of the nearby second oxidation wave.

Excellent fitting is permitted by both models, as demonstrated by the extremely small MSAD values shown in Table 8.1. Equally significant is that there is no discernible difference between the two models in their ability to fit the experimental data for this highly reversible system.

8.4.3 Reduction of 2-nitropropane

For this system the diffusion coefficients of the neutral and radical anion species were measured as 3.1×10^{-5} cm^2 s^{-1} and 2.7×10^{-5} cm^2 s^{-1} respectively. No literature values could be found for 2NP species, but the related t-nitropropane was reported to have a value of 3×10^{-5} cm^2 s^{-1} [9, 19].

Cyclic and linear sweep voltammetry was recorded at a 40.5 µm platinum microband electrode for a solution of 2.65 mM 2NP and 0.1 M TBAP in acetonitrile. The solution was flowed at a rate of 0.14 cm^3 s^{-1} and voltammetry was recorded for scan rates in the range $200\,\mathrm{mV\,s^{-1}}$ to $2\,\mathrm{kV\,s^{-1}}$. Due to the high rates of mass transport, combined with the highly irreversible nature of the system, the anodic peak was only clearly observable for cyclic voltammetry at scan rates exceeding $1\,\mathrm{kV\,s^{-1}}$.

Fitting of the experimental voltammetry was then performed using both the Butler-Volmer and symmetric Marcus-Hush models. The best-fit parameters are given in Table 8.2.

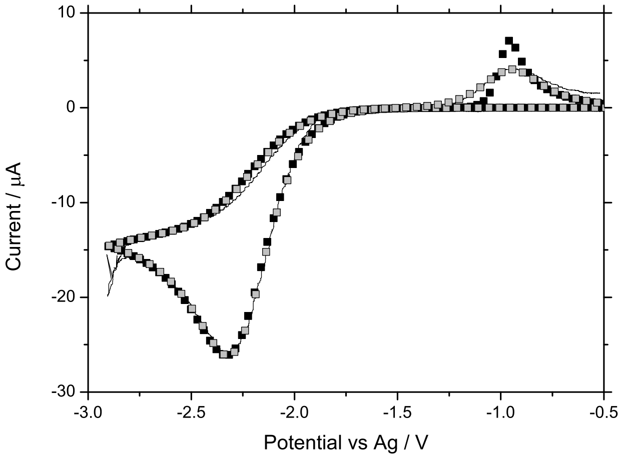

Figure 8.4: Experimental cyclic voltammetry of 2NP reduction (solid line) compared to best-fit simulations using the BV model with $\alpha+\beta = 1$ (black squares) and with $\alpha+\beta \neq 1$ (grey squares). The scan rate is $1\,\mathrm{kV\,s^{-1}}$ and the volume flow rate is $0.14\,\mathrm{cm^3\,s^{-1}}$.

The best fit achieved for the BV model used $k_0 = 7.0 \times 10^{-5}\,\mathrm{cm\,s^{-1}}$ and $\alpha = 0.24$, however this did not yield an accurate fit as can be seen in Figure 8.4. While the reductive peak is fitted very closely, the simulated oxidative peak is significantly larger and 'sharper' than the experimental peak. This poor fit is reflected in the large average MSAD value of 19.0 %.

However, a variable transfer coefficient has been reported for the related reduction of t-nitrobutane at Pt electrodes in acetonitrile [9]. The value reported for $\frac{\mathrm{d}\alpha}{\mathrm{d}E}$ is $0.4\,\mathrm{V^{-1}}$ which, considering the forward and back peaks are separated by more the 1.5 V, suggests that the transfer coefficients for the oxidative and reductive processes ought to differ substantially. We therefore relax the usual requirement that $\alpha + \beta = 1$, which only holds rigorously if α and β are defined simultaneously at the same potential. This is justifiable considering that the energetic environments in which the oxidation and reduction occur are likely quite different and thus the principle of microscopic reversibility is not violated

	BV		SMH	
	$\alpha+\beta=1$	$\alpha+\beta\neq 1$	$\lambda_{\text{best fit}}$	$\lambda_{\text{literature}}$
k_0 / $10^{-5}\,\mathrm{cm\,s^{-1}}$	7.0 ± 3.0	95 ± 15	5.0 ± 1.0	0.7 ± 0.3
α	0.24 ± 0.02	0.24 ± 0.02	–	–
β	0.76 ± 0.02	0.24 ± 0.02	–	–
λ / eV	–	–	1.0 ± 0.1	2.5 ± 0.1
$E_f^{\ominus}$ / V	-1.32 ± 0.04	-1.66 ± 0.05	-1.64 ± 0.08	-1.68 ± 0.06
% MSAD	19.0 ± 4.9	7.1 ± 0.5	10.1 ± 2.1	22.1 ± 3.2

Table 8.2: Simulation results for 2NP. Note that the use of a quasi-reference electrode is the source of the error in $E_f^{\ominus}$.

[20].

With this modification it is possible to obtain excellent fitting of the experimental data, for both forward and back peaks (see Figure 8.4), resulting in a much smaller MSAD value of 7.1 %.

The SMH model is able to provide a moderate fit, MSAD 10.1 %, when the reorganisation energy takes the value 1.0 eV. The best-fit parameters are given in Table 8.2 and some typical voltammetry is shown in Figure 8.5.

However, the value of the reorganisation energy for this system has been calculated to lie within the range 2.2 – 2.8 eV, comprising an outer sphere contribution (calculated to be 1.4 – 2.0 eV according to Equation (5.4)) and an inner sphere contribution (0.8 eV according to the DFT calculations reported by Kraiya *et al.* [21]).

Taking a mean value of 2.5 eV yields very poor agreement between simulation and experiment for the reductive peak, although there is better agreement in the oxidative wave. The overall effect of using a ‘literature’ value of reorganisation energy, rather than the best-fit value, is to increase the MSAD to 22.1 %.

However, unlike the dichotomy outlined above for the BV model, there is no obvious physical justification for lowering λ to a value as small as 1.0 eV. The solvent reorganisation energy alone is larger than this figure and a sizeable inner-sphere contribution has been long established for the reduction of nitroalkanes [21]. Significantly, even when the reorganisation energy takes a very small value, the quality of fit is still not as good as

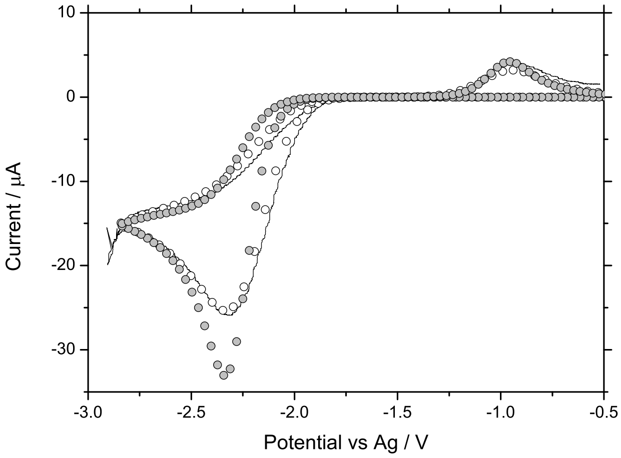

Figure 8.5: Experimental cyclic voltammetry of 2NP reduction (solid line) compared to best-fit simulations using the SMH model with a best-fit reorganisation energy (1.0 eV, white circles) and a ‘literature’ reorganisation energy (2.5 eV, grey circles). The scan rates is $1\,\mathrm{kV\,s^{-1}}$ and the volume flow rate is $0.14\,\mathrm{cm^3\,s^{-1}}$.

that achieved for Butler-Volmer kinetics (with $\alpha + \beta \neq 1$).

8.5 Conclusions

The Butler-Volmer and symmetric Marcus-Hush models of heterogeneous electron transfer kinetics have been compared under high mass transport conditions and the quality of the fits to experimental data quantified. In the case of DPA oxidation no significant measurable differences were found between the two models and excellent fits to cyclic and linear sweep voltammetry experiments were obtained. For 2NP the best fit was achieved using the Butler-Volmer model when the oxidative and reductive transfer coefficients were varied separately. The symmetric Marcus-Hush model was also able to produce reasonable fits to experiment, however in order to achieve this it was necessary to discard the ‘literature’ value of reorganisation energy in favour of using λ as a purely fitting parameter.

Although the symmetric Marcus-Hush model may arguably provide greater insight into the underlying processes occurring, on the basis of the systems considered here, the Butler-Volmer formalism may remain the preferred model for the parameterisation, if nothing more, of experimental data.

Bibliography

[1] D. Suwatchara, M. C. Henstridge, N. V. Rees and R. G. Compton, *J. Phys. Chem. C* **115** (2011) 14876–14882.

[2] N. V. Rees, R. A. W. Dryfe, J. A. Cooper, B. A. Coles, R. G. Compton, S. G. Davies and T. D. McCarthy, *J. Phys. Chem.* **99** (1995) 7096–7101.

[3] B. Coles, R. Compton, J. Larsen and R. Spackman, *Electroanalysis* **8** (1996) 913–917.

[4] N. Rees and R. Compton, *Russ. J. Electrochem.* **44** (2008) 368–389.

[5] A. D. Clegg, N. V. Rees, O. V. Klymenko, B. A. Coles and R. G. Compton, *J. Electroanal. Chem.* **580** (2005) 78–86.

[6] A. D. Clegg, N. V. Rees, O. V. Klymenko, B. A. Coles and R. G. Compton, *ChemPhysChem* **5** (2004) 1234–1240.

[7] A. D. Clegg, N. V. Rees, O. V. Klymenko, B. A. Coles and R. G. Compton, *J. Am. Chem. Soc.* **126** (2004) 6185–6192.

[8] N. V. Rees, A. D. Clegg, O. V. Klymenko, B. A. Coles and R. G. Compton, *J. Phys. Chem. B* **108** (2004) 13047–13051.

[9] D. A. Corrigan and D. H. Evans, *J. Electroanal. Chem.* **106** (1980) 287–304.

[10] E. J. F. Dickinson, J. G. Limon-Petersen, N. V. Rees and R. G. Compton, *J. Phys. Chem. C* **113** (2009) 11157–11171.

[11] J. A. Alden and R. G. Compton, *J. Electroanal. Chem.* **404** (1996) 27–35.

[12] R. G. Compton, M. B. G. Pilkington and G. M. Stearn, *J. Chem. Soc. Faraday Trans.* **84** (1988) 2155–2171.

[13] N. V. Rees, O. V. Klymenko, B. A. Coles and R. G. Compton, *J. Electroanal. Chem.* **534** (2002) 151–161.

[14] N. V. Rees, O. V. Klymenko, E. Maisonhaute, B. A. Coles and R. G. Compton, *J. Electroanal. Chem.* **542** (2003) 23–32.

[15] C. Amatore, C. Lefrou and F. Pflüger, *J. Electroanal. Chem.* **270** (1989) 43–59.

[16] O. V. Klymenko, R. G. Evans, C. Hardacre, I. B. Svir and R. G. Compton, *J. Electroanal. Chem.* **571** (2004) 211–221.

[17] R. G. Compton and C. E. Banks, *Understanding voltammetry* (Imperial College Press, 2010), 2nd edition.

[18] S. R. Belding, E. I. Rogers and R. G. Compton, *J. Phys. Chem. C* **113** (2009) 4202–4207.

[19] J. M. Savéant and D. Tessier, *J. Electroanal. Chem.* **65** (1975) 57–66.

[20] W. J. Albery, *Electrode Kinetics* (Clarendon Press, 1975).

[21] C. Kraiya, P. Singh and D. H. Evans, *J. Electroanal. Chem.* **563** (2004) 203–212.

Chapter 9

Redox systems obeying Marcus-Hush electrode kinetics do not obey the Randles–Ševčík equation for linear sweep voltammetry

The cyclic voltammetry of the reaction of a solution-phase species at a macroelectrode under semi-infinite diffusion is simulated assuming irreversible electrode kinetics within the symmetric Marcus-Hush model. The resulting peak currents are shown to deviate from the square root dependence on voltage scan rate predicted by the Randles–Ševčík equation. Simulated voltammetry of a surface-bound redox couple also shows deviations from the expected linear dependence of peak current on scan rate.

These numerical findings are supported by analytical arguments and they provide a simple method for a critical analysis of the kinetic model. In particular the sheer extent of published experimental work containing linear Randles–Ševčík plots suggests the need for significant refinement of the Marcus-Hush-Chidsey model before it is suitable for the analysis of experimental voltammetry.

This work has been published in the *Journal of Electroananlytical Chemistry* [1]. The analytical results were derived by E. J. F Dickinson and the simulations shown in Figure 9.3 were carried out in collaboration with E. Laborda.

9.1 Introduction

The use of the Randles–Ševčík equation [2, 3] is ubiquitous in experimental electrochemistry. Its prediction of peak current varying with the square root of voltage scan rate is an important analytical result, indicating that a redox couple is dissolved in solution rather than adsorbed on the electrode surface, the latter being identified by a linear relationship between peak current and scan rate [4].

While the behaviour of reversible redox systems is determined by thermodynamics, the analysis of irreversible systems as a function of scan rate can yield electrode kinetic data. The derivation of the Randles–Ševčík equation for irreversible couples assumes, however, that "the rate of electron transfer is an exponential function of the electrode potential" [5], *i.e.* it assumes Butler-Volmer kinetics. For an irreversible, one-electron, solution-phase oxidation the peak current, I_p, assuming Butler-Volmer kinetics is given by

$$I_\mathrm{p} = 0.4958 \left[\frac{(1-\alpha)F}{RT}\right]^{\frac{1}{2}} FAc^* D^{\frac{1}{2}} v^{\frac{1}{2}} \tag{9.1}$$

where A is the geometric area of the electrode, c^* is the bulk reactant concentration, D is the reactant diffusion coefficient, v is the voltage scan rate and α is the transfer coefficient. F, R and T have their usual meanings.

In this chapter we use both numerical and analytical methods to examine whether the equations governing the variation of peak current with scan rate hold when using a different kinetic model, namely the symmetric Marcus-Hush model [6, 7], for both solution-phase and surface-bound redox systems. In the limit of irreversible kinetics the peak current for a one-electron surface-bound redox couple is given by [8]

$$I_\mathrm{p} = \frac{F}{RT}\frac{\alpha F A \Gamma^*}{2.718}\, v \tag{9.2}$$

where Γ^* is the initial coverage of reactant.

We examine the conditions under which significant differences may be expected, with deviations from classical Randles–Ševčík behaviour providing an experimental method for the critical assessment of the symmetric Marcus-Hush kinetic formalism.

9.2 Theory

The voltammetry for solution-phase redox couples was simulated using the same model described in Chapter 7, with the exception that Fick's second law is solved in cartesian coordinates rather than in spherical polar coordinates:

$$\frac{\partial c}{\partial t} = D\frac{\partial^2 c}{\partial x^2} \tag{9.3}$$

where x is distance perpendicular to the planar electrode surface.

The voltammetry for surface-bound redox couples uses the model outlined in Chapter 6.

9.3 Scan rate dependence of the peak current

This section makes extensive use of dimensionless variables, which are defined in Chapter 2.

9.3.1 Development of a general integral equation

Diffusion-only mass transport is given by Fick's 2nd Law, which for a linear space is:

$$\frac{\partial C}{\partial \tau} = \frac{\partial^2 C}{\partial X^2} \tag{9.4}$$

If the applied overpotential is perturbed as:

$$\theta = \theta_{\mathrm{i}} + \sigma\tau \tag{9.5}$$

then we can define a coordinate θ' which is scaled to scan rate:

$$\theta' = \theta - \theta_{\mathrm{i}} = \sigma\tau \tag{9.6}$$

Hence

$$\sigma\frac{\partial C}{\partial \theta'} = \frac{\partial^2 C}{\partial X^2} \tag{9.7}$$

Now, if $C = 1$ initially, and the outer boundary condition is $C \to 1$ as $X \to \infty$, the general solution for C in the Laplace space is:

$$\mathcal{L}_{\theta' \to s'} \left\{ C(X, \theta') \right\} = \bar{C}(X, s') = \frac{1}{s'} + B(s') \exp(-X\sqrt{s'\sigma}) \tag{9.8}$$

Hence

$$\frac{\partial \bar{C}}{\partial X} = -\sqrt{s'\sigma}\, B(s') \exp(-X\sqrt{s'\sigma}) \tag{9.9}$$

and

$$\bar{C} = \frac{1}{s'} - \frac{\frac{\partial \bar{C}}{\partial X}}{\sqrt{s'\sigma}} \tag{9.10}$$

On inverse transformation, from application of the convolution theorem it follows that:

$$C(X, \theta') = 1 - \int_0^{\theta'} \frac{\partial C(X, u)}{\partial X} \frac{du}{\sqrt{\pi\sigma(\theta' - u)}} \tag{9.11}$$

Defining $C_0(\theta') = C(0, \theta')$ and $j(\theta') = (\partial C/\partial X)_{X=0}$, we derive the following general relationship:

$$C_0 = 1 - \frac{1}{\sqrt{\pi\sigma}} \int_0^{\theta'} \frac{j(u)\, du}{\sqrt{\theta' - u}} \tag{9.12}$$

This general mass transport relation is of direct use to the solution for the current if the surface flux obeys a simple first-order relationship:

$$j(\tau) = K_0\, f(\theta)\, C_0(\tau) \tag{9.13}$$

Both the irreversible Butler–Volmer and irreversible Marcus–Hush–Chidsey boundary conditions obey this general form. Hence, transforming into the coordinate θ':

$$j(\theta') = K_0\, f(\theta_\mathrm{i} + \theta')\, C_0(\theta') \tag{9.14}$$

On substitution into the integral expression, an integral equation for C_0 results, which is a Volterra equation of the second kind:

$$c_0(\theta') + \frac{K^0}{\sqrt{\pi\sigma}} \int_0^{\theta'} f(\theta_i + u) \frac{c_0(u)\, du}{\sqrt{\theta' - u}} = 1 \tag{9.15}$$

or equivalently

$$C_0(\theta') + \frac{K_0}{\sqrt{\pi\sigma}} \int_0^{\theta'} f(\theta_i + \theta' - u) C_0(\theta' - u) \frac{du}{\sqrt{u}} = 1 \tag{9.16}$$

9.3.2 Analysis of the integral equation for special cases of f

In general the solution to Equation (9.16) depends on the coefficients K_0, σ and θ_i. However, let us suppose a special case in which multiplying the function $f(x)$ by a constant shifts it on the abscissa, but does not otherwise affect it. This is true for the exponential function. This property may be expressed:

$$\lambda\, f(x) \equiv f(x + g(\lambda)) \tag{9.17}$$

Therefore the constants may be absorbed into the function f:

$$C_0(\theta') + \int_0^{\theta'} f(\theta' + \Delta\theta - u) C_0(\theta' - u) \frac{du}{\sqrt{u}} = 1 \tag{9.18}$$

and so a general solution $C_0(\theta', \Delta\theta)$ can be defined. Defining the voltammetric waveform function $\chi(x, \Delta\theta)$ as:

$$\chi(x, \Delta\theta) = f(x + \Delta\theta)\, C_0(x) \tag{9.19}$$

we ensure that the unknown $\chi(x, \Delta\theta)$ tends to zero when negligible current is drawn, *i.e.* where $f(x + \Delta\theta) \to 0$. Then the integral equation can be written as:

$$\chi(\theta', \Delta\theta) + f(\theta' + \Delta\theta) \int_0^{\theta'} \chi(\theta' - u, \Delta\theta) \frac{du}{\sqrt{u}} = f(\theta' + \Delta\theta) \tag{9.20}$$

Is χ a strong function of $\Delta\theta$? This can be assessed by altering the coefficient by the addition of a, so considering $\chi(\theta', \Delta\theta + a)$, which from definition (Equation (9.20)) satisfies:

$$\chi(\theta', \Delta\theta + a) + f(\theta' + \Delta\theta + a) \int_0^{\theta'} \chi(\theta' - u, \Delta\theta + a) \frac{du}{\sqrt{u}} = f(\theta' + \Delta\theta + a) \tag{9.21}$$

Now considering the original function with an offset of a in the abscissa, *i.e.* $\chi(\theta' + a, \Delta\theta)$, we can see that the offset in potential affects the function f identically to altering $\Delta\theta$:

$$\chi(\theta' + a, \Delta\theta) + f(\theta' + \Delta\theta + a) \int_0^{\theta' + a} \chi(\theta' + a - u, \Delta\theta) \, \frac{du}{\sqrt{u}} = f(\theta' + \Delta\theta + a) \qquad (9.22)$$

If the rate of reaction $f(\theta' + \theta_\mathrm{i})$ is negligible between $\theta' = 0$ and $\theta' = a$ at the beginning of the potential sweep, such that f tends to zero in this domain, then equally χ is zero in range. This can be ensured by requiring that $\theta_\mathrm{i} \ll 0$. Hence

$$\int_{\theta'}^{\theta' + a} \chi(\theta' + a - u, \Delta\theta) \, \frac{du}{\sqrt{u}} \approx 0 \qquad (9.23)$$

Therefore

$$\chi(\theta' + a, \Delta\theta) + f(\theta' + \Delta\theta + a) \int_0^{\theta'} \chi(\theta' + a - u, \Delta\theta) \, \frac{du}{\sqrt{u}} \approx f(\theta' + \Delta\theta + a) \qquad (9.24)$$

from which it follows that, subject to the above conditions:

$$\chi(\theta', \Delta\theta + a) \approx \chi(\theta' + a, \Delta\theta) \qquad (9.25)$$

because the defining equations for these two functions, given by Equation (9.21) and Equation (9.24) respectively, are identical. We conclude that $\chi(\theta')$ is only affected by the exact value of $\Delta\theta$ in terms of a horizontal shift of the waveform on the potential axis, so long as the condition of initially negligible rate of reaction remains satisfied. Hence, the maximal value of $\chi(\theta')$ does not depend on K_0, σ or θ_i, although the absolute potential where this maximum occurs *does* depend on these parameters.

Therefore, if the maximum current is j_max and its associated potential is θ_max, and the maximum value of the general function χ is χ_max:

$$j_\mathrm{max} = K_0 f(\theta_\mathrm{max}) \, c(\theta_\mathrm{max}) = K_0 f(\theta_\mathrm{max}) \, \frac{\chi_\mathrm{max}}{\frac{K_0}{\sqrt{\pi\sigma}} f(\theta_\mathrm{max})} = \chi_\mathrm{max} \sqrt{\pi\sigma} \qquad (9.26)$$

thus demonstrating that peak current is proportional to $\sqrt{\sigma}$, irrespective of the actual value of σ.

This above analysis is entirely dependent on the condition of Equation (9.17), which is satisfied for the exponential Butler–Volmer boundary condition but not for the parabolic

Marcus–Hush integral. Therefore, we can expect the peak current to be a more complex function of σ (as well as the other parameters) if Marcus–Hush boundary conditions are applied, and the simple relation $j_{\text{max}} \propto \sqrt{\sigma}$ does not hold.

9.4 Solution-phase results

Cyclic voltammetry was simulated using symmetric Marcus-Hush kinetics for a range of scan rates and compared with the Randles–Ševčík equation. A macrodisc radius, of 1 mm was assumed and the diffusion coefficient was set to be $10^{-5}\,\text{cm}^2\,\text{s}^{-1}$. Voltammetry was simulated over the range $100\,\text{mV}\,\text{s}^{-1}$ – $1\,\text{kV}\,\text{s}^{-1}$: from previous work Randles–Ševčík behaviour is expected over this range of scan rates [9].

The Randles–Ševčík equation (Equation (9.1)) predicts $I_{\text{p}} \propto \sqrt{v}$. Consequently plotting peak current against square root of scan rate, as in Figure 9.1, ought to yield a linear trend. The simulated voltammetry, however, clearly deviates from the expected linearity, particularly for high scan rates and for reorganisation energies of 1 eV and smaller. The extent of this non-linearity, which was predicted by the analytical treatment above, is highlighted in Figure 9.2 which shows a plot of the variation of $\frac{\partial I_{\text{p}}}{\partial \sqrt{v}}$ vs $\sqrt{v}$. Note that a very significant variation in Randles–Ševčík slope occurs in the range $10 < \vartheta < 200$, where

$$\vartheta = \frac{1}{k_0}\sqrt{\frac{vFD}{RT}} \tag{9.27}$$

For this range, which corresponds to $250\,\text{mV}\,\text{s}^{-1}$ – $100\,\text{V}\,\text{s}^{-1}$ in Figure 9.2, the change in slope is given in Table 9.1 for some typical values of reorganisation energy.

λ (eV)	Δ slope (%)
2.0	4.3
1.0	9.3
0.5	37.3

Table 9.1: Variation of Randles–Ševčík slope in the range $10 < \vartheta < 200$.

This deviation from Randles–Ševčík behaviour is also evident in the transition from reversible to irreversible voltammetry with increasing scan rate, as shown in Figure 9.3.

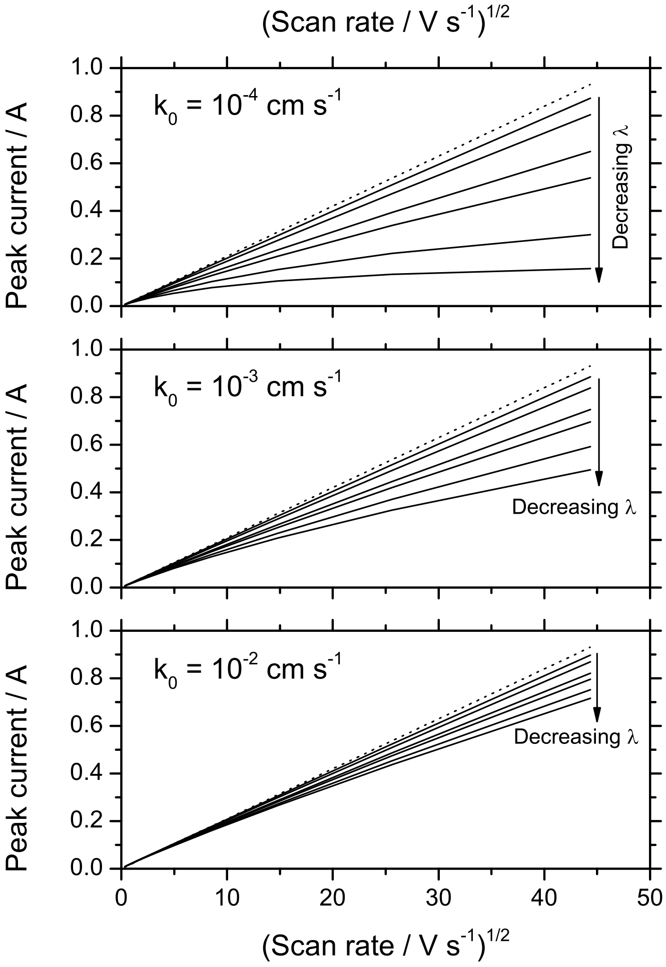

Figure 9.1: Plot of peak current against square root of scan rate for a solution-phase redox couple for a range of k_0 values. The dotted line shows the Randles–Ševčík equation for $\alpha = 0.5$, solid lines are simulated peak currents using symmetric Marcus-Hush kinetics: $\lambda = 0.5$, 0.6, 0.8, 1.0, 2.0 and 5.0 eV. $r_\mathrm{e} = 0.1\,\mathrm{cm}$, $D = 10^{-5}\,\mathrm{cm}^2\,\mathrm{s}^{-1}$ and $c^* = 1\,\mathrm{mM}$.

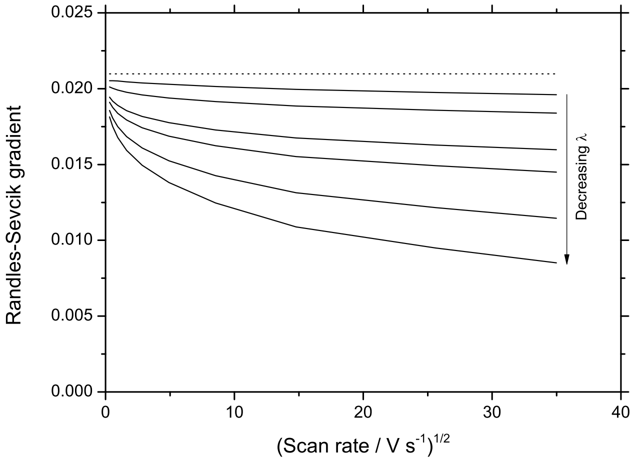

Figure 9.2: Plot of $\frac{\partial I_{\mathrm{P}}}{\partial \sqrt{v}}$ vs $\sqrt{v}$ for $k_0 = 10^{-3}\,\mathrm{cm\,s^{-1}}$. All parameters are as in Figure 9.1.

The Randles–Ševčík equations (for $\alpha = 0.5$) predict at most a *ca.* 30 % difference in peak current upon the transition from reversible to irreversible (Figure 9.3(a)). However, as shown in Figures 9.3, for symmetric Marcus-Hush kinetics the normalised peak current continues to decrease with scan rate, rather than reaching a limiting value as does the voltammetry simulated using the Butler-Volmer model. This observation has implications for electroanalysis in terms of the study of the analytical benefits expected from electrocatalyic effects, for example due to modification of the electrode surface. According to these results, under symmetric Marcus-Hush kinetics the increase in analytical sensitivity can be significantly greater than the 30 % predicted from Randles–Ševčík equations for reversible and irreversible systems [10, 11].

9.5 Surface-bound results

Equation (9.2) predicts a linear relationship between peak current and scan rate for voltammetry of a surface-bound species. Cyclic voltammetry simulated for a surface-bound couple over the scan rate range $1\,\mathrm{mV\,s^{-1}}$ to $1\,\mathrm{kV\,s^{-1}}$ yielded significant deviations from Equation (9.2) in a similar fashion to that observed for solution-phase voltammetry. The extent of this deviation is much greater for surface-bound species, however, because the electrode kinetics are not masked by rate-limiting mass transport. Figure 9.4 shows the variation of peak current with scan rate for a range of reorganisation energies and k_0

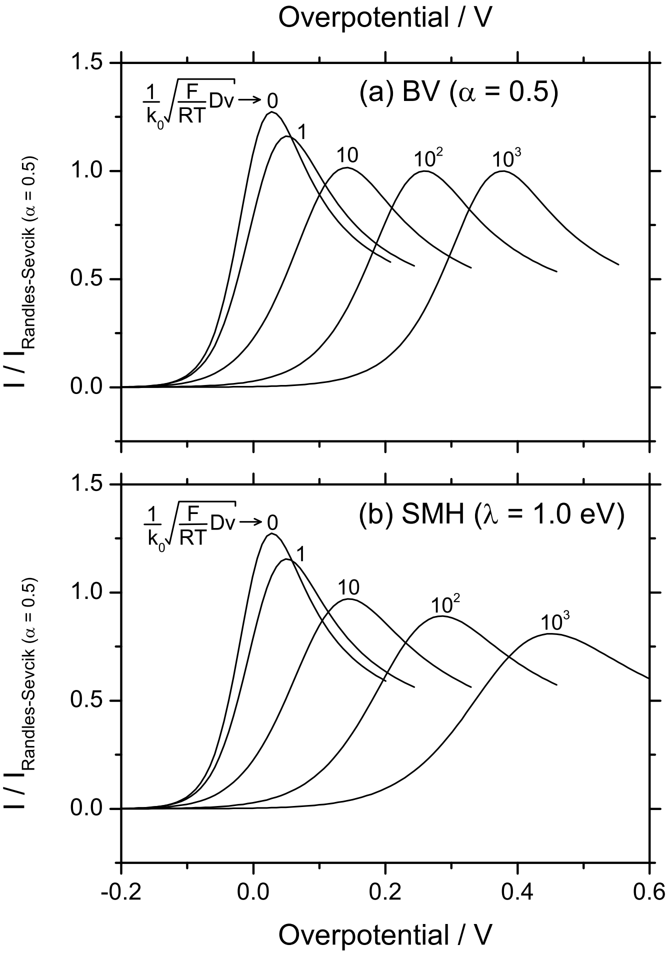

Figure 9.3: Linear sweep voltammetry simulated for a range of scan rates (or equivalently a range of k_0 values) demonstrating the differing behaviour of the BV and SMH models in the transition from reversible to irreversible behaviour.

values ranging from $0.1\,\mathrm{s}^{-1}$ up to $10\,\mathrm{s}^{-1}$. For all reorganisation energies a negative deviation from the expected trend is observed, particularly at higher scan rates. Again the extent of the curvature is most extreme for the smallest values of reorganisation energy and rate constant, this is shown more clearly in Figure 9.5 which plots $\frac{\partial I_\mathrm{p}}{\partial v}$ vs v.

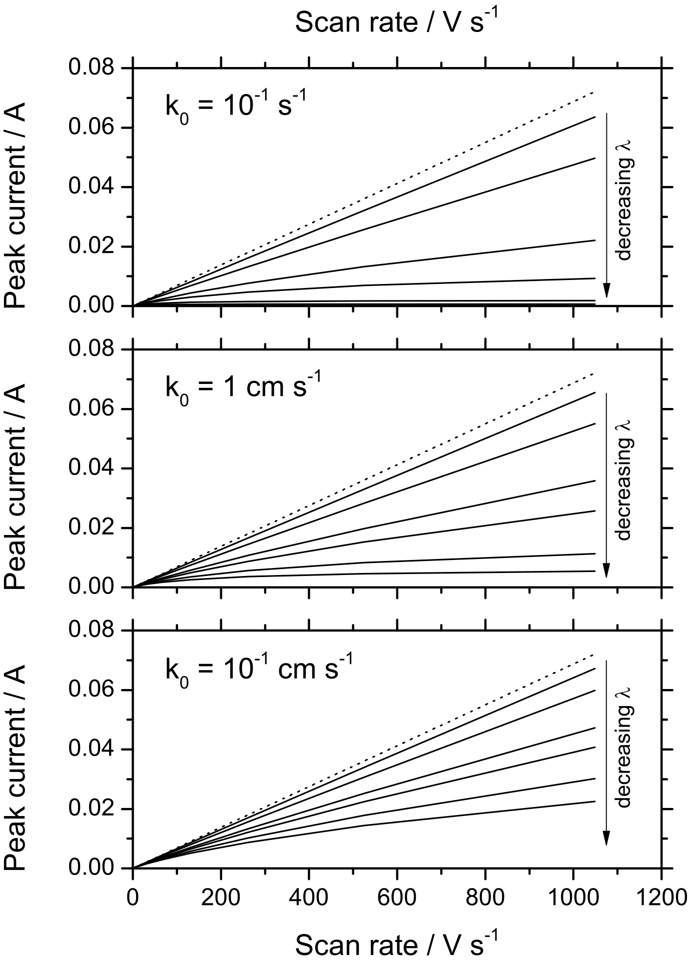

Figure 9.4: Plots of peak current against scan rate for a surface-bound redox couple for a range of k_0 values. The dotted line shows Equation (9.2) for $\alpha = 0.5$, solid lines are simulated peak currents using symmetric Marcus-Hush kinetics: $\lambda = 0.5$, 0.6, 0.8, 1.0, 2.0 and $5.0\,\mathrm{eV}$. $A = 0.1\,\mathrm{cm}^2$, $\Gamma^* = 10^{-9}\,\mathrm{mol\,cm}^{-2}$.

9.6 Discussion

The symmetric Marcus-Hush model has proven somewhat successful for the analysis of surface-bound redox systems through the ability to reproduce the curvature evident in

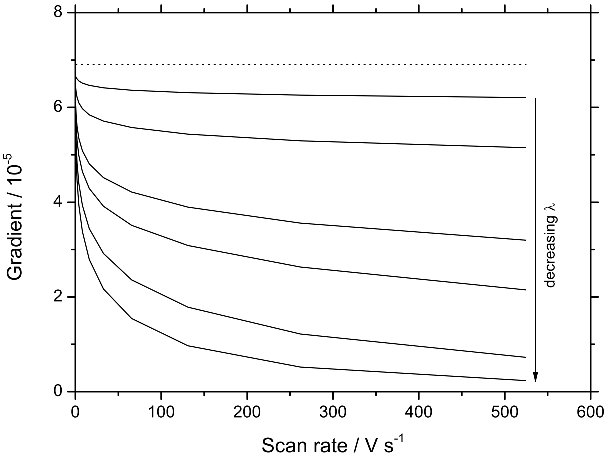

Figure 9.5: Plot of $\frac{\partial I_{\mathrm{p}}}{\partial v}$ vs v for $k_0 = 1\,\mathrm{s}^{-1}$. All parameters are as in Figure 9.4.

experimental Tafel plots [6], consequently a curved Tafel plot is taken to be evidence of Marcusian, rather than Butler-Volmer, kinetics. Recent work has also studied symmetric Marcus-Hush kinetics applied to solution-phase voltammetry both under diffusion-only [12] and diffusion-convection mass transport [13]. These works have compared symmetric Marcus-Hush and Butler-Volmer kinetics by fitting of the whole voltammetric waveshape.

The present results suggest that, according to the symmetric Marcus-Hush model, a curved Randles–Ševčík plot should be observed under certain experimental conditions. This observation should be most apparent for systems with small reorganisation energies and for high scan rates ($10 < \vartheta < 200$). These findings also suggest that such a deviation would be particularly evident for a surface-bound redox couple.

According to Marcus theory a small reorganisation energy leads to a fast rate constant, and vice versa, making the task of observing such a curved plot more difficult as the deviation is most apparent for small values of both λ and k_0. Nevertheless through the use of high scan rates one ought to be able to study systems with relatively high k_0 values (and therefore low λ values) under the appropriate conditions to observe deviations from Randles–Ševčík.

The literature, however, is replete with linear plots in accordance with Equations (9.1) and (9.2) and, to the author's knowledge, there are no reports of significant deviations from linearity such as the ones reported here. This, however, could potentially be a result of examining only a narrow range of scan rates, as is commonplace experimentally. In this case the trends in Figures 9.1 and 9.4 would appear almost linear, albeit with a non-zero intercept, and may be analysed using either Equation (9.1) or Equation (9.2). If all other variables are known (r_e, c, D etc) then analysing the slope will yield a value for α. The present results suggest that it may be prudent to check the consistency of this α value. This could be done via comparison with the value extracted via Tafel analysis.

An illustrative example of this comparison is shown in Figure 9.6 which shows voltammetry simulated for a dissolved redox couple using symmetric Marcus-Hush kinetics with $\lambda = 1\,\mathrm{eV}$ at a scan rate of $1\,\mathrm{V\,s^{-1}}$. Tafel analysis ($\ln I$ vs E) of this voltammogram yields $\alpha \approx 0.5$. Figure 9.6(a) shows a comparison with Butler-Volmer kinetics for this value and the discrepancy in peak current is plainly visible. While the value of diffusion coefficient also affects peak current, this may be fixed independently using a method such as potential step chronoamperometry. As such there are no parameters whose values may be "tweaked" to improve the quality of fit.

Figure 9.6(b) shows a comparison with BV for a larger value of $\alpha = 0.616$, which was extracted from Randles–Ševčík analysis of the slope in Figure 9.1. While Figure 9.6(b) shows close agreement between the two forward peaks after shifting the formal potential slightly, the back peaks differ markedly in both current and potential. The fitting of both oxidative and reductive peaks serves as another helpful check on the consistency of an α value extracted from Randles–Ševčík analysis.

9.7 Conclusion

Through numerical simulation of cyclic voltammetry we have demonstrated that a system obeying symmetric Marcus-Hush kinetics does not obey the Randles–Ševčík equation for an irreversible system. We have shown analytically that peak current scales with the square root of scan rate when the rate of electron transfer depends exponentially on potential, as is the case for Butler-Volmer kinetics. This relationship, however, does not hold for the Marcus-Hush kinetic model. We have also shown a similar deviation from Butler-Volmer theory for surface-bound redox systems.

The optimal experimental conditions for the verification of these results have been discussed, suggesting $10 < \vartheta < 200$. Where the deviation from linearity is not marked,

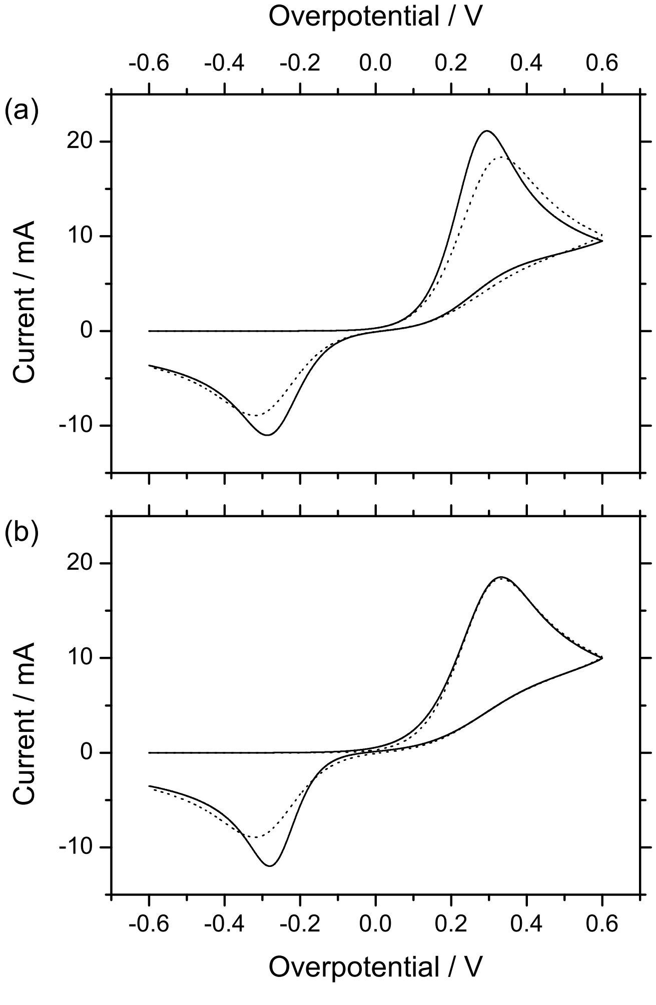

Figure 9.6: Cyclic voltammetry simulated using symmetric Marcus-Hush kinetics with $\lambda = 1\,\mathrm{eV}$ (dotted line) and Butler-Volmer kinetics (solid line) with (a) $\alpha = 0.5$ and (b) $\alpha = 0.616$. Other parameters are as in Figure 9.1.

assessment of the consistency of the α value extracted from the Randles–Ševčík equation is recommended, *e.g.* via Tafel analysis.

Bibliography

[1] M. C. Henstridge, E. Laborda, E. J. F. Dickinson and R. G. Compton, *J. Electroanal. Chem.* **664** (2012) 73–79.

[2] J. E. B. Randles, *Trans. Faraday Soc.* **44** (1948) 327–338.

[3] A. Sevcik, *Collect. Czechoslov. Chem. Commun.* **13** (1948) 349.

[4] R. G. Compton and C. E. Banks, *Understanding voltammetry* (Imperial College Press, London, 2010), 2nd edition.

[5] P. Delahay, *J. Am. Chem. Soc.* **75** (1953) 1190–1196.

[6] C. E. D. Chidsey, *Science* **251** (1991) 919–922.

[7] S. W. Feldberg, *Anal. Chem.* **82** (2010) 5176–5183.

[8] A. J. Bard and L. R. Faulkner, *Electrochemical Methods: Fundamentals and Applications* (Wiley, 2001), 2nd edition.

[9] A. S. Barnes, E. I. Rogers, I. Streeter, L. Aldous, C. Hardacre and R. G. Compton, *J. Phys. Chem. B* **112** (2008) 7560–7565.

[10] B. R. Kozub, N. V. Rees and R. G. Compton, *Sens. Actuat. B* **143** (2010) 539–546.

[11] E. Laborda, A. Molina, F. Martnez-Ortiz and R. G. Compton, *Electrochim. Acta* **73** (2012) 3–9.

[12] E. Laborda, Y. Wang, M. C. Henstridge, F. Martínez-Ortiz, A. Molina and R. G. Compton, *Chem. Phys. Lett.* **512** (2011) 133–137.

[13] D. Suwatchara, M. C. Henstridge, N. V. Rees and R. G. Compton, *J. Phys. Chem. C* **115** (2011) 14876–14882.

Chapter 10

Asymmetric Marcus theory: application to electrode kinetics

In the preceding chapters we have shown that the *symmetric* Marcus-Hush model is not able to provide accurate fitting of experimental voltammetry for diffusional systems. We now report the application of the *asymmetric* form of Marcus theory to the voltammetric study of electrode kinetics. The resulting four-parameter model accounts for discrepancies in the values of the inner-shell force constants and offers deeper insight to the changes involved in electron transfer processes at electrodes.

The variation of the electrochemical rate constant with the applied potential is examined, and seen to be in agreement with reported experimental deviations from the SMH model. The application of the asymmetric model to cyclic and square wave voltammetries is further reported.

This work, carried out in collaboration with E. Laborda, has been published in the *Journal of Electroanalytical Chemistry* [1].

10.1 Introduction

Thus far we have considered the symmetric form of Marcus theory, which models the Gibbs energy curves of the reactants and products as parabolae of equal curvature. Additionally, the density of metallic states and the extent of electronic coupling between metallic states and electroactive species are presumed to be independent of the applied potential. In the case of surface-bound redox couples, these assumptions have been supported by the reasonably successful description of many systems over several years [2–12].

These assumptions are brought into question, however, when the model is applied to the voltammetry of diffusional systems. The SMH model has been applied in the fitting of experimental cyclic voltammetry, square wave voltammetry and differential multi pulse voltammetry of several different redox systems, as well as to both diffusion-only and convective mass transport conditions (see Chapters 7–8 and references [6, 13–16]). Despite its foundations in the widely accepted microscopic Marcus model of electron transfer, the symmetric Marcus-Hush model has performed consistently poorly. Specifically, the results show that the SMH is not able to quantitatively describe the voltammetric responses of systems for which the transfer coefficient differs from $\frac{1}{2}$. By contrast, the empirical Butler-Volmer model has afforded consistently accurate fitting under a wide variety of experimental conditions and techniques.

Aditionally, it has been shown [17–22] that for quasi-reversible systems a peak splitting is expected for differential pulse voltammetries when the Butler-Volmer transfer coefficient deviates significantly from $\frac{1}{2}$. However, there exists no set of parameters for which the same peak split is observed using the symmetric Marcus-Hush model [22]. This phenomenon has been experimentally verified by Osteryoung *et al.* [19] using SWV for the reduction of Zn(II) to Zn(0) at mercury electrodes, with the split becoming more prominent with increasing frequency. Satisfactory fitting of the experimental voltammetry was achieved with $\alpha = 0.2$, but as discussed above, no fit is possible using symmetric Marcus-Hush theory.

Other experimental deviations from the SMH approach have been observed by various authors such as Tafel plots in which the anodic and cathodic branches are asymmetric. Weaver and co-workers observed this behaviour for metal aquo complexes [23] and analogous results have been obtained for some osmium [3, 4] and ferrocene [24–26] complexes attached to the electrode surface.

A possible explanation for these discrepancies is that the SMH model assumes that the force constants for reactants and products are equal. Given the change in charge taking place during the process, the vibrational modes and interactions with the solvent can be significantly different between the oxidised and reduced species, rendering this approximation invalid. Weaver and Hupp examined this aspect from calculated Gibbs energy curves [23] and pointed out the need for considering difference in force constants when examining electrochemical kinetics. Savéant and Tessier [27] also outlined this possibility as an explanation for the deviations from Marcus theory observed when studying the electroreduction of various nitrocompounds in acetonitrile and dimethylformamide.

In this chapter we remove this assumption, making use of the asymmetric form of Marcus theory to derive relationships for the heterogeneous rate constants when the force constants of the electroactive species differ. This new model of electrode kinetics is applied to the modeling of solution-phase redox systems for both cyclic and reverse scan square wave voltammetry and the results compared with those obtained using the SMH and BV models of electrode kinetics.

10.2 Theory

In Chapter 5 we saw that for the one-electron reduction $A + e \rightleftharpoons B$ occuring at the surface of an electrode we must consider electron transfer at the entire continuum of energy levels in the conduction band of the electrode. This approach leads to the following general form for the heterogeneous rate constants:

$$k_{\mathrm{red/ox}} = k_0 \, \frac{S_{\mathrm{red/ox}}(\theta, \Lambda)}{S_{\mathrm{red/ox}}(0, \Lambda)} \tag{10.1}$$

where Λ is the dimensionless reorganisation energy, θ is dimensionless overpotential, and $S_{\mathrm{red/ox}}(\theta, \Lambda)$ is an integral of the form:

$$S_{\mathrm{red/ox}}(\theta, \Lambda) = \int_{-\infty}^{\infty} \frac{\exp\left[-\Delta G^{\ddagger}_{\mathrm{red/ox}}(x)/RT\right]}{1 + \exp\left[\mp x\right]} \, dx \tag{10.2}$$

where x is an integration variable.

The symmetric form of Marcus theory [28] assumes that the Gibbs energy curves for the reactants and products both have the same curvature (*i.e.* they have equal force constants). This model, however, has been demonstrated to be unsuited to the fitting of diffusional voltammetry and so it is desirable to investigate the effect of removing the assumption of equal force constants.

Marcus considered the possibility of unequal force constants and presented expressions for the activation energy of the oxidative and reductive processes in Appendix IV of reference [28]:

$$\frac{\Delta G^{\ddagger}_{\mathrm{red/ox}}(x)}{RT} = \frac{\Lambda}{4}\left(1 \pm \frac{\theta + x}{\Lambda}\right)^2 + \frac{\Omega}{4}\left(\frac{\theta + x}{\Lambda}\right)\left[1 - \left(\frac{\theta + x}{\Lambda}\right)^2\right] + \frac{\Omega^2}{16\Lambda} \tag{10.3}$$

where we have defined a new kinetic parameter ω, which has a dimensionless analogue:

$$\Omega = \frac{F}{RT}\,\omega \tag{10.4}$$

This parameter accounts for the difference in curvature of the Gibbs energy curves and is given by:

$$\omega = \lambda_{\mathrm{i}} \langle l_{\mathrm{s}} \rangle \tag{10.5}$$

with λ_{i} being the inner-sphere reorganization energy and $\langle l_{\mathrm{s}} \rangle$ is related to the difference between the force constants of the oxidised and reduced species. They are defined thus:

$$\lambda_{\mathrm{i}} = \frac{1}{2}\sum_{\mathrm{s}} k_{\mathrm{s}} \left(\Delta q^0_{\mathrm{s}}\right)^2 \tag{10.6}$$

$$\langle l_{\mathrm{s}} \rangle = \frac{\sum\limits_{\mathrm{s}} k_{\mathrm{s}} \left(\Delta q^0_{\mathrm{s}}\right)^2 l_{\mathrm{s}}}{\sum\limits_{\mathrm{s}} k_{\mathrm{s}} \left(\Delta q^0_{\mathrm{s}}\right)^2} \tag{10.7}$$

where Δq^0_{s} is the difference in the equilibrium values for the sth normal mode coordinate of reactants and products, k_{s} and l_{s} are the symmetric and antisymmetric combinations of the force constants of the sth mode, $f^{\mathrm{ox}}_{\mathrm{s}}$ and $f^{\mathrm{red}}_{\mathrm{s}}$:

$$k_{\mathrm{s}} = \frac{2 f^{\mathrm{ox}}_{\mathrm{s}} f^{\mathrm{red}}_{\mathrm{s}}}{f^{\mathrm{ox}}_{\mathrm{s}} + f^{\mathrm{red}}_{\mathrm{s}}} \tag{10.8}$$

$$l_{\mathrm{s}} = \frac{f^{\mathrm{ox}}_{\mathrm{s}} - f^{\mathrm{red}}_{\mathrm{s}}}{f^{\mathrm{ox}}_{\mathrm{s}} + f^{\mathrm{red}}_{\mathrm{s}}} \tag{10.9}$$

Thus $\langle l_{\mathrm{s}} \rangle$ is related to the differences between the inner-shell force constants of reactants and products such that it increases in magnitude between 0 and 1 with the disparity of the values of the force constants. The sign of $\langle l_{\mathrm{s}} \rangle$ depends on whether the force constants are greatest in the oxidised or reduced species:

$$\begin{aligned} f_{\mathrm{s}}^{\mathrm{ox}} &> f_{\mathrm{s}}^{\mathrm{red}} \qquad \langle l_{\mathrm{s}}\rangle > 0 \\ f_{\mathrm{s}}^{\mathrm{ox}} &< f_{\mathrm{s}}^{\mathrm{red}} \qquad \langle l_{\mathrm{s}}\rangle < 0 \\ f_{\mathrm{s}}^{\mathrm{ox}} &= f_{\mathrm{s}}^{\mathrm{red}} \qquad \langle l_{\mathrm{s}}\rangle = 0 \end{aligned} \tag{10.10}$$

In the case of equal force constants, or when the average value does not change due to compensating effects (*i.e.* $\langle l_{\mathrm{s}}\rangle = 0$) then $\omega = 0$ and this asymmetric formulation reduces to the previously described symmetric version (described in Chapter 5).

In the derivation of the expressions for the activation energies (Equation (10.3)) only the first terms in the expansion of $\langle l_{\mathrm{s}}\rangle$ are considered. This enables us to generalize the solution for the heterogeneous rate constants but to restrict the number of adjustable parameters to four: $\{E_{\mathrm{f}}^{\ominus}, k_0, \lambda, \omega\}$. Note that when the force constants are known, the adjustable parameters are reduced to three since ω may be explicitly calculated.

For very large differences between the force constants, it is likely necessary to consider higher-order terms in the expansion of $\langle l_{\mathrm{s}}\rangle$ in order to obtain accurate results. This complicates both the computation and application of the kinetic model as it further increases the number of adjustable parameters. Further, additional knowledge of the properties of the electroactive species is required. This situation thus requires the particularisation of the solution to the system under study, although qualitative estimations may be made from the simpler expressions presented here.

The significance of neglecting higher-order corrections in $\langle l_{\mathrm{s}}\rangle$ was examined by comparison with results obtained from the 'complete' solution given by Equations (A6)-(A8) in Appendix IV of reference [28], assuming a coordination number for the electroactive species of 6.

We consider an extreme case for which $f_{\mathrm{s}}^{\mathrm{ox}}$ is twice as large as $f_{\mathrm{s}}^{\mathrm{red}}$ (*i.e.* $\langle l_{\mathrm{s}}\rangle = \frac{1}{3}$) and the outer-sphere reorganisation energy is negligible. For a reorganisation energy of 1 eV the contribution of higher-order terms to the activation energy is found to be negligible ($\leq 2\,\%$) for overpotentials up to *ca.* 150 mV at 298 K. For a larger reorganisation energy of 1.5 eV the higher-order terms are found to contribute negligibly for overpotentials up to *ca.* 350 mV at 298 K.

Note that the latter case is more likely since large differences in the force constants between the oxidised and reduced species will lead to significant changes in bond lengths and geometry and thus result in a large inner-shell reorganisation energy [23]. For less extreme differences between force constants, the contribution of higher-order terms in $\langle l_\mathrm{s} \rangle$ may be neglected at even larger overpotentials and as such the 'simple' expressions given in Equation (10.3) are likely sufficient to describe the majority of experimental systems.

Asymmetry may also arise from the solvation of the electroactive species beyond the inner coordination shell, however their treatment would require computer modeling of solvent coordination for each particular system. Such effects are not considered here.

10.3 Results and discussion

The variation of rate constants with potential for the new asymmetric Marcus-Hush (AMH) model is shown in Figure 10.1 for $\lambda = 1\,\mathrm{eV}$ and a range of values for ω.

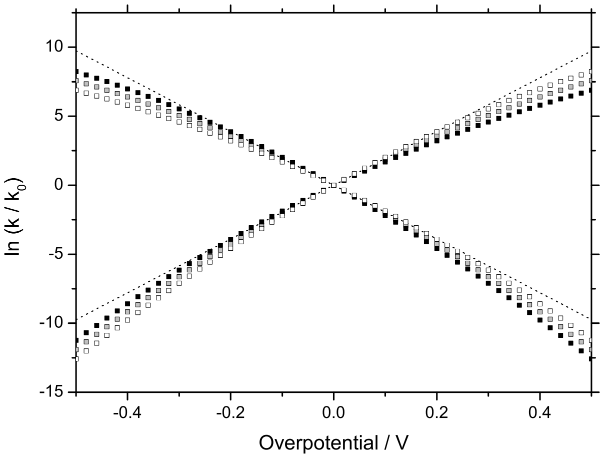

Figure 10.1: Variation of rate constants with applied potential for the Butler-Volmer model (dotted line, $\alpha = 0.5$) and asymmetric Marcus-Hush model with $\lambda = 1\,\mathrm{eV}$ and $\omega = -0.2\,\mathrm{eV}$ (white squares), $0.0\,\mathrm{eV}$ (grey squares) and $+0.2\,\mathrm{eV}$ (black squares).

Note that when $\omega = 0$ the AMH model reduces to the SMH model for which the rate constants are symmetrical about the formal potential. For $\omega > 0$ the reductive rate constant shows a steeper dependence on overpotential than for the symmetric model, whereas the oxidative rate constant varies more slowly with overpotential. The opposite trend is observed for $\omega < 0$. In all cases, as with the symmetric model, the rate constants begin to level off as overpotential increases in contrast with the Butler-Volmer model, for which the rate constants continue to increase exponentially *ad infinitum.*

Another important consequence of considering unequal force constants for the reactants and products is observed in the variation of the 'transfer coefficient', defined as $-\dfrac{\partial \ln k_{\mathrm{red}}}{\partial \theta}$. While the Butler-Volmer model predicts a constant value for this parameter, Marcus theory predicts that this value should vary with potential. The variation of the transfer coefficient has been repeatedly studied in order to discriminate between the two different models [27, 29]. This trend is shown in Figure 10.2.

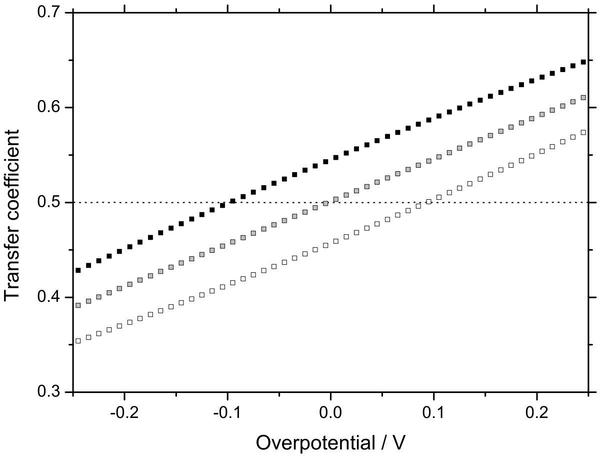

Figure 10.2: Variation of the 'transfer coefficient' with applied potential for the Butler-Volmer model (dotted line, $\alpha = 0.5$) and asymmetric Marcus-Hush model with $\lambda = 1\,\mathrm{eV}$ and $\omega = -0.2\,\mathrm{eV}$ (white squares), $0.0\,\mathrm{eV}$ (grey squares) and $+0.2\,\mathrm{eV}$ (black squares).

An important characteristic of the AMH model is the ability of the transfer coefficient to differ from $\frac{1}{2}$ at the formal potential. This was first observed experimentally by Savéant and Tessier [27] for the electroreduction of nitroalkanes and it is the absence of this feature in the SMH model which has led to the reported inability to fit experimental voltammetry for a number of diffusional systems [6, 13–16]. The variation of transfer coefficient at the formal potential $\left(-\dfrac{\partial \ln k_{\mathrm{red}}}{\partial \theta}\bigg|_{E=E_{\mathrm{f}}^{\ominus}}\right)$ with λ and ω is shown in Figure 10.3. The transfer coefficient deviates positively from 0.5 for $\omega > 0$ and vice versa for $\omega < 0$. Additionally the transfer coefficient varies more strongly with potential for smaller values of reorganisation energy.

Next, we apply the AMH model to the simulation of diffusional cyclic and square wave voltammetry. We consider a system with sluggish electrode kinetics ($k_0 = 10^{-3}\,\mathrm{cm\,s^{-1}}$)

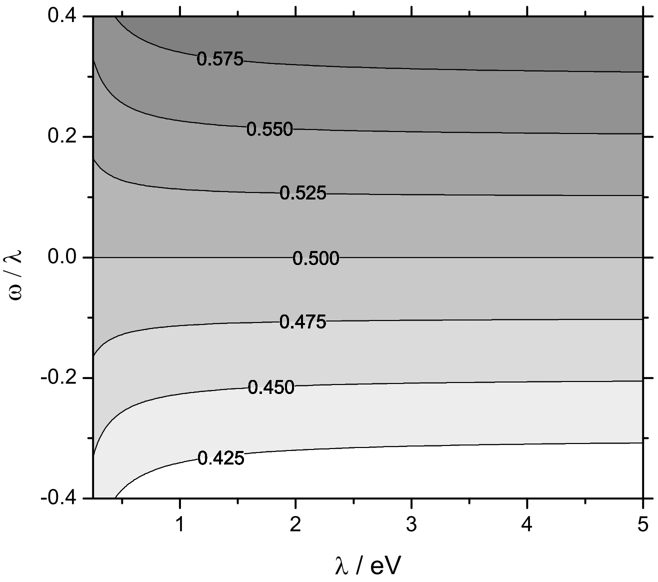

Figure 10.3: Variation of the value of the 'transfer coefficient' at the formal potential with λ and ω.

with a typical reorganisation energy of 2 eV. The simulated voltammetry is shown in Figure 10.4.

We showed in Chapter 5 that the value of the reorganization energy has a similar effect on both the reductive and oxidative peaks – as λ increases, both peaks increase in height and vice versa. By contrast ω affects each peak differently. As ω becomes more positive the reductive peak becomes larger and sharper, while the oxidative peak becomes smaller and broader. The opposite trends are observed when ω becomes more negative. In this manner the parameter ω acts in a (qualitatively) very similar fashion to the transfer coefficient within the Butler-Volmer model.

10.4 Conclusions

We have used the asymmetric formulation of Marcus theory to produce expressions for heterogeneous electron transfer rate constants. This approach leads to a four-parameter model of electrode kinetics: the formal potential, the standard electrochemical rate constant, the reorganisation energy, and a new parameter, ω, which accounts for the differences between the force constants between the oxidised and reduced species.

This new parameter is seen to affect diffusional voltammetry in a manner which is

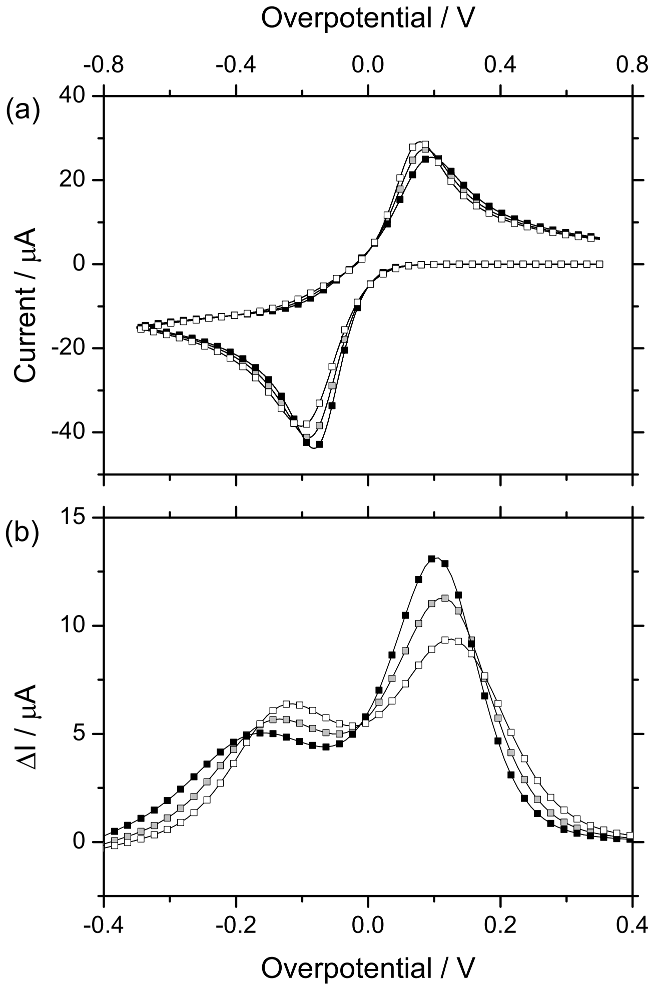

Figure 10.4: Simulated (a) cyclic and (b) reverse scan square wave voltammetry at a hemisphere electrode for a one-electron reduction using the asymmetric Marcus-Hush model. $k_0 = 10^{-3}\,\mathrm{cm\,s^{-1}}$, $\lambda = 2\,\mathrm{eV}$ and $\omega = -0.5\,\mathrm{eV}$ (white squares), $0.0\,\mathrm{eV}$ (grey squares) and $+0.5\,\mathrm{eV}$ (black squares). The values for ω are indicated on the plot. The simulation parameters were $r_\mathrm{e} = 1\,\mathrm{mm}$, $c^* = 1\,\mathrm{mM}$, $D_\mathrm{A} = D_\mathrm{B} = 10^{-5}\,\mathrm{cm^2\,s^{-1}}$ and the scan rate was $1\,\mathrm{V\,s^{-1}}$.

qualitatively similar to that of the transfer coefficient within the Butler-Volmer model. Thus experimental deviations from the symmetric Marcus-Hush model (for which $\omega = 0$), such as asymmetric Tafel plots and transfer coefficients which deviate from 0.5 at the formal potential, can potentially be explained in terms of different inner-shell force constants for the oxidized and reduced species.

In the following chapters we evaluate this new model through application to several experimental systems.

Bibliography

[1] E. Laborda, M. C. Henstridge and R. G. Compton, *J. Electroanal. Chem.* **667** (2012) 48–53.

[2] H. O. Finklea and D. D. Hanshew, *J. Am. Chem. Soc.* **114** (1992) 3173–3181.

[3] R. M. Haddox and H. O. Finklea, *J. Phys. Chem. B* **108** (2004) 1694–1700.

[4] N. Madhiri and H. O. Finklea, *Langmuir* **22** (2006) 10643–10651.

[5] C. E. D. Chidsey, *Science* **251** (1991) 919–922.

[6] M. C. Henstridge, C. Batchelor-McAuley, R. Gusmao and R. G. Compton, *Chem. Phys. Lett.* **517** (2011) 108–112.

[7] R. J. Forster and L. R. Faulkner, *J. Am. Chem. Soc.* **116** (1994) 5444–5452.

[8] H. O. Finklea, L. Liu, M. S. Ravenscroft and S. Punturi, *J. Phys. Chem.* **100** (1996) 18852–18858.

[9] M. S. Ravenscroft and H. O. Finklea, *J. Phys. Chem.* **98** (1994) 3843–3850.

[10] J. N. Richardson, G. K. Rowe, M. T. Carter, L. M. Tender, L. S. Curtin, S. R. Peck and R. W. Murray, *Electrochim. Acta* **40** (1995) 1331–1338.

[11] G. K. Rowe, M. T. Carter, J. N. Richardson and R. W. Murray, *Langmuir* **11** (1995) 1797–1806.

[12] B. R. Kozub, M. C. Henstridge, C. Batchelor-McAuley and R. G. Compton, *ChemPhysChem* **12** (2011) 2806–2815.

[13] E. Laborda, Y. Wang, M. C. Henstridge, F. Martínez-Ortiz, A. Molina and R. G. Compton, *Chem. Phys. Lett.* **512** (2011) 133–137.

[14] D. Suwatchara, M. C. Henstridge, N. V. Rees and R. G. Compton, *J. Phys. Chem. C* **115** (2011) 14876–14882.

[15] D. Suwatchara, N. V. Rees, M. C. Henstridge, E. Laborda and R. G. Compton, *J. Electroanal. Chem.* **665** (2012) 38–44.

[16] Y. Wang, E. Laborda, M. C. Henstridge, F. Martinez-Ortiz, A. Molina and R. G. Compton, *J. Electroanal. Chem.* **668** (2012) 7–12.

[17] V. Mirceski, S. Komorsky-Lovric and M. Lovric, *Square-Wave Voltammetry: Theory and Application*, Monographs in Electrochemistry (Springer, 2007).

[18] H. Matsuda, *Bull. Chem. Soc. Japan* **53** (1980) 3439–3446.

[19] W. S. Go, J. J. O'Dea and J. Osteryoung, *J. Electroanal. Chem* **255** (1988) 21–44.

[20] A. Molina, F. Martnez-Ortiz, E. Laborda and R. G. Compton, *Electrochim. Acta* **55** (2010) 5163–5172.

[21] E. Laborda, E. I. Rogers, F. Martínez-Ortiz, A. Molina and R. G. Compton, *Electroanalysis* **22** (2010) 2784–2793.

[22] E. Laborda, M. C. Henstridge, A. Molina, F. Martínez-Ortiz and R. G. Compton, *J. Electroanal. Chem* **660** (2011) 169–177.

[23] J. T. Hupp and M. J. Weaver, *J. Phys. Chem.* **88** (1984) 6128–6135.

[24] G. A. Orlowski and H.-B. Kraatz, *Electrochim. Acta* **51** (2006) 2934–2937.

[25] G. A. Orlowski, S. Chowdhury and H.-B. Kraatz, *Langmuir* **23** (2007) 12765–12770.

[26] A. L. Eckermann, J. A. Shaw and T. J. Meade, *Langmuir* **26** (2010) 2904–2913.

[27] J. M. Savéant and D. Tessier, *Faraday Discuss. Chem. Soc.* **74** (1982) 57–72.

[28] R. A. Marcus, *J. Chem. Phys.* **43** (1965) 679–701.

[29] S. Fletcher and T. S. Varley, *Phys. Chem. Chem. Phys.* **13** (2011) 5359–5364.

Chapter 11

Evaluation of the asymmetric Marcus-Hush model at a mercury microhemisphere electrode

The newly-developed asymmetric Marcus-Hush model of electrode kinetics is applied to the kinetic study of the one-electron reductions of 2-methyl-2-nitropropane, cyclooctatetraene and europium (III). For each of these redox couples the four-parameter asymmetric Marcus-Hush model is found to enable accurate fitting of the experimental cyclic and square wave voltammetry. The new model is seen to significantly outperform the symmetric Marcus-Hush model in terms of its ability to fit experimental data and performs as well as the Butler-Volmer model. The ratio ω/λ is found to be the important fitting parameter and we highlight the link between this value and the Butler-Volmer transfer coefficient.

This work has been published in the *Journal of Electroanalytical Chemistry* [1]. The experiments were performed by Y. Wang and D. Suwatchara and the simulated square wave voltammetry was produced by E. Laborda.

11.1 Introduction

In previous chapters we have evaluated the so-called symmetric Marcus-Hush model of electrode kinetics through a quantitative comparison between simulation and experiment for several redox systems. In almost all cases this model has performed poorly, particularly when compared with the empirical Butler-Volmer model, with accurate fitting of experimental data not possible even when the reorganisation energy is used purely as a fitting parameter [2–6].

In particular the symmetric Marcus-Hush model has been seen to fail whenever the Butler-Volmer transfer coefficient deviates significantly from $\frac{1}{2}$. In this chapter we apply the *asymmetric* Marcus-Hush model [7] developed in Chapter 10 to the fitting of experimental voltammetry at a mercury microhemisphere electrode. This model removes the assumption that the Gibbs energy curves for the reactants and products have the same curvature, resulting in a significantly more flexible model than its symmetric counterpart.

As test systems we re-examine the one-electron reductions of methyl-2-nitropropane and europium (III) [2] described in Chapter 7, as well as the reduction of cyclooctatetraene [5]. Fitting of the experimental cyclic and square wave voltammetry is attempted using the AMH model, with the results then compared with those obtained previously using the SMH and BV models.

11.2 Theory

The simulations described in this chapter employ the same model as described in Chapter 7 with the exception that the asymmetric Marcus-Hush model is employed instead of its symmetric counterpart.

11.3 Experimental

11.3.1 Chemical reagents

Cyclooctatetraene (COT, Aldrich, 98 %), 2-methyl-2-nitropropane (MeNP, Aldrich, 99 %), europium (III) chloride hexahydrate ($EuCl_3 \cdot 6\,H_2O$, Aldrich, 99.99 %), mercury (I) nitrate dihydrate ($Hg_2(NO_3)_2 \cdot 2\,H_2O$, Aldrich, >97 %), nitric acid (HNO_3, Fisher scientific, 70 %), ferrocene ($Fe(C_5H_5)_2$, Aldrich, 98 %), cobalt (III) sepulchrate trichloride ($[CoSep]Cl_3$, Aldrich, 95 %), potassium nitrate (KNO_3, Aldrich, >99 %), potassium chloride (KCl, Aldrich, >99 %), acetonitrile (MeCN, Fisher Scientific, HPLC grade), N,N-dimethylformamide (DMF, Aldrich, anhydrous grade) and dimethylsulfoxide (DMSO, Alfa Aesar, >99 %) were all used as received without further purification.

Background electrolytes including tetraethylammonium perchlorate (TEAP, Fluka, Puriss grade), tetraethylammonium bromide (TEABr, BDH Chemicals, 98 %), tetrabutylammonium perchlorate (TBAP, Fluka, Puriss grade) and tetrabutylammonium iodide (TBAI, Aldrich, >98 %) were recrystallized from ethanol and dried in a dessicator for 48 h prior to use in order to remove adsorbed moisture and trace electroactive species.

11.3.2 Instrumentation

All electrochemical measurements were performed with a computer-controlled Autolab PGSTAT12 (Metrohm-Autolab BV, Utrecht, Netherlands).

Mercury hemispherical electrodes electrodeposited on platinum discs were used as working electrodes. A silver wire was employed as reference electrode for organic solvents and a saturated calomel electrode (SCE) for aqueous solutions. A platinum foil was used as counter electrode.

Microdisc electrodes of radii 25 and 50 µm were fabricated in-house by sealing Pt wire (Goodfellow Cambridge Ltd, UK) into a soda glass capillary. The platinum disc was polished prior to hemisphere deposition using 1.0, 0.3 and 0.05 µm alumina-water slurry on soft lapping pads (Buehler, Illinois). The disc size was calibrated from chronoamperometry of 1 mM ferrocene solution in acetronitrile supported by 0.1 M TBAP using the Shoup and Szabo expression [8]. A value of the diffusion coefficient for ferrocene of $2.43 \times 10^{-5}\,\mathrm{cm^2\,s^{-1}}$ at 25 °C was assumed according to literature [9].

Mercury hemispheres were electrochemically deposited onto each microdisc by stepping to -0.25 V vs Ag wire in a 5 mM $Hg_2(NO_3)_2$ solution containing 0.1 M KNO_3 and acidified to 0.5 % with HNO_3 [10].

The size of the hemispherical drop was initially controlled by the amount of charge passed, and then confirmed by both optical and electrochemical methods. Thus, visual measurement of the hemispheres was obtained through the use of JVC digital video camera TK-C921EG. In all cases, the mercury droplet was found to adopt the radius of its respective microdisc. The electrochemical characterization of the mercury hemispheres was also carried out through analysis of the limiting current chronoamperogram of an aqueous solution containing 2 mM [CoSep]Cl_3 and 0.1 M KNO_3. The value of the diffusion coefficient of [CoSep]Cl_3 employed for the calculations was $6.3 \times 10^{-6}\,\mathrm{cm^2\,s^{-1}}$ [5].

Redox couple	Medium	D_{reactant} ($\mathrm{cm^2\,s^{-1}}$)	D_{product} ($\mathrm{cm^2\,s^{-1}}$)
MeNP / $\mathrm{MeNP^{\bullet-}}$	0.1 M TBAP, MeCN	2.7×10^{-5}	2.7×10^{-5}
COT / $\mathrm{COT^{\bullet-}}$	0.1 M TEABr, DMSO	7.4×10^{-6}	6.5×10^{-6}
$\mathrm{Eu^{3+}}$ / $\mathrm{Eu^{2+}}$	0.4 M KCl, H_2O	6.5×10^{-6}	9.0×10^{-6}

Table 11.1: Diffusion coefficients for the three redox couples studied.

11.3.3 Experiments

The specific conditions for cyclic voltammetry (CV) and square wave voltammetry (SWV) experiments are given in each figure.

In all cases, the working solution was deoxygenated using N_2 (BOC Gases) for at least 20 min before each experiment and a positive pressure of N_2 was maintained throughout. Measurements were carried out at 25 ± 0.2 °C with stringent thermal control of the electrochemical cell through the use of an air heater-controller system.

The diffusion coefficients of the electroactive species were determined separately via double potential step chronoamperometry [11] in the case of MeNP and Eu(III). In the case of COT, the use of double step chronoamperometry was not feasible due to interference by a second reduction wave [5]. The diffusion coefficient of the oxidized species (COT) was extracted via single pulse chronoamperograms and that of the reduced species (radical anion $\mathrm{COT^{\bullet-}}$) was determined from the fitting of the cyclic voltammograms. The results obtained are included in Table 11.1.

The occurrence of ohmic drop or migration effects are not considered following simulation [12] of the influence of the uncompensated resistance for the conditions of the working solutions.

11.4 Results

Cyclic and square wave voltammetry were performed at a range of scan rates and frequencies for MeNP in acetonitrile, COT in DMSO and Eu(III) in water at a mercury microhemisphere electrode. Fitting of this voltammetry was then attempted using the AMH model with the quality of fit being measured using a mean scaled absolute deviation (MSAD). Typical voltammetry is shown in Figures 11.1, 11.2 and 11.3 along with the best fits achieved using the AMH and BV models. The best-fit parameters for both models are given in Table 11.2.

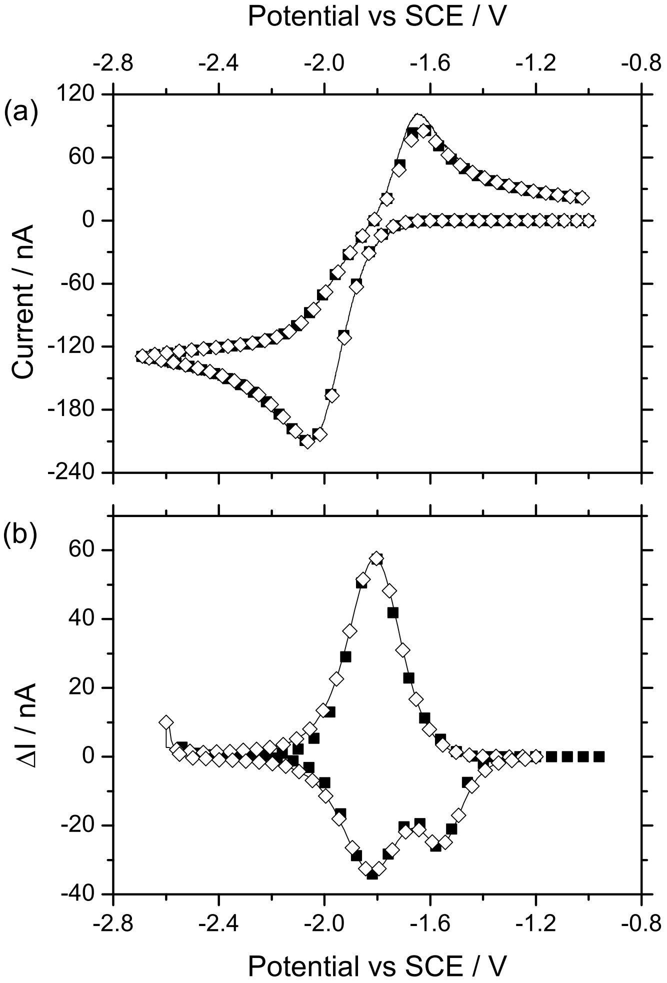

Figure 11.1: Experimental voltammetry for MeNP reduction (solid line) with best fits using Butler-Volmer (black squares) and asymmetric Marcus-Hush kinetics (white diamonds). (a) Cyclic voltammetry recorded at $5\,\mathrm{V\,s^{-1}}$ and (b) square wave voltammetry recorded at 100 Hz, $E_{\mathrm{SW}} = 25\,\mathrm{mV}$ and $E_{\mathrm{S}} = 10\,\mathrm{mV}$.

In all cases the AMH model enables excellent fitting of both cyclic and square wave voltammetry across the entire range of scan rates and frequencies using a consistent set of kinetic parameters. The AMH model is also seen to produce voltammetry which is almost indistinguishable from the BV model, consequently the MSAD values (given in Table 11.2) are also very similar between the two models. The AMH approach, however, carries the additional benefit of allowing the kinetic parameters to be rationalised in terms

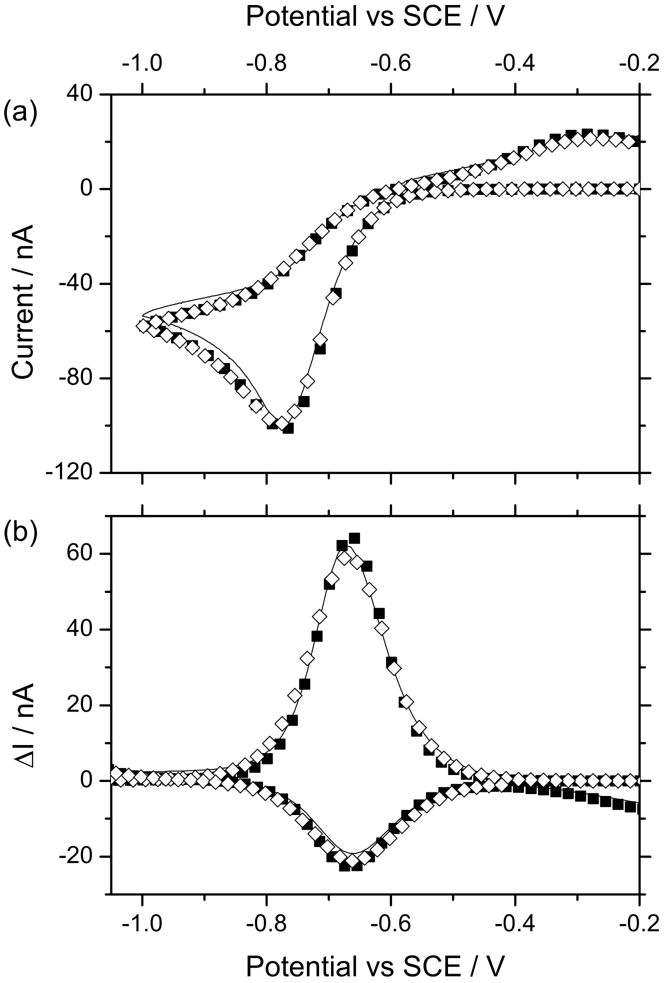

Figure 11.2: Experimental voltammetry for Eu reduction (solid line) with best fits using Butler-Volmer (black squares) and asymmetric Marcus-Hush kinetics (white diamonds). (a) Cyclic voltammetry recorded at $1\,\mathrm{V\,s^{-1}}$ and (b) square wave voltammetry recorded at $100\,\mathrm{Hz}$, $E_{\mathrm{SW}} = 25\,\mathrm{mV}$ and $E_{\mathrm{S}} = 10\,\mathrm{mV}$.

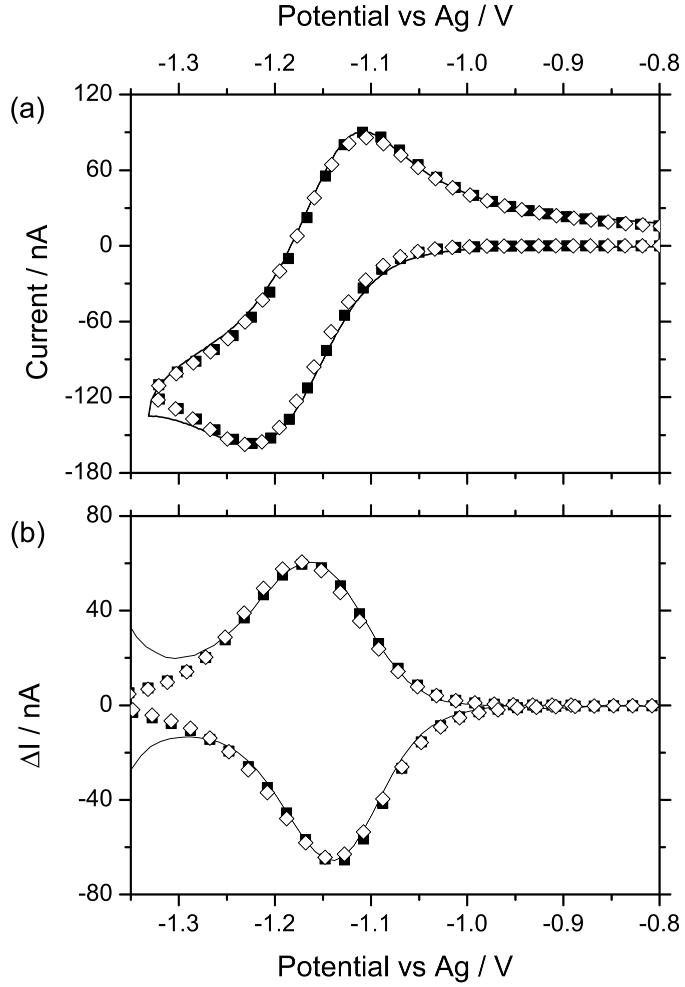

Figure 11.3: Experimental voltammetry for COT reduction (solid line) with best fits using Butler-Volmer (black squares) and asymmetric Marcus-Hush kinetics (white diamonds). (a) Cyclic voltammetry recorded at $1\,\mathrm{V\,s^{-1}}$ and (b) square wave voltammetry recorded at $100\,\mathrm{Hz}$, $E_{\mathrm{SW}} = 15\,\mathrm{mV}$ and $E_{\mathrm{S}} = 10\,\mathrm{mV}$.

Redox couple	Kinetic model	Parameters	% MSAD	
			CV	SWV
MeNP / MeNP$^{\cdot-}$	BV	$k_0 = (3.0 \pm 0.2)\times\ 10^{-3}\,\mathrm{cm\,s^{-1}}$ $\alpha = 0.38 \pm 0.01$	4 ± 2	10 ± 1
	AMH	$k_0 = (3.0 \pm 0.2)\times\ 10^{-3}\,\mathrm{cm\,s^{-1}}$ $\omega/\lambda = -0.31 \pm 0.04$	3 ± 1	5 ± 1
COT / COT$^{\cdot-}$	BV	$k_0 = (1.2 \pm 0.2)\times\ 10^{-2}\,\mathrm{cm\,s^{-1}}$ $\alpha = 0.38 \pm 0.01$	7 ± 2	4 ± 1
	AMH	$k_0 = (1.1 \pm 0.3)\times\ 10^{-2}\,\mathrm{cm\,s^{-1}}$ $\omega/\lambda = -0.22 \pm 0.07$	7 ± 2	4 ± 1
$\mathrm{Eu^{3+}}$ / $\mathrm{Eu^{2+}}$	BV	$k_0 = (3.5 \pm 0.7)\times\ 10^{-4}\,\mathrm{cm\,s^{-1}}$ $\alpha = 0.66 \pm 0.02$	9 ± 2	12 ± 4
	AMH	$k_0 = (3.5 \pm 0.5)\times\ 10^{-4}\,\mathrm{cm\,s^{-1}}$ $\omega/\lambda = +0.55 \pm 0.04$	8 ± 3	10 ± 4

Table 11.2: Best fit parameters for the three redox couples studied.

of the microscopic properties of the system, as will be discussed below.

The ability of the AMH model to accurately fit experimental data is in stark contrast to its symmetric counterpart, whose inability to fit these particular systems was demonstrated in Chapter 7. For the SMH model the best fits generally featured a reasonable fit of the forward peak, but significant deviation from experiment for the back peak. This behaviour is not observed for the asymmetric model and the improved performance must be attributed to the extra flexibility afforded by the additional parameter ω, which characterises the asymmetry of the system.

While the AMH model is formally a four parameter model with $\{E_{\mathrm{f}}^{\ominus}, k_0, \lambda, \omega\}$, in the course of fitting the voltammetry it became clear that the simulated voltammetry was fairly insensitive to the exact values of λ and ω, rather the value of the ratio ω/λ is the important variable in determining the 'shape' of the voltammetry. In this way the ratio ω/λ is seen to act in a similar fashion within the AMH model as does the transfer coefficient within the BV model.

Indeed the rate constants for the SMH model, which may be thought of as a special case of the AMH model with $\omega = 0$, have been shown to tend towards those given by the BV model for $\alpha = \frac{1}{2}$ in the limit $\lambda \to \infty$ [13]. Analysis of the rate constants given by the AMH model (shown in Appendix A) yields a similar relationship: in the limit $\lambda \to \infty$ the rate constants tend to those given by the Butler-Volmer model with transfer coefficient given by:

$$\alpha = \frac{1}{2} + \frac{1}{4}\frac{\omega}{\lambda} \tag{11.1}$$

This relationship is demonstrated in Figure 11.4, which shows rate constants for the BV model with $\alpha = 0.6$ and for the AMH model with $\omega/\lambda = +0.4$ for a range of reorganisation energies. As λ increases the AMH rate constants are seen to converge on the BV limit as given by Equation (11.1). As λ decreases the rate constants deviate from the BV limit a lower overpotentials, but even for small values of reorganisation energy the two models yield almost indistinguishable rate constants at small overpotentials.

Equation (11.1) is exact only in the limit $\lambda \to \infty$, it is only approximate for realistic values of reorganisation energy. A more general relationship may be applied at the formal potential for any value of reorganisation energy:

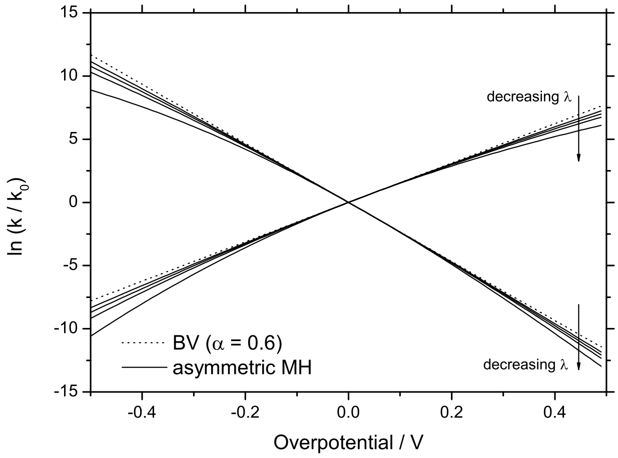

Figure 11.4: Demonstration of the relationship between the Butler-Volmer (dashed line) and asymmetric Marcus-Hush models given in Equation (11.1) for different values of reorganisation energy.

$$\alpha(E_\mathrm{f}^\ominus) = \frac{1}{2} + \gamma\frac{\omega}{\lambda} \tag{11.2}$$

where γ has been calculated numerically and is shown as a function of λ in Figure 11.5. Empirical fitting of this curve yields:

$$\gamma = \frac{1}{4} - \frac{0.0325}{\lambda + 0.0861} \tag{11.3}$$

which is accurate to within 0.1 % for $\lambda > 0.5\,\mathrm{eV}$. For a typical solution phase reorganisation energy of 2 eV this gives $\gamma = 0.234$.

11.5 Discussion

The relationship between the Butler-Volmer and asymmetric Marcus-Hush models given in Equation (11.1) is potentially of great significance since it permits an approximate physical interpretation for the great number of experimental systems for which the transfer coefficient is already known. In the same way, it justifies the use of a simpler Butler-Volmer like analysis of electrode kinetics, complemented with the physical insights derived from the asymmetric Marcus-Hush model.

Further, from the definition of ω (Chapter 10), the ratio ω/λ is seen to be directly

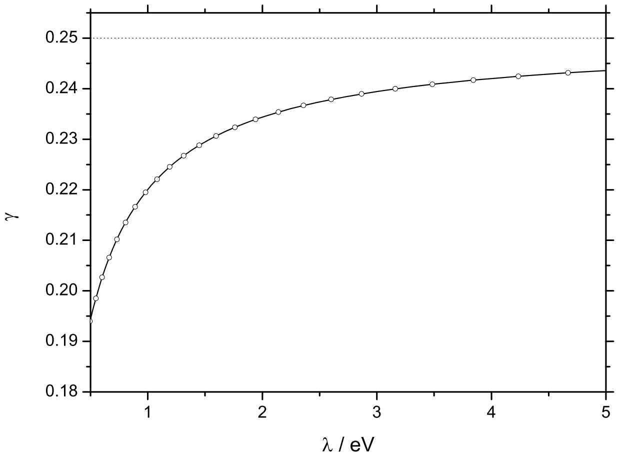

Figure 11.5: Variation of the parametetr γ from Equation (11.2). Measured values (white circles) have been fitted empirically (solid line).

related to the differences between the force constants through $\langle l_s \rangle$. Thus, a positive ω/λ value indicates $f_s^{\text{ox}} > f_s^{\text{red}}$ and hence a tighter Gibbs energy curve for the oxidised species, the opposite is the case for negative ω/λ. Clearly, the greater the absolute value of ω/λ, the greater the differences in the force constants.

Applying this interpretation of ω/λ to the experimental results, we observe that negative values are obtained for the reductions of COT and MeNP. In both cases the oxidised species is neutral and the reduced species is a radical anion. One would therefore expect the reduced species to interact more strongly with the solvent and consequently the Gibbs energy curve is tighter (*i.e.* has a larger force constant) for the reduced species [14]. By contrast, for the reduction of Eu(III) ω/λ is positive which can be understood taking into account that the oxidised species (Eu^{3+}) carries a greater charge than the reduced species (Eu^{2+}).

11.6 Conclusions

The asymmetric Marcus-Hush model has been applied to the quantitative study of three one-electron reductions at a mercury microhemisphere electrode: 2-methyl-2-nitropropane, cyclooctatetraene and europium (III). In each case the fitting achieved was excellent and proved almost indistinguishable from that previously obtained using the Butler-Volmer model. Importantly the asymmetric model performed significantly better than the *symmetric* Marcus-Hush model, which has previously been shown to perform poorly for these systems.

In the course of fitting it was observed that the important variable in determining the 'shape' of the simulated voltammogram, and hence the quality of fit, is in fact the ratio ω/λ, rather than the individual values of the two parameters. In this regard the ratio ω/λ acts in a similar fashion to the transfer coefficient within the Butler-Volmer model, indeed a simple relationship between these two parameters is given.

This relationship permits existing kinetic data parameterised in terms of a transfer coefficient to be reinterpreted in terms of the microscopic properties of the system. Indeed, continued use of the Butler-Volmer model for the analysis of diffusional voltammetry is recommended due to its great simplicity and ubiquity, with any results easily recast in terms of the asymmetric Marcus-Hush model subsequently.

Further, for each system the sign of the fitted ω/λ value proved consistent with the underlying physical model in which ω is an indication of the differences between the force constants of the oxidised and reduced species. The reductions of MeNP and COT, for which the reduced species is more highly charged and hence ought to interact more strongly with the solvent, yielded negative values of ω/λ and the reduction of Eu(III), for which the oxidised species is more highly charged, yielded a positive value.

Bibliography

[1] M. C. Henstridge, E. Laborda, Y. Wang, D. Suwatchara, N. Rees, A. Molina, F. Martínez-Ortiz and R. G. Compton, *J. Electroanal. Chem.* **672** (2012) 45–52.

[2] M. C. Henstridge, Y. Wang, J. G. Limon-Petersen, E. Laborda and R. G. Compton, *Chem. Phys. Lett.* **517** (2011) 29–35.

[3] E. Laborda, Y. Wang, M. C. Henstridge, F. Martínez-Ortiz, A. Molina and R. G. Compton, *Chem. Phys. Lett.* **512** (2011) 133–137.

[4] D. Suwatchara, M. C. Henstridge, N. V. Rees and R. G. Compton, *J. Phys. Chem. C* **115** (2011) 14876–14882.

[5] D. Suwatchara, N. V. Rees, M. C. Henstridge, E. Laborda and R. G. Compton, *J. Electroanal. Chem.* **665** (2012) 38–44.

[6] Y. Wang, E. Laborda, M. C. Henstridge, F. Martinez-Ortiz, A. Molina and R. G. Compton, *J. Electroanal. Chem.* **668** (2012) 7–12.

[7] E. Laborda, M. C. Henstridge and R. G. Compton, *J. Electroanal. Chem.* **667** (2012) 48–53.

[8] D. Shoup and A. Szabo, *J. Electroanal. Chem.* **140** (1982) 237–245.

[9] Y. Wang, E. I. Rogers and R. G. Compton, *J. Electroanal. Chem.* **648** (2010) 15–19.

[10] J. Mauzeroll, E. A. Hueske and A. J. Bard, *Anal. Chem.* **75** (2003) 3880–3889.

[11] R. G. Compton and C. E. Banks, *Understanding voltammetry* (Imperial College Press, London, 2010), 2nd edition.

[12] E. J. F. Dickinson, J. G. Limon-Petersen, N. V. Rees and R. G. Compton, *J. Phys. Chem. C* **113** (2009) 11157–11171.

[13] S. W. Feldberg, *Anal. Chem.* **82** (2010) 5176–5183.

[14] J. M. Savéant and D. Tessier, *Faraday Discuss. Chem. Soc.* **74** (1982) 57–72.

Chapter 12

Asymmetric Marcus-Hush Model of Electron Transfer Kinetics: Application to the voltammetry of surface-bound redox systems

The asymmetric Marcus-Hush model is applied to the study of the voltammetric response of electroactive monolayers. We employ numerical simulations to examine several experimental features for both cyclic and square wave voltammetry, as well as Tafel plots, using both symmetric and asymmetric Marcus-Hush models and the phenomenological Butler-Volmer model.

The asymmetric Marcus-Hush model is seen to outperform the other models in terms of the quantitative description of the full voltammetric waveshape and is able to reproduce all of the experimental trends examined, as such its use for the analysis of surface-bound redox couples is highly recommended.

This work has been published in the *Journal of Electroanalytical Chemistry* [1]. The simulations for square wave voltammetry were performed by E. Laborda.

12.1 Introduction

The symmetric Marcus-Hush model has been particularly successful in modelling surface-bound redox couples due to its ability to reproduce the curved Tafel plots which have often been observed experimentally [2–4].

There are, however, documented examples of experimental systems which show deviations from the symmetric Marcus-Hush model. These systems exhibit curved Tafel plots whose anodic and cathodic branches have differing slopes in the vicinity of the formal potential [5–13]. This cannot be accounted for either by the symmetric Marcus-Hush model, for which a Tafel plot is always symmetrical about the formal potential, or by the Butler-Volmer model which cannot reproduce the curvature of such plots. Some researchers have treated the anodic and cathodic branches entirely separately using the symmetric Marcus-Hush model with two different values for the standard rate constant and reorganisation energy [8–10, 13], but this approach is not consistent with the Nernst equation.

A "through-space" tunneling model has been proposed as a possible justification for the asymmetric Tafel plots observed for surface-bound systems [14]. This introduces an additional potential-dependent term which quantifies the probability of an electron tunneling through an energy barrier. The inclusion of this term permits asymmetric Tafel plots, but this method always yields a greater slope for the cathodic branch than for the anodic. However there have been systems reported, both surface-bound and solution-phase, for which the opposite trend is observed [9, 10, 15].

In this chapter we consider the application of the asymmetric Marcus-Hush theory to the study of surface-bound redox couples. The qualitative effects of the reorganisation energy (λ) and the asymmetry parameter (ω/λ) on Tafel plots and both cyclic and square wave voltammetries are examined, as well as their effect on observable voltammetric features such as peak potential and peak current.

12.2 Theory

The simulations presented here used the same model described in Chapter 6. For all simulations the electrode area is $0.1\,\mathrm{cm}^2$, the surface coverage is $10^{-10}\,\mathrm{mol\,cm}^{-2}$. Unless otherwise stated, we use values for the kinetic parameters which are typical for surface-bound systems: $k_0 = 10\,\mathrm{s}^{-1}$, $\lambda = 1\,\mathrm{eV}$.

12.3 Results

12.3.1 Asymmetric Tafel plots

Among the most distinctive features of the Marcus-Hush model [2, 16–18], both symmetric and asymmetric, is its prediction of curved Tafel plots compared to the linear plots predicted by the Butler-Volmer model. While the latter predicts rate constants which increase exponentially with overpotantial *ad infinitum*, the Marcus-Hush model predicts that rate constants begin to level off at large overpotential and tend towards limiting values. Early work by Chidsey [2] using ferrocene tethered to a gold electrode yielded a markedly curved, yet symmetric Tafel plot.

However, there have since been several reported instances of experimental systems [5, 6, 8–13] for which the anodic and cathodic branches are curved, but not symmetric. Neither the Butler-Volmer nor symmetric Marcus-Hush model can account for both of these observations simultaneously: the symmetric Marcus-Hush model produces curved Tafel plots, but it cannot account for the any asymmetry between anodic and cathodic branches. The opposite is true of the Butler-Volmer model, for which the transfer coefficient controls the degree of asymmetry between the anodic and cathodic regions, but the resulting Tafel plots are strictly linear. The asymmetric Marcus-Hush model, on the other hand, is able to reproduce both of these experimentally observed features simultaneously, as shown in Figure 12.1.

The effect of the reorganisation energy on the potential dependence of rate constants has been well documented in the past [2, 17, 18]. For very large values of λ the Tafel plot remains almost linear, however as λ decreases the overpotential at which the rate constants begin to plateau decreases. The effect of the asymmetry parameter on Tafel plots is shown in Figure 12.1. The curvature of the plots is marked, especially when compared with the corresponding Butler-Volmer data, as the rate constants begin to level off at large overpotentials. While the symmetric Marcus-Hush model ($\omega/\lambda = 0$) yields symmetric anodic and cathodic branches, the asymmetric model ($\omega/\lambda \neq 0$) does not. As the asymmetry parameter increases in magnitude, so does the difference between the anodic and cathodic rate constants.

We have tested the asymmetric model against experimental data published by Haddox

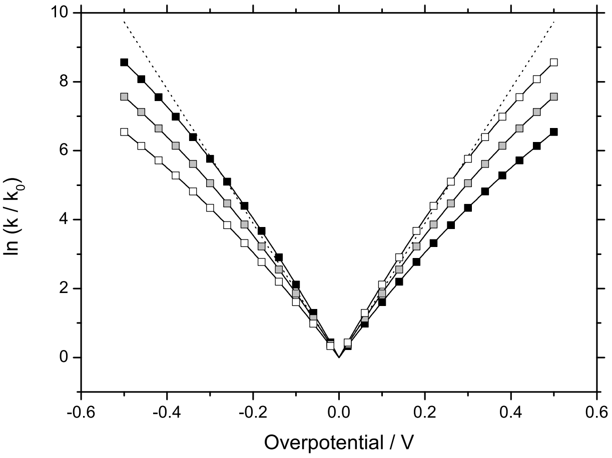

Figure 12.1: Simulated Tafel plots for a redox couple obeying asymmetric Marcus-Hush kinetics. In each case $\lambda = 1\,\mathrm{eV}$, $\omega/\lambda = +0.3$ (black), -0.3 (white) and 0 (grey). The dotted line shows the corresponding data calculated using the Butler-Volmer model (with $\alpha = 0.5$) for comparison.

and Finklea [9]. They studied the proton-coupled oxidation of a surface-bound osmium complex at a SAM-modified gold electrode. While the kinetics of this redox process will be a function of the local proton concentration, at very high and very low pH this value ought to remain approximately constant during the reaction and the electron transfer kinetics will not be obscured. Further the monolayer is assumed kinetically homogeneous.

Figure 12.2 shows the experimental data given in this paper for the reaction at pH 0.8 (inferred from Figure 6 in Reference [9]). Both anodic and cathodic branches show definite curvature and the asymmetry between the two halves is clear. Haddox and Finklea fitted the anodic and cathodic branches independently, yielding two different values of both reorganisation energy and standard rate constant (anodic $\lambda = 1.4\,\mathrm{eV}$, $k_0 = 24\,\mathrm{s}^{-1}$; cathodic $\lambda = 0.6\,\mathrm{eV}$, $k_0 = 21\,\mathrm{s}^{-1}$). It should be noted that for this system the anodic Tafel slope is appreciably greater than the cathodic slope in contrast to the predictions of the "through-space" tunneling model. Independent fitting of the anodic and cathodic branches has been widely employed [8–10, 13] and achieves a satisfactory fit, however this approach cannot be reconciled with the Nernst equation (i.e. for a given potential θ the relation $k_{\mathrm{ox}}/k_{\mathrm{red}} = \exp(\theta)$ is not satisfied).

We therefore attempted to fit the same experimental data with a single set of parameters using the asymmetric Marcus-Hush model. This was achieved via least-squares fitting

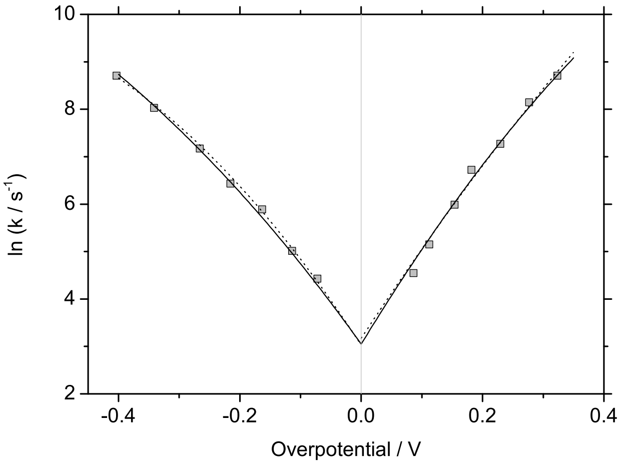

Figure 12.2: Plot of rate constant *vs* overpotential for a surface-bound Osmium aquo complex. Experimental data (squares) are taken from Reference [9], as is the theoretical fit using symmetric MH theory (dotted) which uses two values of k_0 and λ. The theoretical fit using asymmetric MH theory (solid) was calculated using $k_0 = 21\,\mathrm{s}^{-1}$, $\lambda = 0.85\,\mathrm{eV}$ and ω/λ = -0.18.

using an exhaustive search over a wide range of k_0, λ and ω/λ. This process yielded an excellent fit for both anodic and cathodic branches using a single set of kinetic parameters ($k_0 = 21\,\mathrm{s}^{-1}$, $\lambda = 0.85\,\mathrm{eV}$ and ω/λ = -0.18) as can be seen in Figure 12.2.

12.3.2 Voltammetric peak current

When studying surface-bound redox couples using cyclic voltammetry (CV), assuming irreversible Butler-Volmer kinetics, the peak current is predicted to scale linearly with scan rate [19]. If Marcus-Hush kinetics operate, however, plotting peak current against scan rate yields a curve with the peak current smaller than expected from classical theory at high scan rates [20–22], as has been demonstrated experimentally [8–10, 23]. As an illustrative example the forward (oxidative) peak current for Haddox and Finklea's Osmium system [9] discussed in the previous section is predicted to be only approximately 70 % that expected from the classical Butler-Volmer treatment for a scan rate of $1\,\mathrm{kV\,s}^{-1}$.

This feature is common to both symmetric and asymmetric formulations of the Marcus-Hush model as illustrated in Figure 12.3, which shows the theoretical scan rate dependence of both oxidative and reductive peak currents for a system with $k_0 = 10\,\mathrm{s}^{-1}$ and λ = 1 eV for a range of ω/λ values. The deviations from linearity are marked: all values of ω/λ yield a curve; including $\omega/\lambda = 0$, which corresponds to the symmetric Marcus-Hush model. Positive values of this parameter yield larger reductive peak currents than the symmetric model and smaller oxidative peaks, negative values yield smaller reductive peak currents.

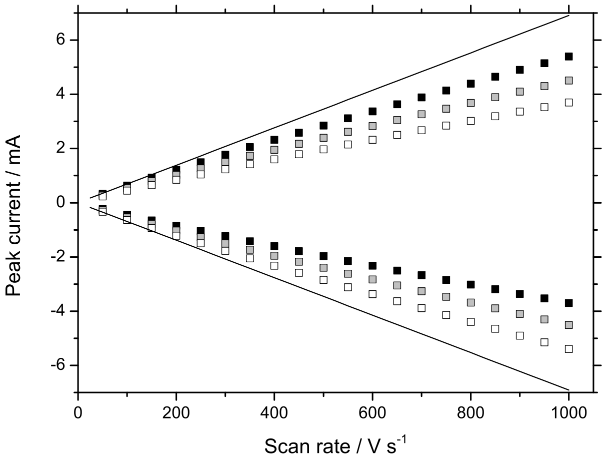

Figure 12.3: Variation of CV peak current with scan rate for a surface-bound redox couple, $\lambda = 1\,\text{eV}$ and $\omega/\lambda = +0.3$ (black), -0.3 (white) and 0 (grey). The linear relationship expected from Butler-Volmer kinetics is shown for comparison.

The Butler-Volmer model predicts an analogous trend for square wave voltammetry (SWV): for a totally irreversible system the peak current is proportional to the pulse frequency. The variation of the peak current with heterogeneous rate constant is plotted in Figures 12.4 and 12.5 for a reduction for both Butler-Volmer and symmetric Marcus-Hush kinetic models. In the reversible and quasireversible regions (in which the pulse frequency, f, satisfies $k_0/f > 0.1$) only small differences are observed between the models since the peaks occur at small overpotentials where the values for the rate constants are very similar. Both models predict the so-called 'quasireversible maximum' as shown in Figure 12.4 [24, 25] at *ca.* $k_0/f = 1$. When considering more irreversible systems, however, the differences between the models become more apparent. While peak current scales linearly with frequency for the Butler-Volmer model, at high frequencies the peak height is smaller than predicted by classical theory (Figure 12.5). The trends regarding the value of ω/λ are the same as those observed for CV.

For both techniques it is possible to use the ratio of cathodic and anodic peak currents ($I_{\text{p,c}}/I_{\text{p,a}}$) to estimate the value of ω/λ. Figures 12.6 and 12.7 show surfaces relating the

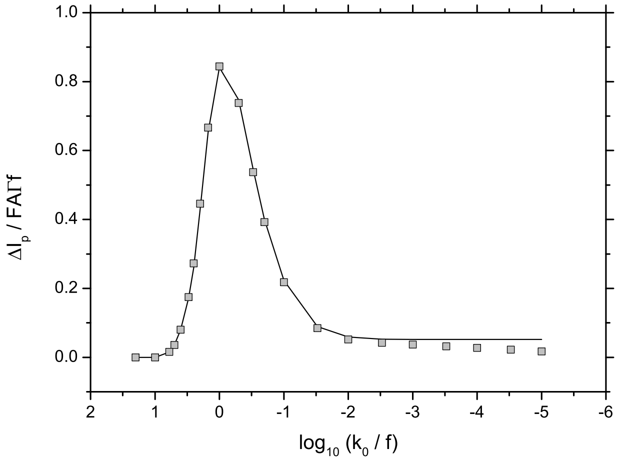

Figure 12.4: Variation of peak current with the dimensionless heterogeneous rate constant (k_0/f), displaying the ‘quasireversible maximum’. Frequency = 100 Hz, pulse amplitude = 50 mV, step potential = 5 mV.

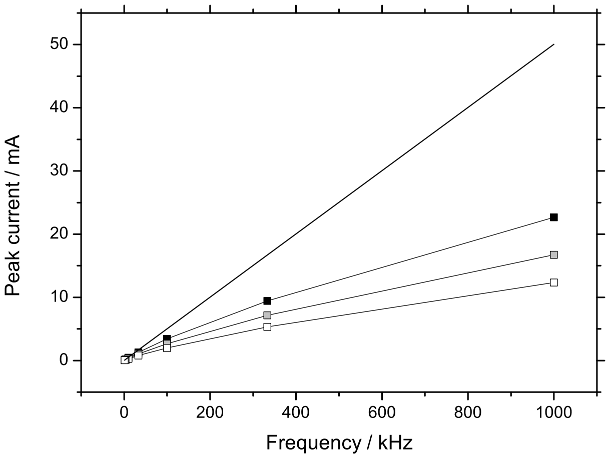

Figure 12.5: Variation of SWV peak current with frequency for a surface-bound redox couple, $\lambda = 1\,\mathrm{eV}$ and $\omega/\lambda = +0.3$ (black), -0.3 (white) and 0 (grey). The linear relationship expected from Butler-Volmer kinetics is shown for comparison. Pulse amplitude = 50 mV and step potential = 5 mV.

ratio of peak currents to both λ and ω/λ. It is clear that the ratio of peak currents is fairly insensitive to the exact value of the reorganisation energy and thus these surfaces may serve to extract an approximate value of ω/λ. The surfaces are calculated for $RTk_0/Fv = 0.01$ and $k_0/f = 0.01$ respectively and are general to all systems as either the scan rate or pulse frequency may be adjusted to satisfy these relationships.

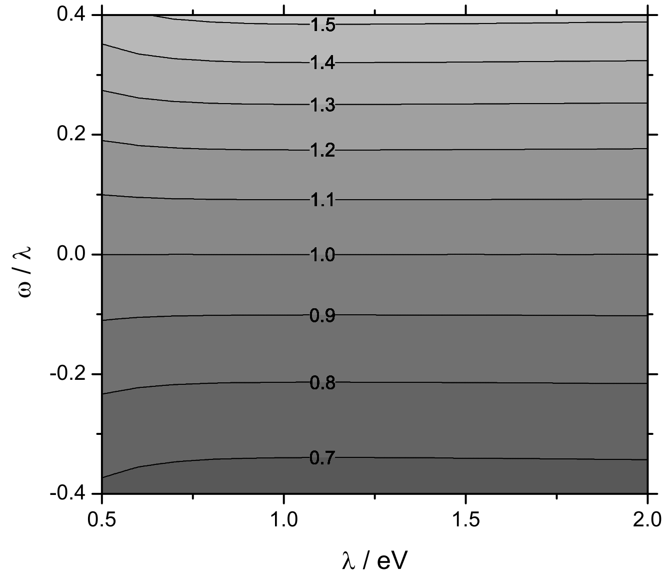

Figure 12.6: The ratio between of cathodic and anodic peak currents as a function of λ and ω/λ for cyclic voltammetry, $RTk_0/Fv = 0.01$.

Peak split

A further characteristic of electroactive monolayers, unique to SWV, is the splitting of the peak for fast electron transfers when large pulse amplitudes are employed [25]. The separation between the two resulting peaks increases with increasing pulse amplitude. As can be seen in Figure 12.8, this behaviour is successfully reproduced by both Butler-Volmer and Marcus-Hush kinetic models. This phenomenon has been observed for several redox systems by employing the appropriate frequency value and both have been used to characterise the kinetics of the electron transfer [25].

While the frequency of the quasireversible maximum permits estimation of the k_0 value [25], the ratio of the two resulting peak currents is characteristic of the transfer coefficient as can be inferred from Figure 12.8. Within the Butler-Volmer model the peak

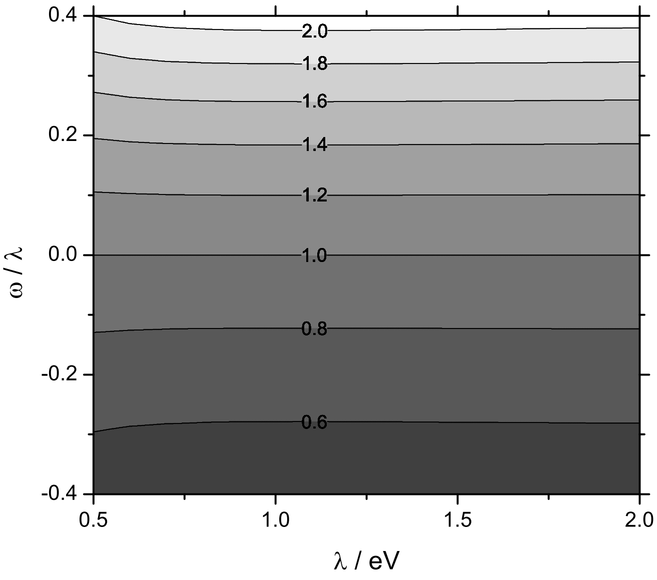

Figure 12.7: The ratio between of cathodic and anodic peak currents as a function of λ and ω/λ for cyclic square wave voltammetry, $k_0/f = 0.01$. Pulse amplitude $= 25\,\mathrm{mV}$, step potential $= 10\,\mathrm{mV}$.

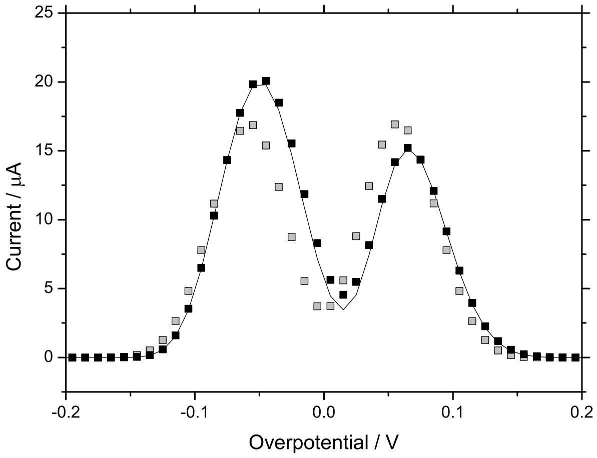

Figure 12.8: Split of the SWV peak for fast electron transfers at large pulse amplitudes predicted by the Butler-Volmer (solid line, $\alpha = 0.6$) and asymmetric Marcus-Hush (square points, $\lambda = 1\,\mathrm{eV}$) for $\omega/\lambda = 0$ (grey) and $+0.45$ (black). In both cases $f = 3.33\,\mathrm{Hz}$, step potential $= 10\,\mathrm{mV}$ and pulse amplitude $= 75\,\mathrm{mV}$.

currents are predicted to be equal for $\alpha = 0.5$, the anodic peak is larger for $\alpha < 0.5$ and the cathodic peak is larger for $\alpha > 0.5$. Similarly, this ratio relates to the asymmetry parameter in the Marcus-Hush model: a larger cathodic peak indicates a positive ω/λ value (i.e. the force constants of the oxidized species are greater on average than those of the reduced species). The opposite applies when the anodic peak is larger. Thus studying the symmetry of the two peaks under suitable conditions enables simple detection and quantification of asymmetry effects.

12.3.3 Voltammetric peak potential

Due to the difficulty in correctly subtracting non-Faradaic background current from experimental cyclic voltammetry, the potentials of the CV peaks have sometimes been preferred for extracting quantitative data [20]. According to the work of Laviron, for a kinetically irreversible system (with peak splitting $\geq 200\,\text{mV}$) the peak potential should scale linearly with the logarithm of scan rate [19]. Under Marcus-Hush kinetics, however, peak potential deviates from this relationship – increasing at a greater rate than log scan rate, as shown in Figure 12.9. Symmetric Marcus-Hush predicts that oxidative and reductive peaks should occur equally separated from the formal potential, whereas within the asymmetric model the two peaks may occur at different overpotentials. This feature of the asymmetric model, specifically, has been observed experimentally in the Osmium system described in reference [9].

As is the case for peak current, there is an analogous theoretical relationship for SWV assuming Butler-Volmer kinetics: peak potential scales linearly with log frequency [24]. The Marcus-Hush model, however, does not follow this prediction, as shown in Figure 12.10.

12.3.4 Voltammetric waveshape

We demonstrated a relationship between the Butler-Volmer transfer coefficient (α) and the asymmetry parameter ω/λ [15] in Chapter 11. Figures 12.11 and 12.13 show cyclic and square wave voltammograms respectively for a range of ω/λ values. The results are indeed qualitatively akin to those expected from varying α: when $\omega/\lambda = 0$ (roughly equivalent to $\alpha = 0.5$) the forward and back peaks are the same height and occur at the

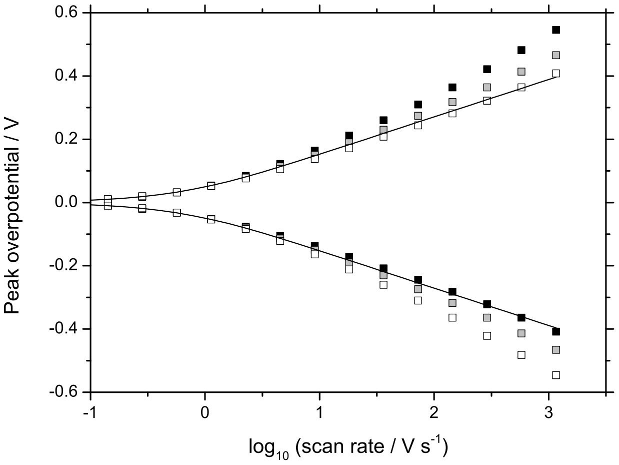

Figure 12.9: Plot of peak potential *vs* log scan rate for a surface-bound redox couple using CV, $\lambda = 1\,\text{eV}$ and $\omega/\lambda = +0.3$ (black), -0.3 (white) and 0 (grey). The relationship expected from Butler-Volmer kinetics is (solid line) shown for comparison.

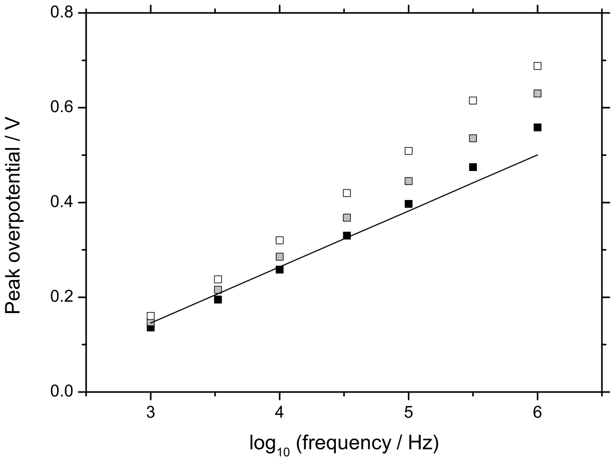

Figure 12.10: Plot of peak potential *vs* log frequency for a surface-bound redox couple using SWV, $\lambda = 1\,\text{eV}$ and $\omega/\lambda = +0.25$ (black), -0.25 (white) and 0 (grey). The relationship expected from Butler-Volmer kinetics (solid line) is shown for comparison. Pulse amplitude = 25 mV and step potential = 10 mV.

same magnitude of overpotential. If ω/λ deviates from 0 then one peak becomes sharper and taller, occurring at lower overpotential and the other becomes broader, shorter and moves away from the formal potential.

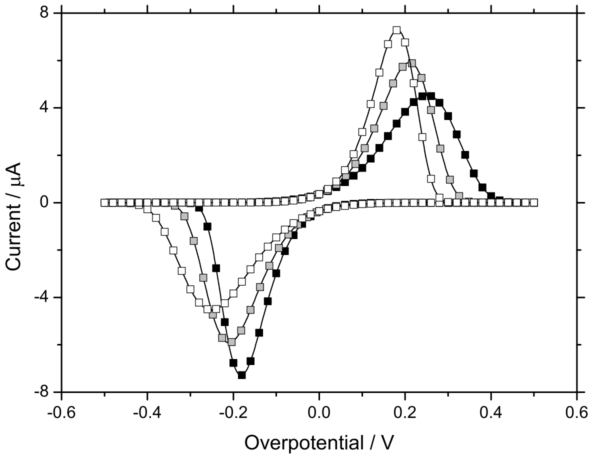

Figure 12.11: Simulated cyclic voltammetry for a surface-bound redox couple obeying asymmetric Marcus-Hush kinetics with $RTk_0/Fv = 0.01$ ($k_0 = 0.389\,\mathrm{s}^{-1}$ and $v = 1\,\mathrm{V\,s}^{-1}$), $\lambda = 1\,\mathrm{eV}$ and $\omega/\lambda = +0.45$ (black), -0.45 (white) and 0 (grey).

When comparing the asymmetric Marcus-Hush model with the Butler-Volmer model quantitatively, however, the equivalence no longer holds for the smaller values of reorganisation energy (~1 eV) typical for surface-bound systems. Figures 12.12 and 12.14 show voltammetry simulated for both cyclic and square wave voltammetry using asymmetric Marcus-Hush kinetics ($\lambda = 1\,\mathrm{eV}$, $\omega/\lambda = +0.45$, $RTk_0/Fv = 0.01$ and $k_0/f = 0.01$ respectively) and the closest fits of the reductive peak possible using the Butler-Volmer model (while keeping k_0 fixed). In both cases it is not possible to simultaneously fit both forward and back peaks, even if $E_\mathrm{f}^\ominus$ and k_0 are treated as variable. While the two models proved almost indistinguishable for typical solution-phase systems [15], this is evidently not the case for surface-bound systems.

12.4 Discussion

In Chapter 11 we concluded that for diffusional voltammetry both the Butler-Volmer and asymmetric Marcus-Hush models can satisfactorily parameterise experimental data. Indeed, an approximate equivalence relationship between the electron transfer coefficient

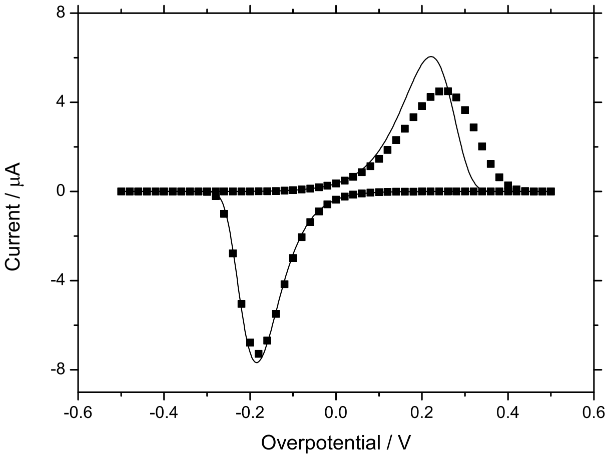

Figure 12.12: Simulated cyclic voltammetry for a surface-bound redox couple with $RTk_0/Fv = 0.01$ ($k_0 = 0.389\,\mathrm{s}^{-1}$ and $v = 1\,\mathrm{V\,s}^{-1}$). The black squares were simulated using asymmetric MH kinetics ($\lambda = 1\,\mathrm{eV}$ and $\omega/\lambda = +0.45$), the solid line is the best fit of the reductive peak achieved using Butler-Volmer kinetics ($\alpha = 0.56$).

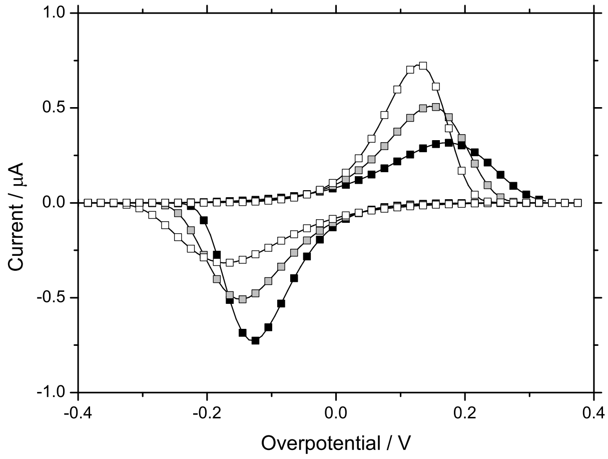

Figure 12.13: Simulated square wave voltammetry for a surface-bound redox couple obeying asymmetric Marcus-Hush kinetics with $k_0/f = 0.01$ ($k_0 = 1\,\mathrm{s}^{-1}$ and $f = 100\,\mathrm{Hz}$), $\lambda = 1\,\mathrm{eV}$ and $\omega/\lambda = +0.45$ (black), -0.45 (white) and 0 (grey). Pulse amplitude = 25 mV and step potential = 10 mV.

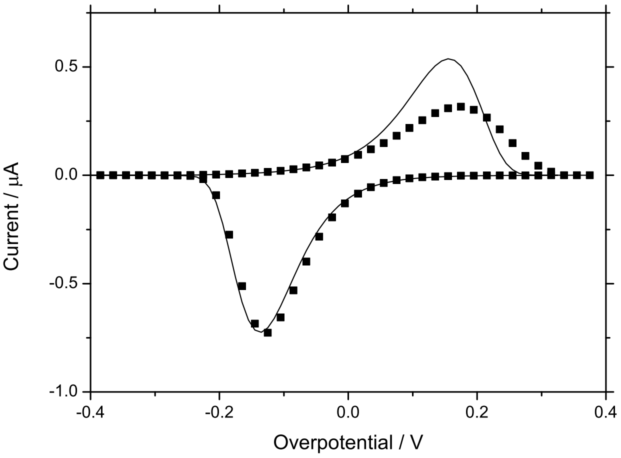

Figure 12.14: Simulated square wave voltammetry for a surface-bound redox couple with $k_0/f = 0.01$ ($k_0 = 1\,\mathrm{s}^{-1}$ and $f = 100\,\mathrm{Hz}$). The black squares were simulated using asymmetric Marcus-Hush kinetics ($\lambda = 1\,\mathrm{eV}$ and $\omega/\lambda = +0.45$), the solid line is the best fit of the reductive peak achieved using Butler-Volmer kinetics ($\alpha = 0.54$). Pulse amplitude = 25 mV and step potential = 10 mV.

(α) and the asymmetry parameter (ω/λ) was established. This enables the use of the simpler Butler-Volmer model while maintaining the ability to gain physical insights about the system through the relationship with the asymmetric Marcus-Hush model.

However for the case of electroactive monolayers the two models are no longer indistinguishable (as shown in Figures 12.12 and 12.14) due to the smaller values of reorganisation energy which are typical for surface-bound systems. Additionally experimental evidence has demonstrated numerous features which the Butler-Volmer is unable to account for [2–4, 9]. As such the use of the Butler-Volmer model should be restricted to systems with highly reversible electrode kinetics.

The symmetric Marcus-Hush model correctly predicts curved Tafel plots and deviations from the Butler-Volmer trends in peak current and potential, however it is unable to model the asymmetry evident in many experimental Tafel plots and cannot account for unequal cathodic and anodic peak currents or peak overpotentials. This model has been successfully employed for some systems, notably the ferrocene system studied by Chidsey [2], however the use of this model may not be appropriate in all cases. In particular the practice of independently fitting the cathodic and anodic branches of a Tafel plot to gain two values for the reorganisation energy is to be discouraged due to its thermodynamic inconsistency.

The asymmetric Marcus-Hush model, however, has been able to reproduce each of the features of experimental cyclic and square wave voltammetry considered here. Further, the use of this model enables the extraction of physically insightful kinetic data and conversely allows for predictions based upon previously known data. Given that this model encompasses the symmetric version, but with greater flexibility, we recommend that the analysis of surface-bound redox couples should be performed using the asymmetric Marcus-Hush model.

12.5 Conclusions

The asymmetric Marcus-Hush model has been applied to the simulation of surface-bound redox systems by cyclic voltammetry and square wave voltammetry. Comparison has been made with both the empirical Butler-Volmer model and the symmetric Marcus-Hush model.

The asymmetric Marcus-Hush model has been shown to most accurately reproduce the experimentally observed features of surface-bounds redox systems: it yields asymmetric curved Tafel plots and predicts the correct non-linear trends in both peak current and peak potential for both cyclic and square wave voltammetry. As such its use for the analysis of surface-bound redox systems is strongly recommended.

Bibliography

[1] M. C. Henstridge, E. Laborda and R. G. Compton, *J. Electroanal. Chem.* **674** (2012) 90–96.

[2] C. E. D. Chidsey, *Science* **251** (1991) 919–922.

[3] R. J. Forster, P. Loughman and T. E. Keyes, *J. Am. Chem. Soc.* **122** (2000) 11948–11955.

[4] S. Fletcher and T. S. Varley, *Phys. Chem. Chem. Phys.* **13** (2011) 5359–5364.

[5] J. T. Hupp and M. J. Weaver, *J. Phys. Chem.* **88** (1984) 6128–6135.

[6] R. J. Forster and L. R. Faulkner, *J. Am. Chem. Soc.* **116** (1994) 5444–5452.

[7] R. J. Forster, *Inorg. Chem.* **35** (1996) 3394–3403.

[8] H. O. Finklea, K. Yoon, E. Chamberlain, J. Allen and R. Haddox, *J. Phys. Chem. B* **105** (2001) 3088–3092.

[9] R. M. Haddox and H. O. Finklea, *J. Phys. Chem. B* **108** (2004) 1694–1700.

[10] N. Madhiri and H. O. Finklea, *Langmuir* **22** (2006) 10643–10651.

[11] G. A. Orlowski and H.-B. Kraatz, *Electrochim. Acta* **51** (2006) 2934–2937.

[12] G. A. Orlowski, S. Chowdhury and H.-B. Kraatz, *Langmuir* **23** (2007) 12765–12770.

[13] A. L. Eckermann, J. A. Shaw and T. J. Meade, *Langmuir* **26** (2010) 2904–2913.

[14] H. O. Finklea and D. D. Hanshew, *J. Am. Chem. Soc.* **114** (1992) 3173–3181.

[15] M. C. Henstridge, E. Laborda, Y. Wang, D. Suwatchara, N. Rees, A. Molina, F. Martínez-Ortiz and R. G. Compton, *J. Electroanal. Chem.* **672** (2012) 45–52.

[16] J. Hale, *J. Electroanal. Chem.* **19** (1968) 315 – 318.

[17] S. W. Feldberg, *Anal. Chem.* **82** (2010) 5176–5183.

[18] K. B. Oldham and J. C. Myland, *J. Electroanal. Chem.* **655** (2011) 65–72.

[19] E. Laviron, *J. Electroanal. Chem.* **101** (1979) 19–28.

[20] K. Weber and S. E. Creager, *Anal. Chem.* **66** (1994) 3164–3172.

[21] L. Tender, M. T. Carter and R. W. Murray, *Anal. Chem.* **66** (1994) 3173–3181.

[22] M. C. Henstridge, E. Laborda, E. J. F. Dickinson and R. G. Compton, *J. Electroanal. Chem.* **664** (2012) 73–79.

[23] H. O. Finklea and R. M. Haddox, *Phys. Chem. Chem. Phys.* **3** (2001) 3431–3436.

[24] M. Lovrić and S. Komorsky-Lovrić, *J. Electroanal. Chem.* **248** (1988) 239–253.

[25] V. Mirčeski, S. Komorsky-Lovrić and M. Lovrić, *Square-Wave Voltammetry. Theory and Application, in: Monographs in Electrochemistry* (Springer-Verlag, Berlin, 2007).

Chapter 13

A comparison of the Butler-Volmer and asymmetric Marcus-Hush models of electrode kinetics at the channel electrode

We report a theoretical study of steady-state voltammetry at the channel electrode comparing the Butler-Volmer and Marcus-Hush (both symmetric and asymmetric) models of electrode kinetics. The latter model is shown, for small values of both reorganisation energy and standard rate constant, to exhibit a kinetically-limited steady-state current which is smaller than the mass-transport limiting current. However, the combination of parameters required to observe this kinetically-limited current is unlikely to occur in a 'real' system. We conclude that the Butler-Volmer model is sufficient to accurately model voltammetry under these conditions.

This work has been submitted as an article to the *Journal of Electroanalytical Chemistry.*

13.1 Introduction

When fitting the voltammetry of solution-phase redox systems the Butler-Volmer and asymmetric Marcus-Hush models have proven practically indistinguishable. Indeed in Chapter 11 we advocated using the Butler-Volmer model to fit experimental data obtained under quiescent conditions and mapping these results onto the asymmetric Marcus-Hush model, taking advantage of a simple relationship between the parameters of the two models [1].

In this chapter we extend the comparison of these models to steady-state voltammetry at the channel electrode. This system is able to produce very high solution flow velocities ($\sim 20\,\mathrm{m\,s^{-1}}$) and hence is able to delay the point at which mass transport becomes rate limiting. This ability to maintain kinetic control has enabled the study of systems exhibiting very fast electrode kinetics [2–7] and may permit experimental differentiation of the Butler-Volmer and asymmetric Marcus-Hush models.

13.2 Theory

The simulations presented here make use of the same model used in Chapter 8. Significantly, the simulation model makes use of the full parabolic flow velocity profile.

The geometry of the channel is held constant in all of the simulations presented here with $d = 2.0\,\mathrm{mm}$, $2h = 0.15\,\mathrm{mm}$ and $w_\mathrm{e} = 1.0\,\mathrm{mm}$. Unless otherwise stated $x_\mathrm{e} = 10\,\mathrm{\mu m}$, $V_\mathrm{f} = 1\,\mathrm{cm^3\,s^{-1}}$, $c_\mathrm{A} = 1\,\mathrm{mM}$ and $D_\mathrm{A} = D_\mathrm{B} = 10^{-5}\,\mathrm{cm^2\,s^{-1}}$.

The transport-limited steady-state current under conditions of laminar flow is given by the Levich equation [8]:

$$I_\mathrm{Levich} = 0.925\, F\, c_\mathrm{A}^*\, x_\mathrm{e}^{2/3}\, w_\mathrm{e}\, D_\mathrm{A}^{2/3} \left(\frac{V_\mathrm{f}}{h^2 d}\right)^{1/3} \tag{13.1}$$

The derivation of this equation assumes that the diffusion layer at the electrode is sufficiently thin that the parabolic flow velocity profile may be approximated as linear. This approximation remains valid for high flow rates and short electrodes [9].

13.3 Results

13.3.1 Effect of reorganisation energy

It has been previously shown [1] that as $\lambda \to \infty$ the Marcus-Hush model becomes equivalent to the Butler-Volmer model with transfer coefficient given by:

$$\alpha = \frac{1}{2} + \frac{1}{4}\frac{\omega}{\lambda} \tag{13.2}$$

Figure 13.1 shows the effect of varying reorganisation energy on steady-state voltammetry at the high speed channel electrode. In this case the parameter ω is set to zero and so the largest values of reorganisation energy yield voltammetry which is very similar to that of the BV model for $\alpha = 0.5$. As λ decreases the current rises less and less steeply towards the limiting current, deviating further from the Butler-Volmer limit, before converging on the same limiting current.

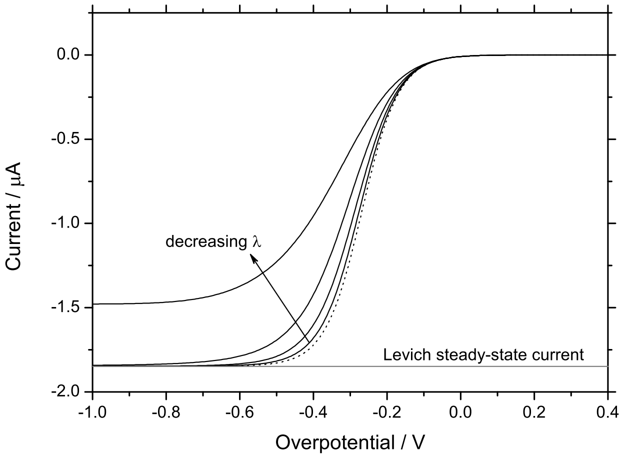

Figure 13.1: Steady state voltammetry at the high speed channel electrode for the BV model (dotted line, $\alpha = 0.5$) and SMH model (solid lines, $\lambda = 5$, 2, 1 and 0.5 eV). For both models $k_0 = 10^{-3}\,\mathrm{cm\,s^{-1}}$.

The most striking feature, however, is that for very small values of reorganisation energy ($\lambda = 0.5\,\mathrm{eV}$) the current limits at a value significantly smaller than predicted by the Levich equation.

We may understand this behaviour by considering the analytical results of Klatt and Blaedel [10, 11] who considered a cylindrical tube electrode. However their results have been recast in the rectangular channel geometry considered here by Rees *et al.* [12]. The steady-state current is given as a function of potential:

$$I/I_{\mathrm{rev}} = 1 - 2u + 2u^2 \ln(1 + u^{-1}) \tag{13.3}$$

where I_{rev} is the current which would flow if the kinetics were totally reversible, given by:

$$I_{\mathrm{rev}} = \frac{I_{\mathrm{Levich}}}{1 + (D_{\mathrm{A}}/D_{\mathrm{B}})^{2/3} \exp[\theta]} \tag{13.4}$$

and

$$u = \frac{0.6783\, D_{\mathrm{B}}^{2/3}(3V_{\mathrm{f}}/4h^2dx_{\mathrm{e}})^{1/3}}{k_{\mathrm{ox}} + (D_{\mathrm{B}}/D_{\mathrm{A}})^{2/3}k_{\mathrm{red}}} \tag{13.5}$$

By inspection the current tends to I_{rev} (which is equal to I_{Levich} at very negative potentials) as the function on the right-hand side of Equation (13.3) tends to unity, which occurs as u tends to zero. Thus the Levich limit is attained only when the kinetic term in the denominator of Equation (13.5) is very large in comparison with the mass transport term in the numerator.

Within the Butler-Volmer model rate constants increase with overpotential *ad infinitum* and so at some sufficiently oxidising or reducing potential u will become vanishingly small.

Within the Marcus-Hush model, however, the rate constants do not continue to increase *ad infinitum*, rather they reach a limiting value as shown in Figure 13.2. As λ decreases the rate constants begin to level off at smaller overpotentials and thus limit to smaller values. As such when both k_0 and λ are sufficiently small, as is the case in Figure 13.1 for $\lambda = 0.5\,\mathrm{eV}$, the kinetic term in Equation (13.5) remains comparable in magnitude to the mass transport term. Consequently u does not tend to zero and the current does not reach the 'Levich limit'.

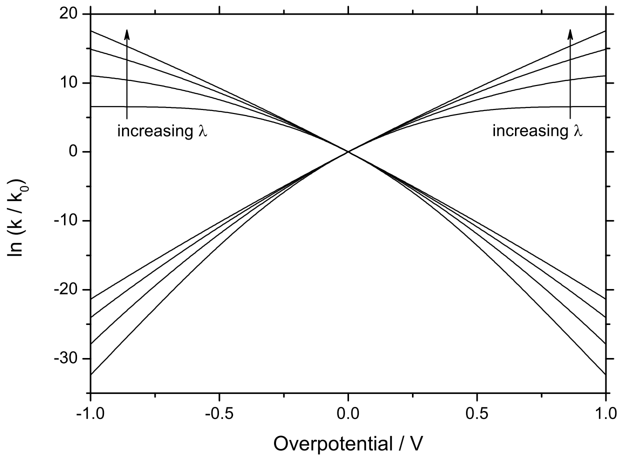

Figure 13.2: Variation of oxidative and reductive rate constants within the SMH model, $\lambda = 0.5$, 1.0, 2.0 and 5.0 eV.

13.3.2 Variation of flux along electrode

The altered steady-state current evident in Figure 13.1 must arise due to a different distribution of flux across the electrode surface. According to the Blaedel-Klatt analysis [10, 11] this is again a function of both mass transport and kinetic terms:

$$\left.\frac{\partial c_\mathrm{A}}{\partial y}\right|_{y=0} \propto \frac{1}{[0.6783\, D_\mathrm{B}^{2/3}(3V_\mathrm{f}/4h^2d)^{1/3}] + [k_\mathrm{ox} + (D_\mathrm{B}/D_\mathrm{A})^{2/3}k_\mathrm{red}]x^{1/3}} \tag{13.6}$$

Figure 13.3 shows the variation of the flux along the electrode for two of the systems shown in Figure 13.2 (Butler-Volmer, $\alpha = 0.5$ and Marcus-Hush, $\lambda = 0.5\,\mathrm{eV}$) plotted in log-log form. The Butler-Volmer model clearly yields a linear variation with a gradient of -1/3, indicating that the kinetic term in $x^{1/3}$ dominates the mass transport term in Equation (13.6). The Marcus-Hush model (with $\lambda = 0.5\,\mathrm{eV}$), however, shows significant deviation from the $x^{-1/3}$ behaviour of the Butler-Volmer model, particularly for small x, demonstrating that the mass transport and kinetic terms are comparable in magnitude.

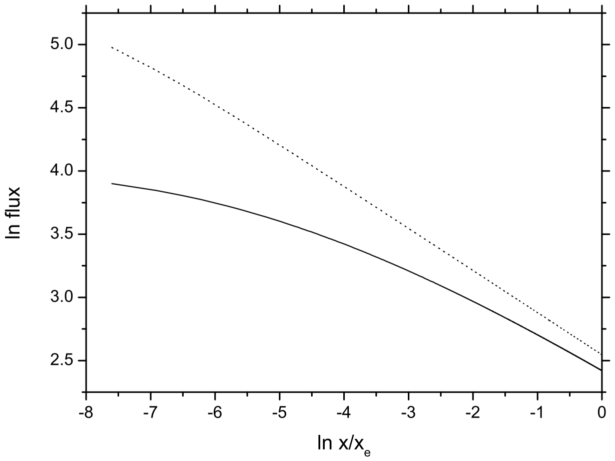

Figure 13.3: Steady-state flux distribution across the electrode surface at an overpotential of $-1.0\,\mathrm{V}$ for the BV model (dotted line, $\alpha = 0.5$) and SMH model (solid line, $\lambda = 0.5\,\mathrm{eV}$). For both models $k_0 = 10^{-3}\,\mathrm{cm\,s^{-1}}$.

13.3.3 Effect of the asymmetry parameter

In Chapter 11 we showed that the important parameter in terms of varying the 'shape' of a voltammogram is the ratio ω/λ and that this value behaves in a manner qualitatively similar to the transfer coefficient within the Butler-Volmer model [1].

Figure 13.4 shows voltammetry simulated for a range of ω/λ values, all with $k_0 = 10^{-3}\,\mathrm{cm\,s^{-1}}$ and $\lambda = 1\,\mathrm{eV}$. In each case the steady-state current is equal to the Levich value, however the three transients diverge in the region $-0.2\,\mathrm{V}$ to $-0.6\,\mathrm{V}$. In this region each value of ω/λ yields a different gradient, as does the transfer coefficient within the Butler-Volmer model.

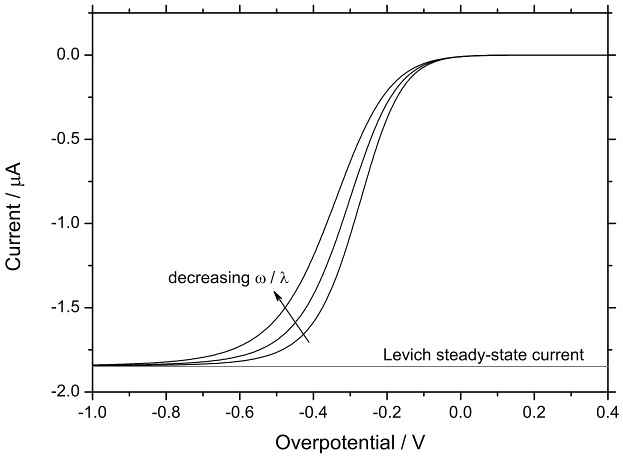

Figure 13.4: Steady state voltammetry at the high speed channel electrode for the asymmetric Marcus-Hush model, $k_0 = 10^{-3}\,\mathrm{cm\,s^{-1}}$, $\lambda = 1\,\mathrm{eV}$, $\omega/\lambda = -0.2$, 0, +0.2.

13.3.4 Application to a ‘real’ system

We now consider a ‘real’ system to test the viability of using the high speed channel electrode to differentiate between the Butler-Volmer and asymmetric Marcus-Hush models.

The one-electron reduction of 2-methyl-2-nitropropane (MeNP) has previously been studied at a mercury microhemisphere electrode using both the BV and AMH models [1]. For both models k_0 was found to be $3 \times 10^{-3}\,\mathrm{cm\,s^{-1}}$, for BV kinetics $\alpha = 0.38$ and for AMH kinetics $\omega/\lambda = -0.31$. While the exact value of reorganisation energy is not known for this system, it has been estimated as approximately 2.5 eV [13]. The diffusion coefficients of MeNP and the radical anion $\mathrm{MeNP}^{\bullet-}$ were both found to be $2.7 \times 10^{-5}\,\mathrm{cm^2\,s^{-1}}$.

We use the largest practical V_f and smallest x_e in order to maximise u and hence maximise the possibility of the steady-state currents differing between the two models. For the high speed channel electrode these extremes are represented by the values $V_\mathrm{f} =$

$4.55\,\mathrm{cm^3\,s^{-1}}$ and $x_\mathrm{e} = 1\,\mathrm{\mu m}$ [12]. The voltammetry simulated using these parameters is shown in Figure 13.5.

Note that while in reality it would not be possible to use a mercury electrode in the high speed flow cell, these parameters are used as illustrative values.

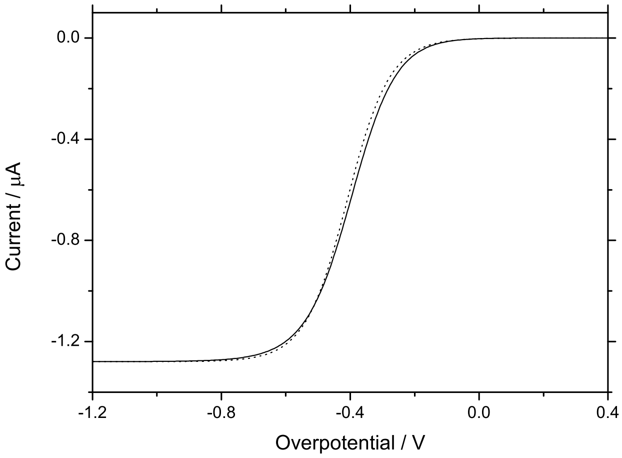

Figure 13.5: Steady-state voltammetry for the reduction of MeNP modeled using the BV model (dotted line, $\alpha = 0.38$) and AMH model (solid line, ω/λ = -0.31, $\lambda = 2.5\,\mathrm{eV}$). For both models $k_0 = 3 \times 10^{-3}\,\mathrm{cm\,s^{-1}}$, $V_\mathrm{f} = 4.55\,\mathrm{cm^3\,s^{-1}}$ and $x_\mathrm{e} = 1\,\mathrm{\mu m}$.

As was the case in quiescent solution [1], the two models give almost indistinguishable voltammetry. There is a slight difference in the gradient of current increase around $-0.4\,\mathrm{V}$, with the Butler-Volmer giving rise to a steeper transient, however this is not likely to be sufficiently large to discriminate between the two models when compared with experimental data. Significantly, the steady-state currents resulting from the two models are identical.

13.4 Discussion

In order to observe a kinetically-limited steady-state current it is necessary for the rate constants to have reached a limiting value. For this to be the case a small value of reorganisation energy is required. Further this value of limiting rate constant must be sufficiently small so as not to dominate the mass transport term in Equation (13.5) and so the system must also possess a small standard rate constant.

When we consider the significance of the parameters λ and k_0 within Marcus theory, which rationalises the rate of electron transfer in terms of molecular reorganisation, we see that this combination of small λ and small k_0 is not likely to occur in a 'real' system. A small reorganisation energy leads to fast electrode kinetics and hence a high standard rate constant. Conversely, a large reorganisation energy gives rise to sluggish electrode kinetics and small values of standard rate constant, as is the case for the reduction of MeNP. Thus, the theoretically predicted kinetically-limited current is not likely to be observed experimentally.

For quiescent solution-phase voltammetry we have previously concluded (Chapter 11) that it is probably best to use the Butler-Volmer model to fit experimental voltammetry and to use Equation (13.2) to relate the value of the transfer coefficient to the ratio ω/λ. Given the strong similarity between the steady-state voltammetry of the Butler-Volmer and asymmetric Marcus-Hush models when applied to the reduction of MeNP, we suggest that this methodology is likely equally suitable for the study of redox systems under convective mass transport conditions.

13.5 Conclusions

We have demonstrated that, when employing Marcus-Hush kinetics with small values of both k_0 and λ, it is theoretically possible to observe a steady-state current which is smaller than the transport-limited current given by the Levich equation. This behaviour is not observed for Butler-Volmer kinetics and is due to the limiting behaviour of the rate constants when using the Marcus-Hush model.

However this phenomenon is not likely to be observable for a 'real' system since, according to Marcus theory, small values of λ lead to large values of k_0 and so these parameters may not both take small values simultaneously. Consequently we conclude that the Butler-Volmer model is likely sufficient for the analysis of systems under convective mass transport regimes.

Bibliography

[1] M. C. Henstridge, E. Laborda, Y. Wang, D. Suwatchara, N. Rees, A. Molina, F. Martínez-Ortiz and R. G. Compton, *J. Electroanal. Chem.* **672** (2012) 45–52.

[2] N. V. Rees, R. A. W. Dryfe, J. A. Cooper, B. A. Coles, R. G. Compton, S. G. Davies and T. D. McCarthy, *J. Phys. Chem.* **99** (1995) 7096–7101.

[3] B. A. Coles, R. A. Dryfe, N. V. Rees, R. G. Compton, S. G. Davies and T. D. McCarthy, *J. Electroanal. Chem.* **411** (1996) 121–127.

[4] N. V. Rees, O. V. Klymenko, B. A. Coles and R. G. Compton, *J. Electroanal. Chem.* **534** (2002) 151–161.

[5] N. V. Rees, O. V. Klymenko, E. Maisonhaute, B. A. Coles and R. G. Compton, *J. Electroanal. Chem.* **542** (2003) 23–32.

[6] A. D. Clegg, N. V. Rees, O. V. Klymenko, B. A. Coles and R. G. Compton, *J. Am. Chem. Soc.* **126** (2004) 6185–6192.

[7] N. V. Rees and R. G. Compton, *Russ. J. Electrochem.* **44** (2008) 368–389.

[8] V. G. Levich, *Physicochemical Hydrodynamics* (Prentice-Hall: Englewood Cliffs, 1962).

[9] J. A. Alden and R. G. Compton, *J. Electroanal. Chem.* **404** (1996) 27–35.

[10] W. J. Blaedel and L. N. Klatt, *Anal. Chem.* **38** (1966) 879–883.

[11] L. N. Klatt and W. J. Blaedel, *Anal. Chem.* **39** (1967) 1065–1072.

[12] N. V. Rees, J. A. Alden, R. A. W. Dryfe, B. A. Coles and R. G. Compton, *J. Phys. Chem.* **99** (1995) 14813–14818.

[13] D. Suwatchara, M. C. Henstridge, N. V. Rees and R. G. Compton, *J. Phys. Chem. C* **115** (2011) 14876–14882.

Chapter 14

Direct extraction of kinetic parameters from experimental cyclic voltammetry

We introduce a novel method for the direct extraction of kinetic data from experimental cyclic voltammetry using numerical simulation. This method is *not* specific to a particular model of electrode kinetics, such as the Butler-Volmer or Marcus-Hush models, and is general to all electrode geometries for which the current density is uniform across the surface. The method is demonstrated using both theoretically simulated voltammetry and experimental data for the reduction of 2-methyl-2-nitropropane at a mercury hemisphere electrode. For the latter system, excellent agreement with previously reported kinetic parameters is obtained.

This work has been published in the *Journal of Electroanalytical Chemistry* [1].

14.1 Introduction

Voltammetry is a sensitive and widely used technique for the investigation of chemical kinetics. A simplistic analysis of the current transient can easily yield qualitative kinetic information such as the number of electrons transferred during the reaction and whether the reaction exhibits 'reversible' or 'irreversible' kinetics.

However, in order to extract more meaningful, quantitative information it is necessary to compare experimental voltammetry with a theoretical model, often requiring numerical simulation. One usually aims to recreate the observed current-voltage curve by changing the parameters of the model. Once a good 'fit' between model and experiment has been achieved, one can then confidently ascribe those parameters to the experimental system.

This iterative fitting process, however, generally proceeds via trial and error, with no guarantee of finding a set of parameters which 'fit' the experimental data even after many attempts. In the present chapter we demonstrate a method which directly extracts the potential dependence of the oxidative and reductive rate constants for a one-electron redox process from an experimental voltammogram. This method makes no assumptions regarding the form of the potential dependence of kinetics parameters and is general to all systems with 'one-dimensional' geometry. Prior art in this area is limited to convolution methods [2] such as 'global analysis' [3, 4] which involve complex mathematical concepts. The method described here is much simpler to implement and, in essence, requires only a modification of the conventional procedure for numerically simulating cyclic voltammetry.

The new method is tested first against theoretical voltammetry and then on real experimental data for the reduction of 2-methyl-2-nitropropane at a mercury hemisphere electrode, yielding excellent agreement with previously reported [3–6] kinetic data for this system.

14.2 Theory

Our goal is to extract, from experimental cyclic voltammetry, information about the rate of the redox reaction $\mathrm{A} + \mathrm{e} \rightleftharpoons \mathrm{B}$ occurring in solution at the surface of an electrode. We assume only that the reaction follows first-order kinetics:

$$j_{\mathrm{A},0} = -k_{\mathrm{A}} c_{\mathrm{A},0} + k_{\mathrm{B}} c_{\mathrm{B},0} \tag{14.1}$$

where $j_{\mathrm{A},0}$ is the flux of A at the electrode surface, k_{A} and k_{B} are the rate constants for the consumption of A and B respectively and $c_{\mathrm{A},0}$ and $c_{\mathrm{B},0}$ are the concentrations of A and B at the electrode surface.

The reaction is further assumed to occur under diffusion-only conditions, *i.e.* the solution is assumed to contain sufficient supporting electrolyte that migration may be neglected. The system is therefore fully described by Fick's second law, which has the following form in one-dimension:

$$\frac{\partial c_i}{\partial t} = D_i \left[\frac{\xi}{r} \frac{\partial c_i}{\partial r} + \frac{\partial^2 c_i}{\partial r^2} \right] \tag{14.2}$$

where c_i and D_i are respectively the concentration and diffusion coefficient of species i, r is distance and t is time. The parameter ξ is geometry dependent; taking the value 0 for a planar system, 1 for a cylindrical system and 2 for a spherical system.

In order to solve Equation (14.2) we require boundary conditions. At $t = 0$ we assume that, throughout the simulation space, species A takes its bulk value (c_{A}^*) uniformly and that species B is absent. The outer boundary of the simulation space is set to be sufficiently far from the electrode surface such that the concentrations of A and B remain at these initial values.

$$r_{\mathrm{max}} = r_{\mathrm{e}} + 6\sqrt{D_{\mathrm{max}}\, t_{\mathrm{max}}} \tag{14.3}$$

where r_{e} is the r-coordinate of the electrode surface, D_{max} is the larger of D_{A} and D_{B} and t_{max} is the duration of the experiment.

This leaves only the boundary condition to be applied at the electrode surface. Since we *assume* no knowledge of k_{A} and k_{B}, the use of Equation (14.1) is inappropriate. The variation of current with potential available from the experimental voltammetry, however, provides us with an alternative boundary condition. The current (I) is related to the surface flux via:

$$I = FAj_{\mathrm{A},0} \tag{14.4}$$

where F is the Faraday constant and A is the electrode area. Further, the flux is related to the concentration gradient via Fick's first law:

$$j_i = -D_i \frac{\partial c_i}{\partial r} \tag{14.5}$$

Combining Equations (14.4) and (14.5) yields the required boundary condition for species A:

$$\left.\frac{\partial c_{\mathrm{A}}}{\partial r}\right|_{r=r_{\mathrm{e}}} = -\frac{I}{FAD_{\mathrm{A}}} \tag{14.6}$$

Mass conservation at the electrode surface requires that the flux of A is exactly opposed by the flux of B, as such the equivalent boundary condition for species B omits the minus sign.

Equation (14.2) is solved with respect to these boundary conditions using the backwards implicit finite difference method [7]. This process yields values for c_{A} and c_{B} at every point in the simulation space, of which only the values for the electrode surface are retained for later analysis. This process is repeated for each point of the experimental voltammogram such that, upon completion, we have two values for I, $c_{\mathrm{A},0}$ and $c_{\mathrm{B},0}$ for each value of potential – one from the forward scan and one from the reverse.

Combining Equations (14.1) and (14.4) yields a relationship linking these quantities:

$$I = FA\left[-k_{\mathrm{A}}c_{\mathrm{A},0} + k_{\mathrm{B}}c_{\mathrm{B},0}\right] \tag{14.7}$$

Substitution of the two sets of data into Equation (14.7) results in two equations in two unknowns which may be solved simultaneously for each value of E, yielding k_{A} and k_{B} as a function of potential.

14.3 Results

14.3.1 Analysis of theoretical voltammetry

In order to test this new method in a verifiable manner, it was first checked against simulated voltammetry. For this purpose, cyclic voltammetry was simulated for a hemispherical electrode at a range of rate constants and voltage scan rates. Additionally, to demonstrate that the method is not model-specific we studied voltammetry simulated using both the Butler-Volmer [8, 9] and asymmetric Marcus-Hush (Chapter 10 and references [6, 10]) models of electrode kinetics. Typical results of the analysis of this simulated voltammetry are shown in Figures 14.1 and 14.2. For the former, $\ln k$ varies linearly with potential whereas the latter shows a distinct curvature which is characteristic of the Marcus-Hush model. In both cases the variation of the extracted oxidative and reductive rate constants is indistinguishable from the theoretical values used to simulate the voltammetry for almost the whole potential range.

There is, however, a small region at very negative overpotentials for which the extracted oxidative rate constant deviates from the theoretical value. As is shown in Figure 14.3, which shows the variation of the surface concentrations of A and B for the voltammetry shown in Figure 14.1, the surface concentration of A in this potential range is effectively zero. The discrepancy between the theoretical and extracted oxidative rate

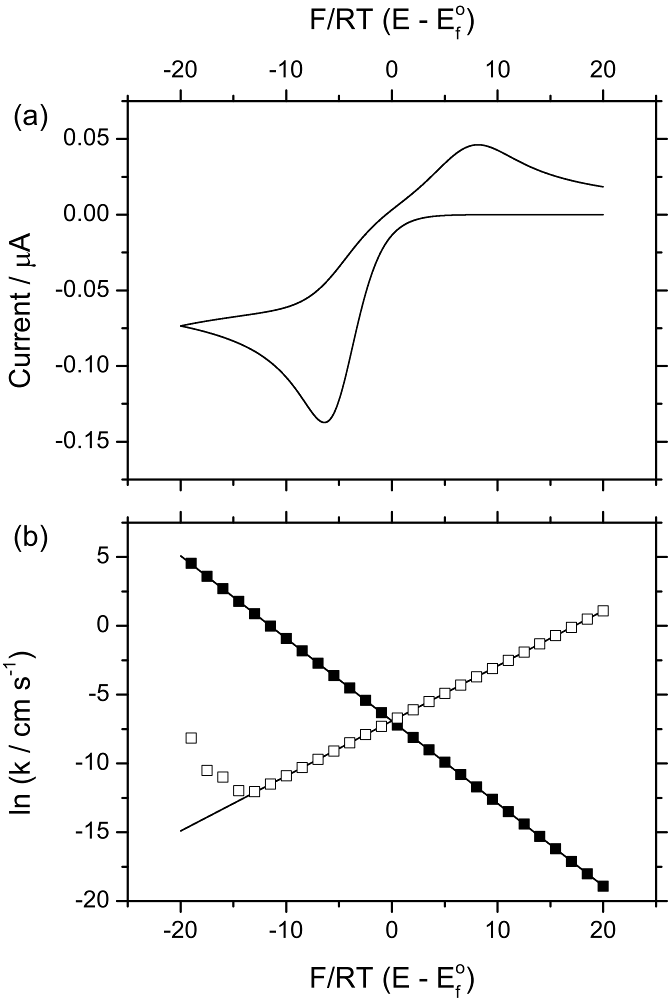

Figure 14.1: (a) Cyclic voltammogram simulated for a hemispherical electrode with radius 50 µm at a scan rate of $1\,\mathrm{V\,s^{-1}}$, $D_\mathrm{A} = D_\mathrm{B} = 10^{-5}\,\mathrm{cm^2\,s^{-1}}$, Butler-Volmer kinetics were assumed with $k_0 = 10^{-3}\,\mathrm{cm\,s^{-1}}$ and $\alpha = 0.6$ and (b) plot showing both the theoretical (solid lines) and extracted (square points) variation of rate constant with applied potential.

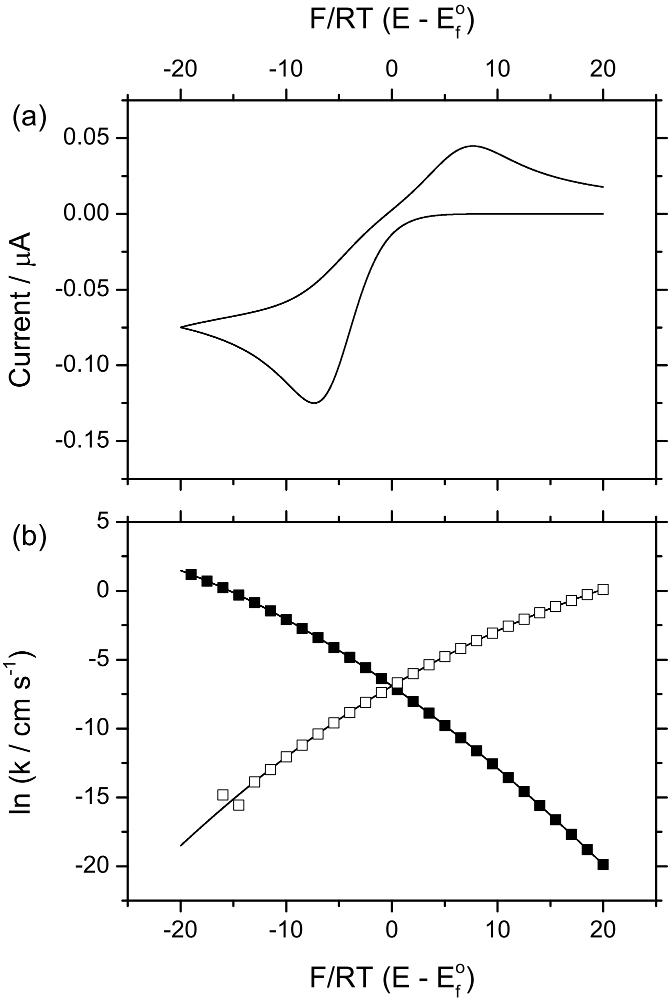

Figure 14.2: (a) Cyclic voltammogram simulated for a hemispherical electrode with radius 50 µm at a scan rate of 1 V s^{-1}, $D_A = D_B = 10^{-5}$ cm^2 s^{-1}, asymmetric Marcus-Hush kinetics were assumed with $k_0 = 10^{-3}$ cm s^{-1}, $\lambda = 1$ eV and $\beta/\lambda = +0.2$ and (b) plot showing both the theoretical (solid lines) and extracted (square points) variation of rate constant with applied potential.

constants seen in Figures 14.1 and 14.2 is caused by machine error resulting from this zero concentration of A.

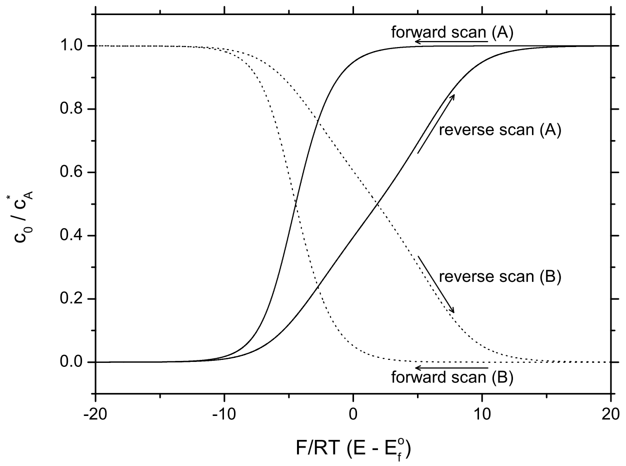

Figure 14.3: Surface concentrations of species A (solid line) and B (dotted line) extracted from the voltammogram shown in Figure 14.1.

From these theoretical plots it is clear that this method enables easy extraction of both the formal potential and the standard rate constant from the crossing point of the two lines. The formal potential is often estimated from the mid-point between the forward and back peaks with a correction due to the ratio of D_A and D_B; however, the crossing point (such as in Figures 14.1 and 14.2) represents the formal potential irrespective of the ratio of D_A and D_B.

Further, a linear plot is a clear indication that the system is likely best analysed using the Butler-Volmer model, whereas evidence of curvature suggests that the asymmetric Marcus-Hush model is more appropriate. Thus one can determine, almost by inspection, whether or not a particular system may be described by a particular kinetic model.

14.3.2 Application to experimental voltammetry

Having verified that the method works as expected for theoretical systems for which the kinetic parameters are known, we next analysed the experimental cyclic voltammetry of the reduction of 2-methyl-2-nitropropane (MeNP) at a mercury hemisphere in acetonitrile at a range of scan rates. The experiments, and their fitting using various kinetic models [5, 6], have been reported in Chapters 7 and 11. Thus the values of the initial concentration of MeNP, the radius of the mercury hemisphere, the diffusion coefficients for both MeNP and the product radical anion and the exact scan rates were all known and are shown in Table 14.1. A representative cyclic voltammogram and the extracted rate constants results are shown in Figure 14.4.

Parameter	Value
Concentration	1.95 mM
Electrode radius	24.0 µm
D_{MeNP}	$2.7 \times 10^{-5}\,\mathrm{cm^2\,s^{-1}}$
$D_{\mathrm{MeNP}^{\cdot -}}$	$2.7 \times 10^{-5}\,\mathrm{cm^2\,s^{-1}}$
Solvent	Acetonitrile
Supporting electrolyte	0.1 M TBAP
Temperature	298 K

Table 14.1: Experimental parameters for MeNP voltammetry.

For potentials beyond the voltammetric peaks the current is diffusion-limited rather than kinetically-limited; precluding the extraction of any meaningful kinetic information. The region between the two peaks, however, does allow for useful analysis (Figure 14.5). The rate constants exhibit a linear dependence on overpotential, indicative of Butler-Volmer kinetics. Analysing the slopes of the two lines yields the two Butler-Volmer transfer coefficients: $\alpha = 0.408$ and $\beta = 0.607$. The crossing point of the two lines also gives the formal potential and standard rate constant: $k_0 = 4.06 \times 10^{-3}\,\mathrm{cm\,s^{-1}}$ and $E_{\mathrm{f}}^{\ominus} = -1.817\,\mathrm{V}$ vs Ag wire.

The accuracy of these values was verified via a separate simulation, shown overlaid with the experimental data in Figure 14.6, which fits the experiment extremely well. The kinetic parameters obtained at other scan rates are shown in Table 14.2. These values are consistent with those published previously [3–6, 11, 12].

It should be noted that this technique relies upon there being two different values of I, $c_{\mathrm{A},0}$ and $c_{\mathrm{B},0}$ at any particular potential in order to extract the desired information. This requirement, however, is not met when the voltammetry takes on steady-state character because the current is the same for both forward and back scans, leaving only one equation with two unknowns. This problem restricted the range of scan rates which could be

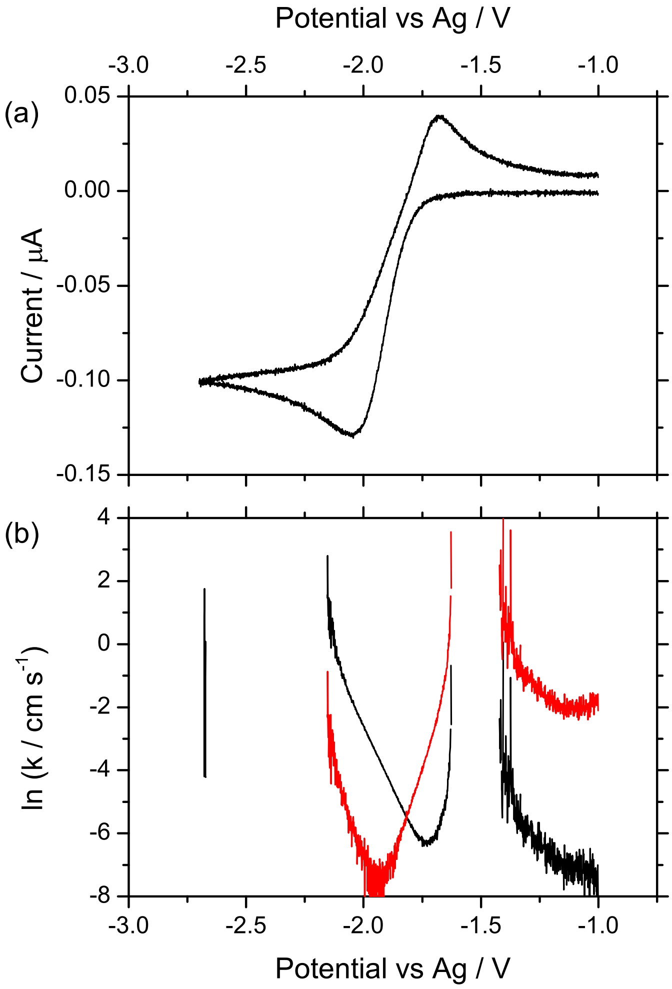

Figure 14.4: (a) Experimental cyclic voltammetry of 1.95 mM MeNP in acetonitrile at $1\,\mathrm{V\,s^{-1}}$ and (b) the extracted potential dependence of the rate constants.

Scan rate ($\mathrm{mV\,s^{-1}}$)	α	β	$E_f^{\ominus}$ (V)	k_0 ($\mathrm{cm\,s^{-1}}$)
500	0.398	0.619	-1.814	4.04×10^{-3}
1000	0.408	0.607	-1.817	4.06×10^{-3}
2000	0.396	0.589	-1.816	4.19×10^{-3}
5000	0.386	0.576	-1.812	4.32×10^{-3}

Table 14.2: Kinetic data extracted from experimental voltammetry of 1.95 mM MeNP in acetonitrile at a range of scan rates.

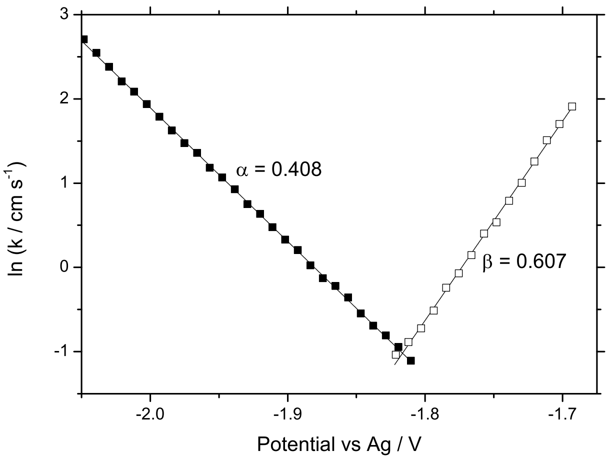

Figure 14.5: Potential dependence of the rate constants in the vicinity of the formal potential, extracted from experimental voltammetry of MeNP at $1\,\mathrm{V\,s^{-1}}$.

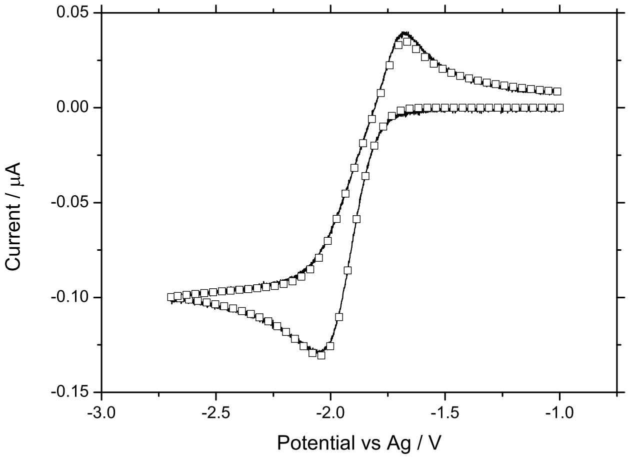

Figure 14.6: Experimental voltammetry of 1.95 mM MeNP in acetonitrile (solid line) and voltammetry simulated using the extracted kinetic parameters (squares) at $1\,\mathrm{V\,s^{-1}}$.

meaningfully analysed for the MeNP system.

14.4 Discussion

This method offers many advantages over the conventional iterative fitting procedure. First, it needs only to be performed once; greatly increasing the speed of analysis. Second, it does not assume a specific model of electrode kinetics; allowing unbiased interpretation of experiments. Further, this method represents only a minor modification of the conventional method for simulating voltammetry; allowing for relatively fast and easy implementation using existing programs, in contrast with convolution methods, which follow a completely separate procedure.

This method is general to all 'one-dimensional' systems, for which the flux is uniform across the electrode surface and can therefore be inferred by the value of the current. It is thus not applicable in its current state to other systems, such as the microdisc electrode or flow systems, where the values of the two currents as a function of potential is not sufficient to determine the variation of flux across the electrode surface.

14.5 Conclusions

We have described a novel technique for the direct extraction of kinetic parameters from experimental voltammetry. The method is general for all 'one-dimensional' systems and has been demonstrated to yield accurate data from real experimental data. We expect that the current methodology may also be adapted to allow for the analysis of experiments employing pulse voltammetry and those for surface-bound redox couples.

Bibliography

[1] M. C. Henstridge and R. G. Compton, *J. Electroanal. Chem.* **681** (2012) 109–112.

[2] A. Neudeck, F. Marken and R. G. Compton, *Electroanalysis* **11** (1999) 1149–1154.

[3] C. G. Zoski, K. B. Oldham, P. J. Mahon, T. L. Henderson and A. M. Bond, *J. Electroanal. Chem.* **297** (1991) 1–17.

[4] A. Bond, P. Mahon, E. Maxwell, K. Oldham and C. Zoski, *J. Electroanal. Chem.* **370** (1994) 1–15.

[5] M. C. Henstridge, Y. Wang, J. G. Limon-Petersen, E. Laborda and R. G. Compton, *Chem. Phys. Lett.* **517** (2011) 29–35.

[6] M. C. Henstridge, E. Laborda, Y. Wang, D. Suwatchara, N. V. Rees, A. Molina, F. Martínez-Ortiz and R. G. Compton, *J. Electroanal. Chem.* **672** (2012) 45–52.

[7] D. Britz, *Digital Simulation in Electrochemistry* (Springer, 2005), 3rd edition.

[8] J. A. V. Butler, *Trans. Faraday Soc.* **28** (1932) 379–382.

[9] T. Erdey-Grúz and M. Volmer, *Z. Physik Chem.* **150** (1930) 203–213.

[10] E. Laborda, M. C. Henstridge and R. G. Compton, *J. Electroanal. Chem.* **667** (2012) 48–53.

[11] D. A. Corrigan and D. H. Evans, *J. Electroanal. Chem.* **106** (1980) 287–304.

[12] J. M. Savéant and D. Tessier, *Faraday Discuss. Chem. Soc.* **74** (1982) 57–72.

Chapter 15

Conclusions

We studied voltammetry at porous electrodes in Chapters 3 and 4. We showed that the enhanced electrochemical selectivity observed at electrodes modified with porous films may not necessarily be caused by a change in electrode kinetics, rather we have demonstrated that this effect may be explained by a change in the mass transport regime from 'linear' diffusion at unmodified electrodes to 'thin layer' diffusion at modified electrodes. We have also demonstrated the possibility of observing two voltammetric peaks for an irreversible couple at a porous electrode with small pores. The two peaks are attributed to the different diffusional regimes operating at different timescales.

In Chapter 5 we introduced the symmetric Marcus-Hush (SMH) model of electrode kinetics which has three adjustable parameters $\{E_{\mathrm{f}}^{\ominus}, k_0, \lambda\}$ determining the potential dependence of the rate of electron transfer. The Butler-Volmer model is also a three-parameter model $\{E_{\mathrm{f}}^{\ominus}, k_0, \alpha\}$, but the parameters λ and α are seen to have very different effects on the rate constants.

In Chapter 6 we examined two different methods for simulating the voltammetry of kinetically inhomogeneous monolayers: a Gaussian distribution of formal potentials and a Gaussian distribution of tunneling distances. Despite the simplicity of both models, the former is seen to accurately reproduce the experimental voltammetry of a ferrocene-modified EPPG electrode.

A critical evaluation of the SMH model was then undertaken in Chapters 7 and 8. Simulations using both SMH and BV models were compared with experiments for several redox systems. We employed both cyclic and square wave voltammetry both under both diffusion-only conditions at a mercury microhemisphere electrode and under convective mass transport conditions at a platinum microband electrode. We saw that, at best, the

SMH model performs similarly well to the BV model for a reversible system. However, for the majority of systems the BV model yields excellent fitting across a wide range of scan rates while the SMH model is generally unable to fit both forward and back peaks simultaneously, leading to a poor fit overall. We also showed in Chapter 9 that the SMH model is inconsistent with the Randles–Ševčík equation, contrary to much literature which confirms this relationship between scan rate and peak current.

Having found the SMH model to be inadequate for the parameterisation of electrode kinetics, we then introduce the so-called asymmetric Marcus-Hush (AMH) model in Chapter 10. We remove the assumption that the Gibbs energy curves of both reactant and product have the same curvature, introducing a new parameter ω (which quantifies the differences between the force constants in the reactant and product) to make a four-parameter model $\{E_{\mathrm{f}}^{\ominus}, k_0, \lambda, \omega\}$.This new model is immediately seen to be much more flexible that the SMH model which predicts that the 'transfer coefficient' is always exactly $\frac{1}{2}$ at the formal potential.

In Chapter 11 we then re-examined the systems which were studied previously at a mercury microhemisphere electrode using this new model. The AMH model was seen to perform as well as the BV model and the resulting voltammetry was generally indistinguishable from that produced using the BV model. Significantly the AMH model was seen to be much better able to accurately fit experimental voltammetry than the SMH model.

We also observed that the ratio between the parameters ω and λ is the important factor in determining the quality of fit to experiment and a mathematical relationship was derived which links this ratio to the transfer coefficient in the limit of large reorganisation energy. This relationship enables existing kinetic data in terms of a transfer coefficient to be re-interpreted in terms of asymmetry between the force constants in the reactant and product. Continued use of the BV model for the analysis of diffusional voltammetry was also recommended due to its greater simplicity of application, with results easily re-cast in terms of the AMH model subsequently.

In Chapter 12 we saw that the equivalence between the BV and AMH models is not observed for surface-bound systems where typical reorganisation energies are significantly smaller that for diffusional systems. The AMH model is nevertheless seen to reproduce all experimentally observed trends, significantly including asymmetric curved Tafel plots which neither the SMH nor BV model is able to account for.

We then studied the AMH model under convective conditions in Chapter 13. We showed that it is theoretically possible for a system obeying this kinetic model to display a kinetically-limited steady-state current which is smaller than the transport-limited current given by the Levich equation if both k_0 and λ are small. We concluded, however, that this phenomenon is not likely to occur under presently realisable conditions for a real system, for which the BV and AMH models are again effectively indistinguishable.

Last, in Chapter 14 we introduced a novel method for the direct extraction of rate constants as a function of potential from experimental voltammetry. This method is simply implemented and is general to all one-dimensional electrode geometries. Excellent agreement with previously obtained values was found when the method was used on the experimental voltammetry of 2-methyl-2-nitropropane. This method may also be easily adapted for the analysis of surface-bound systems.

To conclude, we have demonstrated that the *symmetric* Marcus-Hush model is not a good model for the parameterisation of electrode kinetics. We have also shown that the *asymmetric* Marcus-Hush model enables accurate fitting of experimental data for both solution-phase and surface-bound redox couples. For surface-bound systems, however, it is recommended that the Butler-Volmer model is employed instead due to its simplicity, with results subsequently re-cast in terms of the AMH model via the relationship between α and ω/λ outlined in Appendix A. For surface-bound systems, due to its ability to reproduce *both* curved and asymmetric Tafel plots, the AMH model should be used in preference to either the Butler-Volmer model or symmetric Marcus-Hush model.

Future work should attempt to determine the exact values of ω and λ, rather than their ratio, enabling the estimation of the actual force constants of the system. This may be approached by studying the temperature dependence of k_0.

Appendix A

Marcus-Hush kinetics in the limit $\lambda \to \infty$

We shall define the transfer coefficient, α, as follows:

$$\alpha = -\frac{\partial \ln k_{\mathrm{red}}}{\partial \theta} \tag{A.1}$$

Recall from Chapter 5 that within the Marcus-Hush model k_{red} is given by

$$k_{\mathrm{red}} = k_0 \frac{S_{\mathrm{red}}(\theta)}{S_{\mathrm{red}}(0)} \tag{A.2}$$

where

$$S_{\mathrm{red}}(\theta) = \int_{-\infty}^{\infty} \frac{\exp[-\Delta G^{\ddagger}]}{1+\exp[-x]}\, dx \tag{A.3}$$

and

$$\Delta G^{\ddagger} = \frac{\Lambda}{4}\left(1+\frac{\theta+x}{\Lambda}\right)^2 + \frac{\Omega}{4}\left(\frac{\theta+x}{\Lambda}\right)\left[1-\left(\frac{\theta+x}{\Lambda}\right)^2\right] + \frac{\Omega^2}{16\Lambda} \tag{A.4}$$

We are interested in the behaviour of k_{red} in the limit $\Lambda \to \infty$. Under such conditions Equation (A.4) reduces to

$$\Delta G^{\ddagger} = \frac{\Lambda}{4} + \frac{\Omega^2}{16\Lambda} + \theta\left(\frac{1}{2}+\frac{\Omega}{4\Lambda}\right) + x\left(\frac{1}{2}+\frac{\Omega}{4\Lambda}\right) \tag{A.5}$$

Substituting this result into $S_{\mathrm{red}}(\theta)$ and separating terms into those in x and those not yields

$$S_{\mathrm{red}}(\theta) = \exp\left[-\frac{\Lambda}{4} - \frac{\Omega^2}{16\Lambda} - \theta\left(\frac{1}{2}+\frac{\Omega}{4\Lambda}\right)\right] \cdot \int_{-\infty}^{\infty} \frac{\exp\left[-x\left(\frac{1}{2}+\frac{\Omega}{4\Lambda}\right)\right]}{1+\exp[-x]}\, dx \tag{A.6}$$

Note that the integral in Equation (A.6) no longer a function of θ. As such when we take the ratio $S_{\text{red}}(\theta)/S_{\text{red}}(0)$ in calculating k_{red}, the ratio of the integrals will be unity. Thus the expression for k_{red} is reduced to

$$\begin{aligned} k_{\text{red}} &= k_0 \ \exp\left[-\frac{\Lambda}{4} - \frac{\Omega^2}{16\Lambda} - \theta\left(\frac{1}{2} + \frac{\Omega}{4\Lambda}\right)\right] \cdot \exp\left[\frac{\Lambda}{4} + \frac{\Omega^2}{16\Lambda}\right] && \text{(A.7)} \\ &= k_0 \ \exp\left[-\theta\left(\frac{1}{2} + \frac{\Omega}{4\Lambda}\right)\right] && \text{(A.8)} \end{aligned}$$

and so when we substitute this value into Equation (A.1) we obtain

$$\alpha = \frac{1}{2} + \frac{\Omega}{4\Lambda} \tag{A.9}$$

which is equivalent to:

$$\alpha = \frac{1}{2} + \frac{\omega}{4\lambda} \tag{A.10}$$